DISSERTATION

THE NEAR-GLOBAL DISTRIBUTION OF LIGHT PRECIPITATION FROM CLOUDSAT

Submitted by

John M. Haynes

Department of Atmospheric Science

In partial fulfillment of the requirements

For the Degree of Doctor of Philosophy

Colorado State University

Fort Collins, Colorado

Spring 2008

COLORADO STATE UNIVERSITY

March 14, 2008

We hereby recommend that this dissertation prepared under our supervision by John M. Haynes entitled "The Near-Global Distribution of Light Precipitation from CloudSat" be accepted as fulfilling in part requirements for the degree of Doctor of Philosophy.

Committee on Graduate Work

Graeme L. Stephens, Advisor

William R. Cotton

Christian D. Kummerow

Chiao-Yao She

Richard H. Johnson, Department Head

ABSTRACT OF DISSERTATION

THE NEAR-GLOBAL DISTRIBUTION OF LIGHT PRECIPITATION FROM CLOUDSAT

The W-band (94 GHz) Cloud Profiling Radar (CPR) on CloudSat is sensitive to both clouds and precipitation. A precipitation retrieval applicable to spaceborne, millimeter wavelength radars is introduced. Measurements of the attenuated backscatter of the surface are used to derive the path integrated attenuation (PIA) through precipitating columns, which follows from the clear-sky scattering characteristics of the surface. Over ocean, this can be estimated as a function of near-surface wind speed and sea surface temperature. Assuming an exponential rain drop size distribution, the relationship between PIA and rain rate is derived from Mie theory for homogeneous columns of warm rain.

Multiple scattering is found to be significant for rainfall rates exceeding 3 to 5 mm h^{-1}. To correct for this effect, Monte Carlo modeling is used to simulate the relationship between rainfall and PIA for various vertical precipitation profiles. Multiple scattering is found to increase return power to the radar, acting opposite attenuation. A model of the melting layer is also incorporated to better represent attenuating characteristics near the bright band, where snow aggregates melt into rain. It is found that failure to account for extra attenuation caused by melting particles results in overestimation of precipitation rate.

The retrieval algorithm is applied to near-global CloudSat observations. Precipitation in the tropics is found to prefer clouds with lowest-layer cloud tops near 2 and 15 km. A third mode, likely associated with congestus, is found to be common in the tropical western Pacific, Indian, and Atlantic basins. There are vast regions of the globe where nearly all precipitation falls from cloud with lowest-layer tops below 4.75 km. Over the tropical oceans as a whole, precipitation falls twice as often from these clouds as any other cloud type. Furthermore, multiple layered cloud systems are found to be ubiquitous globally. In the tropics, it is estimated that half the accumulated precipitation comes from multiple layered systems rather than the classic "deep convective" model. Outside the tropics, the CPR observes precipitation more often than the passive microwave AMSR-E, with greater resulting seasonal accumulations.

John Matthew Haynes
Department of Atmospheric Science
Colorado State University
Fort Collins, CO 80523
Spring 2008

ACKNOWLEDGMENTS

I would like thank my advisor, Graeme Stephens, for guiding this research, and for allowing me the time and leeway to find my own niche within the broad topics of clouds and atmospheric radiation on which our research group focuses. The focus of this research changed several times before I settled on the topic of precipitation as derived from CloudSat observations. This work would not have been possible without Graeme's leadership in making the CloudSat mission become a reality.

Tristan L'Ecuyer, Denis O'Brien, and and my graduate committee also deserve thanks for making this research possible. Many hours were spent talking with Tristan about precipitation, details of the retrieval, and organization of the precipitation product that is a result of this work. Denis took time out of preparations for the upcoming Orbiting Carbon Observatory mission to sit down and help me trace photons scattering about in a modeled atmosphere.

Thanks also, of course, to my family and friends for their support throughout my time here in the Department of Atmospheric Science.

Contents

List of Figures

List of Tables

Permission to include excerpts published in scholarly journals

• Figures and tables based on material copyrighted by the American Meteorological Society (AMS) are reproduced in compliance with the AMS copyright statement. The full statement is available at:

http://www.ametsoc.org/pubs/crnotice.html

• The article "A multi-purpose radar simulation package: QuickBeam" (Haynes et al., 2007) is included with written permission of the American Meteorological Society. Copyright 2007 American Meteorological Society.

• The article "Tropical oceanic cloudiness and the incidence of precipitation: Early results from CloudSat" (Haynes and Stephens, 2007) is included with written permission of the American Geophysical Union. Reproduced/modified by permission of the American Geophysical Union. Copyright 2007 American Geophysical Union.

• Figures and tables based on material copyrighted by the IEEE are reproduced in compliance with the IEEE Standards Association (IEEE-SA) copyright policy. The full policy is available at:

http://standards.ieee.org/IPR/copyrightpolicy.html

1 Introduction

1.1 Precipitation and the Global Climate System: Questions and key uncertainties

Precipitation is a key component of the climate system of the Earth, and an essential requirement for human life. How the distribution of fresh water on our planet might change under global climate change scenarios is not currently well understood, but increased drought and water stress in certain regions, due to changes in precipitation, evaporation, and runoff, may reach critical levels in the next centuries, especially in those parts of the world with rapidly developing populations (Arnell, 1999). The question of how water will be distributed on our planet in the future is an essential one from a human quality of life perspective; it is a crucial determining factor in where people can and can not live, where agriculture flourishes and where it doesn't, and how disease spreads amongst populations (Rosengrant and Cline, 2003).

This dissertation does not seek to answer the grandiose question of how the availability of fresh water will change on our planet in the next century. It does, however, address one very important component of this question. The ability to predict a change in the state of any variable, by definition, requires knowledge of the current state of that variable. This work seeks to address one important com-

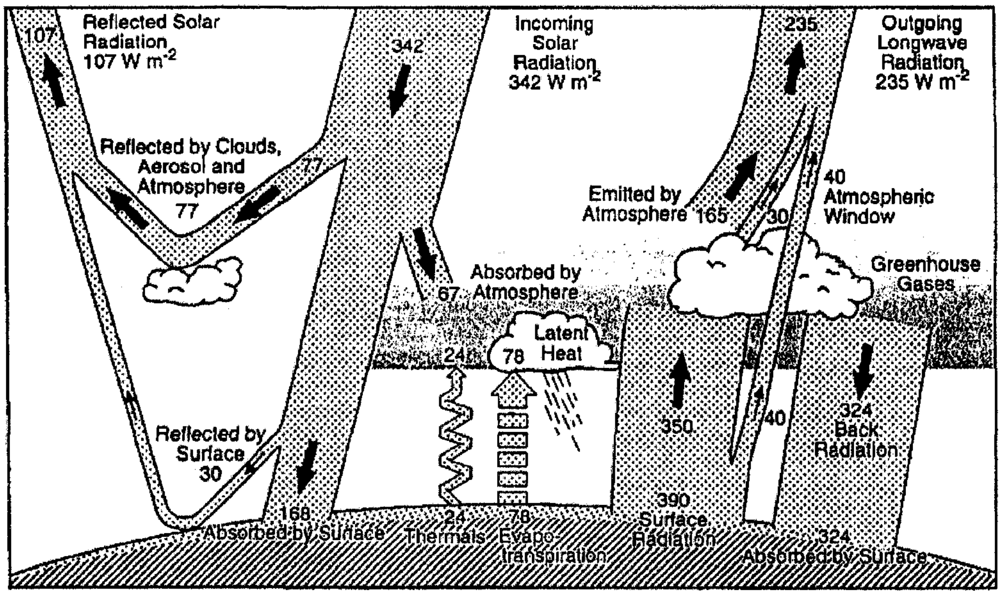

Figure 1.1: Earth's global mean annual radiation budget. From Kiehl and Trenberth (1997).

ponent of the current state of our global water cycle: precipitation. In particular it addresses new knowledge on how precipitation is distributed on our planet.

The global water cycle is driven by the sun. Figure 1.1 shows an approximate representation of the Earth's global mean annual radiation budget. The sun delivers a global mean 342 W m^{-2} of largely visible wavelength radiation to the top of the Earth's atmosphere, nearly half of which is transmitted through the atmosphere and absorbed at the surface. That which does not reach the surface is either reflected within the atmosphere by clouds, aerosols, or atmospheric constituents, or absorbed within the atmosphere (by water vapor and ozone, for example). The surface also reflects a small portion of incident radiation back to space.

The surface, in turn, radiates at its own temperature, and most of this energy falls in the infrared portion of the electromagnetic spectrum. Since the emissivity of the atmosphere is greater than 0.98 between approximately 5 and 20 μm, most of this radiation is absorbed (the foundation of the so-called greenhouse effect). The atmosphere itself radiates both to space and back toward the surface, and is such an effective emitter at infrared wavelengths that it carries a net radiation deficit of 102 W m^{-2}, continuously cooling accordingly. This deficit is accounted for by two factors: convection and conduction of sensible heat from the Earth's surface, and latent heating derived from the process of precipitation formation.

The global mean flux of latent heat into the atmosphere determines the global mean precipitation rate. Using the Kiehl and Trenberth (1997) estimate of $F_{LH} =$ 79 W m^{-2}, the precipitation rate required to balance this flux is given by $F_{LH}/(L_v \rho_w)$, where L_v is the latent heat of vaporization and ρ_w is the density of liquid water, resulting in a global mean rain rate of 3.0 mm day^{-1}. It is well accepted that nature's mean is near this value from both estimates of precipitation rate (Legates, 1995) and independent estimates of latent heat flux (e.g. Rossow and Zhang (1995) and Ohmura and Gilgen (1993)).

How this precipitation is distributed on the planet, both horizontally over the Earth's surface and vertically in the atmosphere, is not so well constrained. Measurements made since the start of the satellite age in the 1960's have gone a long way toward addressing these issues, but problem areas remain. The question of how often it rains at any given location on the Earth's surface is still not well understood. Although most models, for example, do produce a global mean precipitation rate in the vicinity of 3.0 mm day^{-1}, evidence suggests that many achieve the correct result for the wrong reasons. Dai et al. (1999) and Chen et al. (1996), for example, studied the diurnal convective cycle over the continental United States as predicted from climate model simulations and compared the results to observations. In the former study, the model overestimated precipitation frequency while underestimating intensity. The latter study pointed to the opposite problem; too much heavy precipitation but with far less frequency than indicated by observations.

(Sun et al., 2006) also studied precipitation frequency and occurrence over land using observations from a global database based on rain gauge and satellite precipitation estimates. These observations were then compared with results from eighteen global climate models. They found that for light precipitation between 1 and 10 mm day^{-1}, the models overall underestimated the occurrence of precipitation but still produced appropriate total accumulations. Above 10 mm day^{-1}, the models produced correct frequency of occurrences, but at too low an intensity. These issues predominantly point to the uncertainties generated by the parameterization and tuning of the precipitation process. In fact, climate models without cloud resolving capabilities appeal to convective parameterizations that generally treat clouds and precipitation as distinct entities rather that closely tied physical processes (Stephens and Kummerow, 2007).

Microphysical processes like condensation and collision-coalescence operating within clouds provide the pathway by which water vapor in the atmosphere is converted to precipitation. Future changes in precipitation can not, therefore, be quantified without first considering how the distribution and radiative properties of clouds on the planet may change (Stephens, 2005), and without first more fully understanding what types of clouds produce precipitation and which do not. Is deep, tropopause penetrating convection the main mode of precipitation generation in the tropical western Pacific region, or do shallower cloud systems also contribute in a significant way to precipitation in this area? Until the launch of CloudSat in April 2006 (described in detail in Chapter 2.1.1), high resolution global observa-

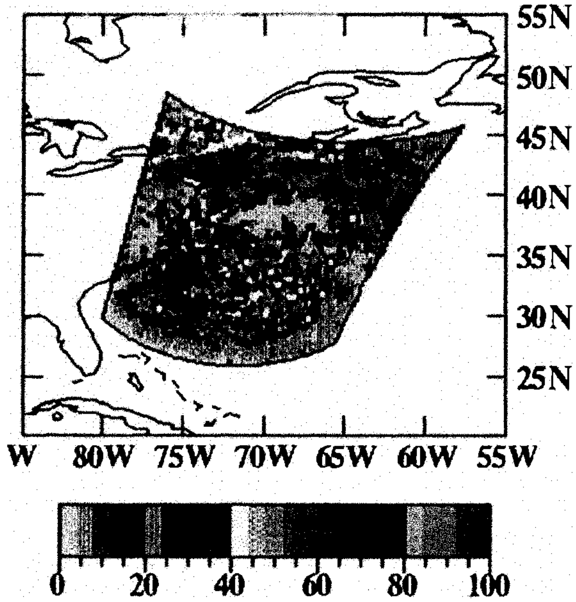

Figure 1.2: The pixels of a swath of microwave radiance data that are identified by different algorithms as precipitation. Pixels colored 100% are those for which all algorithms agree that rain is falling. From Stephens and Kummerow (2007).

tions of the vertical structure of clouds tied together with the precipitation they produced were not available.

Determination of the presence or absence of rain is not only a problem affecting models, but observational retrievals as well. Consider the suite of microwave precipitation algorithms that participated in the Precipitation Intercomparison Project (Smith et al., 1998). A swath corresponding to a set of microwave radiance observations off the east coast of the United States is shown in Figure 1.2, with colors indicating the percentage of participating algorithms that flagged precipitation as present. The variability is primarily a function of the liquid water path thresholds employed by the various algorithms as switches to determine the presence of precipitation. Whether or not precipitation is accumulated is determined by whether this switch is on or off.

Some very basic questions concerning how much precipitation falls outside of the tropics also remain. The most complete, authoritative observations of precipitation within the tropical belt are derived from the spaceborne suite of instruments composing the Tropical Rainfall Measurement Mission (Kummerow et al., 1998). Poleward of about 35° latitude, however, observational global-scale (i.e. including the oceans) precipitation estimates must be derived from passive microwave sensors like AMSR-E or infrared thresholding techniques. Passive microwave techniques such as those utilized in the Goddard Profiling Algorithm (Kummerow et al., 2001) become less reliable outside the tropics since they are based on the properties of tropical rain systems. Infrared precipitation estimates, such as the GOES precipitation index (Joyce and Arkin, 1997), can be subject to significant biases both in the tropics (e.g. Lui et al. (2007)) and especially at higher latitudes, since here the coldest clouds are less likely to be highly correlated with the areas of heaviest precipitation.

1.2 Statement of Purpose

The purposes of this dissertation are multifold:

- To introduce a new precipitation detection and intensity retrieval algorithm that is based on observations made by the W-band (94 GHz) Cloud Profiling Radar onboard CloudSat; and
- To demonstrate the feasibility and application of the algorithm to real-world observations; and
- To evaluate performance and uncertainties of the algorithm, particular against established rainfall estimates from other sensors; and

- To use the output of this algorithm to make new discoveries about how often precipitation occurs over the Earth's oceans, and to better understand how precipitation is distributed on the planet, particularly with regard to the light rainfall that CloudSat is best suited to observe.

The retrieval algorithm is an example of a broader category of methodologies referred to as surface reference techniques (SRT), whereby measurements of the Earth's surface are used to make deductions about hydrometeor content of the overlying atmosphere. The algorithm is novel in that it includes a built-in model of radar backscatter through the melting layer, and also includes the effects of multiple scattering of photons by ice and liquid particles. Multiple scattering is shown to be significant under certain circumstances for millimeter wavelength radars in the CloudSat configuration.

Application of this algorithm to CloudSat data provides new information about precipitation occurrence and distribution on our planet. This information is particularly novel when applied to the global oceans outside the tropics, since CloudSat is the first active sensor to regularly observe precipitation in the middle and higher latitudes.

1.3 Outline and Key Results

The backbone of this dissertation is a collection of three journal articles, two peer-reviewed and published, and one submitted for publication. Auxiliary material is provided to support these articles as necessary, particularly since journal articles are, by design, succinct, and must omit details that may interest some readers. This extra material is provided in the form of subsections after the referenced papers. Sometimes information is provided that expands upon or extends the content of the journal article.

Chapter 2 contains information about data sources used for the studies contained in this dissertation. This is followed by a description of the forward model for radar reflectivity, which is the principle measurement provided by CloudSat. The author has incorporated this into a publicly-available software package named QuickBeam (Chapter 3, (Haynes et al., 2007)). Chapter 4 contains an article describing the nature and methodology of precipitation incidence and detection from CloudSat as well as precipitation occurrence statistics collected over the near-global oceans (Haynes and Stephens, 2007). This includes results demonstrating the variability of precipitation efficiency across different regions of the globe. Chapter 5 contains an article describing the precipitation retrieval algorithm in detail, as well as some principle results (Haynes et al., 2008). This is followed by additional global precipitation accumulation results, focusing on the importance of light precipitation (Chapter 6). Finally, principle results are summarized in the conclusions (Chapter 7).

The key results presented in this dissertation are as follows:

- An attenuation based algorithm is described and applied to near-global CloudSat data.

- Multiple scattering is found to be significant for CloudSat when precipitation rates exceed 3 to 5 mm h^{-1}. This effect is included in the algorithm for up to 10 orders of scatter.

- Precipitation in the tropics prefers clouds with lowest-layer cloud tops near 2 and 15 km. A third mode, likely associated with congestus, is particularly common in the tropical western Pacific, Indian, and Atlantic ocean basins.

- There are vast regions of the globe where nearly all precipitation falls from cloud with lowest-layer tops below 4.75 km. Over the tropical oceans as a whole, precipitation falls twice as often from these clouds as any other cloud type.

- Multiple layered cloud systems are ubiquitous globally. They are responsible for a significant fraction of precipitation occurrence and accumulation. In the tropics, it is estimated that approximately half the accumulated precipitation comes from multiple layered systems.

- Approximately 0.16% of the tropical oceanic rainfall accumulated by CloudSat is due to rain falling at less than 1 mm h^{-1}.

- The CloudSat radar is the first meteorological space-based active sensor to view raining systems outside the tropics. It observes precipitation more often than the passive microwave AMSR-E, with greater resulting seasonal accumulation.

2 Data Sources

This chapter describes the instruments and data sets that are utilized throughout the dissertation. Observation platforms used in this study include the CloudSat millimeter wavelength radar, the CALIPSO visible wavelength lidar, the AMSR-E microwave radiometer on Aqua, and the Tropical Rainfall Measurement Mission (TRMM) precipitation radar and microwave imager. Model output from the European Centre for Medium Range Weather Prediction is utilized as part of the precipitation retrieval process. In addition, land surface types identified by the International Geosphere-Biosphere Programme are used to aide characterization of the Earth's surface as viewed from the CloudSat radar, and a suite of models that form the basis of the latest Intergovernmental Panel on Climate Change report are compared with CloudSat accumulated precipitation statistics. Finally, the Comprehensive Ocean-Atmosphere Data Set suite of ship-based meteorological observations are used for CloudSat rainfall validation purposes.

2.1 A-Train

The National Aeronautics and Space Administration (NASA) A-Train is a constellation of five satellites that fly in formation in a sun-synchronous orbit at approximately 705 km above mean equatorial sea level, with a repeat cycle of approximately 16 days (Figure 2.1). The chief benefit of formation flying is that it allows multiple sensors to make near-simultaneous measurements of the Earth's

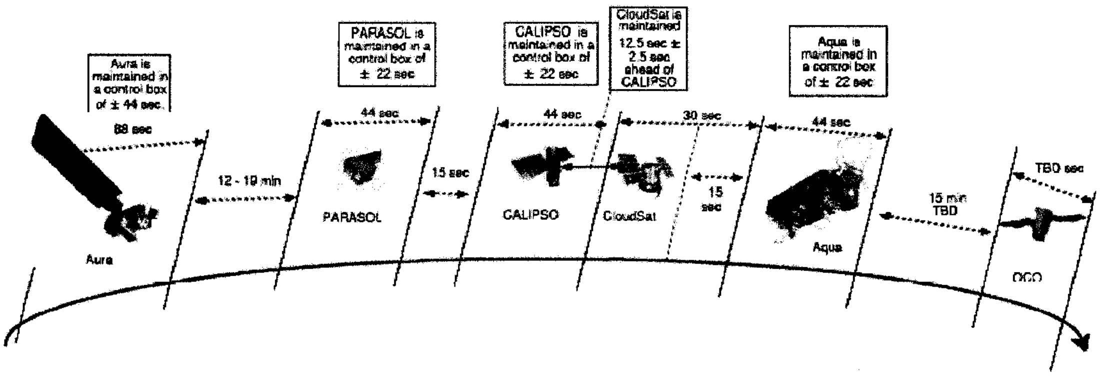

Figure 2.1: The A-Train formation flying configuration. From Stephens et al. (2008).

atmosphere in both space and time. Each of these sensors operates at a different frequency, with its own unique footprint and measurement characteristics, but the idea that the whole can be greater than the sum of its parts is leveraged by making near-coincident observations from multiple platforms. This dissertation will focus on the measurements made by sensors onboard three satellites in the A-Train constellation: CloudSat, CALIPSO, and Aqua.

2.1.1 CloudSat: Cloud Profiling Radar

CloudSat, launched in April 2006, contains the W-band (94 GHz) Cloud Profiling Radar (CPR). Not only is the CPR the most sensitive meteorological radar ever constructed, it is the first W-band radar to fly in space. The types of measurements provided by the CPR were long awaited by many in the Earth observation community. As the name suggests, CPR is an active, profiling radar system. Although the TRMM Precipitation Radar has the honor of being the first spaceborne radar system to make regular observations of the Earth system, the CPR is the first spaceborne radar system to provide a three-dimensional view of the structure of clouds.

The concept of "profiling" is well suited to active instruments, i.e. those which generate radiation, direct it at a target, and then measure the scattered radiation that returns to the antenna. The range to the target, r, is determined by the time t it takes for a pulse of emitted radiation to travel from the transmitting antenna back to the receiver ($r = c_0\, t/2$, where c_0 is the speed of light in a vacuum). Passive instruments, by contrast, measure radiation emitted and scattered by terrestrial objects (such as clouds, air molecules, and the surface of the planet). True ranging is therefore not possible, although measurements made at multiple frequencies with weighting functions that peak at different heights in the atmosphere can provide some information about vertical structure. As a result of this limitation, passive sensors have, to date, provided limited information about how hydrometeors are distributed in a vertical cross section through the atmosphere.

The CPR points near-nadir, but in practice three epochs characterized by different pointing angles have been utilized since launch. Until the beginning of July 2007, the CPR pointed 1.7° off nadir, which was then corrected to 0.0°. The quasi-specular reflection from the Earth's surface, however, resulted in extremely high surface backscatter. During August 2006, the pointing angle was changed slightly off nadir to 0.16°, and it has remained at this viewing geometry to date. During each of these epochs, the backscatter from the Earth's surface is markedly different, and these changes in surface reflectance must be accounted for in retrievals utilizing this signal.

Technical parameters for CloudSat and the CPR are provided in Table 2.1. Given the known antenna beam pattern (with a half width of 0.180 degrees) and a pulse width of 3.3 μs, the 6 dB range resolution is 485 m. Oversampling, however, is

Parameter	Value	Units
Orbit inclination	82.5	deg
Altitude	705-730	km
Operating frequency	94.05	GHz
Pulse width	3.3	μs
Range resolution (6 dB)	485	m
Antenna diameter	1.85	m
Cross-track resolution	1.32-1.38	km
Along-track resolution	1.7-1.72	km
Integration time	0.16	s
Data window	30	km
Range sampling	239.83	m
Peak power	1820	W
Pulse Rep. Frequency	3700-4300	Hz
Num. of integr. pulses	574-671	
Sensitivity	-30	dBZ

Table 2.1: CloudSat and CPR parameters. From Tanelli et al. (2008).

utilized to produce an effective range sampling of 240 m (Tanelli et al., 2008). One profile is obtained every 0.16 s, corresponding to a distance of 1.09 km on the surface of the Earth. The primary data CloudSat data product, 2B-GEOPROF, contains profiles of calibrated radar reflectivity (see Chapter 3.2 for details), gaseous attenuation (Chapter 3.6), normalized surface backscatter (Chapter 5.1.3), and the CPR cloud mask. The cloud mask is, itself, a tremendously valuable geophysical parameter provided by CloudSat (Mace et al., 2007). Values of the cloud mask are 0 (no cloud), or between 10 and 40 (increasing numbers representing higher likelihood of cloud presence). In this dissertation, cloud is considered present with high certainty when the cloud mask is 30 or higher (personal communication, Roger Marchand, University of Washington).

The minimum detectable signal of the CPR is approximately -30 dBZ, which is sufficiently sensitive to detect most clouds in the Earth's atmosphere. Two chief exceptions are optically thin cirrus and boundary layer clouds (discussed in detail in Chapter 4.2). The latter is not a sensitivity issue, but rather a result of contamination of atmospheric power returns by the extremely strong backscatter of the underlying surface. The radar is also extremely sensitive to the presence of precipitation, as will be demonstrated in Chapters 4 and 5.

The CPR is the primary tool that makes the precipitation detection and quantification algorithm described in this dissertation possible. The W-band frequency leads to more path integrated attenuation in rainfall than lower frequency radars like the TRMM Precipitation Radar. The attenuation is utilized as useful signal rather than discarded as noise. Over one year of data is available as of the time of this publication. The author has also generated an auxiliary data product for CloudSat named 2C-PRECIP-COLUMN, which is currently produced to match the profiling data available in 2B-GEOPROF.

2.1.2 CALIPSO: CALIOP lidar system

The CALIPSO satellite containing the CALIOP lidar systems flies approximately one minute behind CloudSat in the A-Train formation. CALIOP is an active sensor that emits a pulsed visible wavelength laser, at both 523 and 1064 nm (Winker et al. (2004), Winker et al. (2007)). Lidar systems are used for a variety of purposes in the physical sciences, including aerosol detection and quantification, water vapor retrieval (e.g. the Atmospheric Radiation Measurement Program Raman lidar system), and topographic mapping. In this study, the cloud detection capabilities of CALIOP are utilized.

Lidar systems transmit smaller pulse widths than the microwave radar systems used in this study (see Table 2.2), and as a result the vertical range sampling is at a higher resolution. In addition, due to the shorter wavelength, CALIOP is more

Parameter	Value	Units
Laser	Diode-pumped Nd:YAG	
Operating wavelengths	523, 1064	nm
Pulse energy	110	mJ
Repetition rate	20.16	Hz
Pulse width	20	ns
Linewidth	30	pm
Vertical resolution	30	m
Horizontal resolution	70	m
Polarization purity	$>$ 1000:1 (532 nm)	
Beam divergence	100	μrad
Boresight range	± 1 (1.6 μrad steps)	deg
Laser environment	18	psia

Table 2.2: CALIOP parameters. Courtesy NASA.

sensitive to small particles than the CPR, and as a result is a better detector of clouds. There are two caveats here; first, attenuation by hydrometeors is so strong at visible wavelengths that only the tops of all but the thinnest clouds can be detected. Second, CALIOP is sensitive to atmospheric aerosols as well as clouds, and differentiating the two can be difficult.

In this study, CALIOP is used to fill in the detection gaps of the CPR. The CloudSat 2B-GEOPROF-LIDAR product contains the fractional cloud coverage detected by the lidar within every CPR range volume. In practice, a combined CPR and CALIOP cloud mask may be obtained by combining the "cloud certain" category of the CPR with those volumes containing a 50% or greater CALIOP cloud fraction (Mace et al., 2007). This volume fraction requirement aims to minimize the impact of aerosol incorrectly classified as optically thin cloud. The combination of the CPR and CALIOP cloud masks represents the best information to date on how clouds are structured in the vertical on our planet.

Center freq (GHz)	6.925	10.65	18.7	23.8	36.5	89.0
Bandwidth (MHz)	350	100	200	400	1000	3000
Sensitivity (K)	0.3	0.6	0.6	0.6	0.6	1.1
Mean spatial res. (km)	56	38	21	24	12	5.4
FOV (km x km)	74 x 43	51 x 30	27 x 16	31 x 18	14 x 8	6 x 4
Sample rate (km x km)	10 x 10	10 x 10	10 x 10	10 x 10	10 x 10	5 x 5
Integration time (ms)	2.6	2.6	2.6	2.6	2.6	1.3
Main beam effic. (%)	95.3	95.0	96.3	96.4	95.3	96.0
Beamwidth (deg)	2.2	1.4	0.8	0.9	0.4	0.18

Table 2.3: AMSR-E parameters. From Marshall Space Flight Center web page.

2.1.3 Aqua: AMSR-E

AMSR-E is a passive microwave radiometer that operates at 6 frequencies centered between 6 and 89 GHz (information from Marshall Space Flight Center web page, see Table 2.3). It flies approximately 1 minute ahead of CloudSat in the A-Train configuration. The instrument scans conically over a range of 61 degrees around nadir, with a resulting swath width of 1445 km. In this study, AMSR-E derived-products including surface wind speed, precipitation rate, and surface type, were obtained from the National Snow and Ice Data Center. Surface wind speed (Wentz and Meissner, 2007) is reported at the 27 by 16 km resolution of the 18.7 GHz footprint, and precipitation rate (Kummerow et al., 2001) is reported at the 14 by 8 km footprint of the 36.5 GHz channel. Precipitation retrieval from AMSR-E uses the same methodology employed by the TRMM Microwave Imager; this will be discussed in Chapter 2.2.2.

Given the larger field of view, multiple CPR footprints correspond to a single AMSR-E footprint, and this makes the matching of geophysical variables associated with measurements from the two instruments difficult. To estimate wind speed at the location of the CloudSat footprint, the value of the AMSR-E pixel centered nearest to the CPR track is extracted. This procedure is also used for rainfall comparisons with the CPR, but greater caution must be used during interpretation of the results because rainfall generally has higher spatial variability than wind; rainfall, in addition to abruptly starting and stopping, may become heavier or lighter over very small horizontal distances, as dictated by the effects of topography, wind effects, and changes in the local microphysics. Figure 2.2 demonstrates the effects of this variability graphically for a shallow raining system observed by both the CPR and AMSR-E (parts a-c). Part (d) of the figure shows individual rainfall retrievals for the CPR (algorithm described in Haynes et al. (2008), Chapter 5) as small filled circles, and the corresponding AMSR-E rainfall retrievals as large filled circles. It is clear from this figure that the CPR is capable of resolving finer spatial variability of rainfall than is AMSR-E, and as a result the AMSR-E retrieved rain rate over the larger footprint tends (in this example) toward the average of the individual CPR retrievals. Furthermore, although the footprint-wide AMSR-E retrieval may be affected by rain observed by the CPR, the inverse is not true. Small scale variability outside the CPR path will still contribute to radiances observed by AMSR-E.

2.2 Tropical Rainfall Measurement Mission (TRMM)

The TRMM mission has provided the most complete and accurate estimates of tropical rainfall to date. The TRMM satellite orbits at 402 km above mean equatorial sea level and coverage extends to about 35° north and south latitude. Five instruments are used to quantify rainfall, lightning occurrence, and energy exchange within the Earth-atmosphere system. The two instruments used to provide estimates of rainfall are the Precipitation Radar (PR) and TRMM Microwave Imager (TMI). TRMM data is used for comparison and evaluation of the CPR

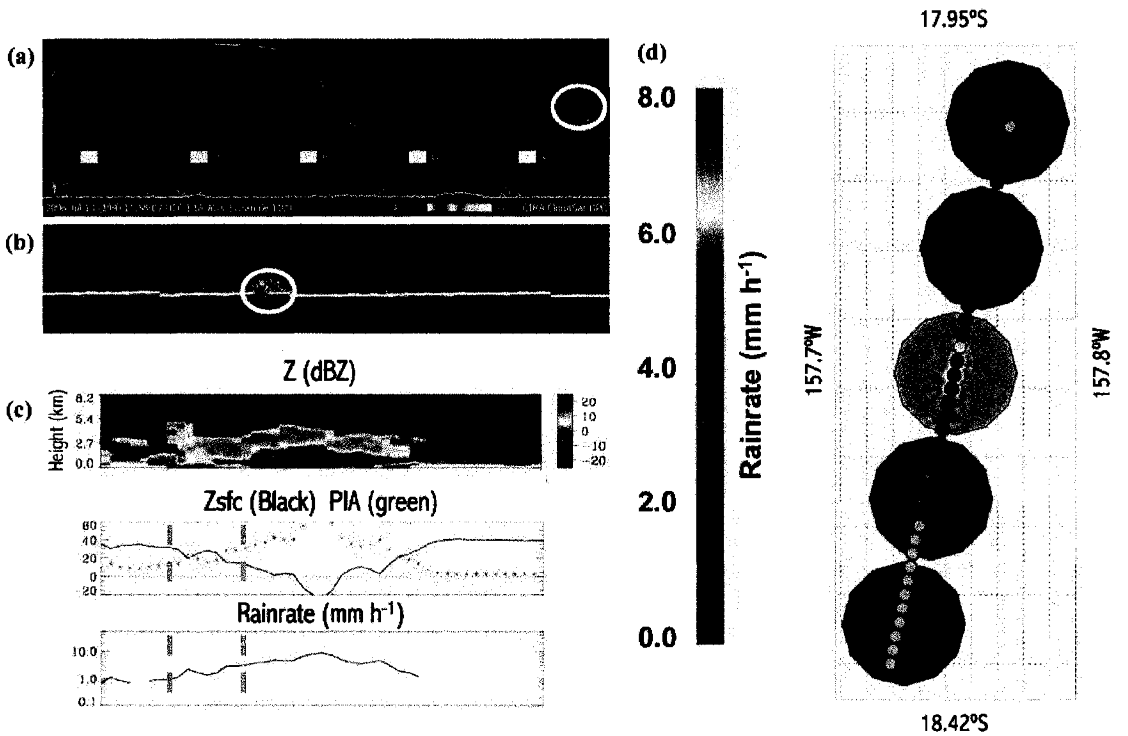

Figure 2.2: Example CPR rain retrieval from 2006 July 13. (a) Circle marking position of example case relative to the orbit; (b) Zoomed view of right-most purple section marked '2'; (c) CPR radar reflectivity profile, near surface reflectivity, path integrated attenuation, and derived rain rate; the set of orange lines represents the width of an AMSR-E footprint; (d) CPR precipitation retrievals (small circles) overlayed on AMSR-E retrievals (large circles), using the approximate size of the 36.5 GHz channel footprint. (Credit: with Tristan L'Ecuyer)

Parameter	Value	Units
Orbit inclination	35	deg
Altitude	402	km
Operating frequency	13.8	GHz
Range resolution	250	m
Horizontal resolution (nadir)	4.3	km
Swath width	247	km
Antenna diameter	2.0	m
Peak power	> 500	W
Pulse Rep. Frequency	2776	Hz
Sensitivity	0	dBZ

Table 2.4: TRMM and PR parameters. From Kozu et al. (2001).

precipitation algorithm.

2.2.1 Precipitation Radar

The PR is a Ku-band (13.8 GHz) radar system; specifications are given in Table 2.4 (Kozu et al., 2001). The instrument scans across track to approximately 17° degrees, resulting in a total swath width of 247 km, composed of individual horizontal footprints of approximately 4.3 km. At this frequency, the PR suffers from less attenuation effects than the CPR, and these effects are negligible in all but moderate to heavy rainfall.

When attenuation is negligible, a reflectivity-rainfall (so called Z-R) relation based on rain type is used to retrieve precipitation rate as a function of height in the atmosphere:

$$Z_e = \alpha_1 R^{\beta_1} \,, \tag{1}$$

where Z_e is the radar reflectivity, R is the rain rate, and α_1 and β_1 are parameters related to the rain type (stratiform or convective). For heavier rainfall, the reflectivity profile is corrected for attenuation before the Z-R relation is applied.

This is accomplished by finding a rain profile that satisfies a hybrid of the classic Hitschfeld-Borden solution for attenuating wavelength radars and the observed path integrated attenuation (PIA) estimated from the change in surface backscatter between a raining area and nearby non-raining area. The Hitschfeld-Borden method (Hitschfeld and Bordan, 1954) uses an assumed relationship between non-attenuated reflectivity and attenuation to correct the observed reflectivities at each range gate for attenuation effects. A variation on this procedure allows the additional constraint of observed PIA to effectively alter the parameters of the reflectivity-attenuation relationship, resulting in a more realistic solution (see Iguchi and Meneghini (1994), Iguchi et al. (2000)). The retrieval procedure is further complicated by a need to account for non-uniform beam filling effects. It is noteworthy that this rain retrieval algorithm is not directly translatable to CloudSat, because at the CPR frequency and viewing geometry there are *two* distinct effects that can produce departures of measured reflectivity from the "true" reflectivity: attenuation as well as multiple scattering. In certain circumstances these two effects can be of similar magnitude, and the latter is not easily dealt with analytically (discussed further in Chapter 5).

In this study, the PR 2A25 rainfall product was used for comparison with CloudSat at locations where orbits overlapped, and also to accumulate precipitation seasonally.

2.2.2 TRMM Microwave Imager

The TRMM Microwave Imager (TMI) is a five channel microwave radiometer with channels situated at similar frequencies (and with similar footprints) as those of the newer AMSR-E (Table 2.5). In fact, both instruments are able to make use

Center freq (GHz)	10.65	19.35	21.3	37.0	85.5
Bandwidth (MHz)	100	500	200	2000	3000
Polarization	V/H	V/H	V	V/H	V/H
Sensitivity (K)	0.63/0.54	0.5/0.47	0.71	0.36/0.31	0.52/0.93
FOV (km x km)	63 x 37	30 x 18	23 x 18	16 x 9	7 x 5
Integration time (ms)	6.6	6.6	6.6	6.6	3.3
Main beam effic. (%)	93	96	98	91/92	82/85

Table 2.5: TRMM TMI parameters. From Kummerow et al. (1998). V indicates vertical polarization, H indicates horizontal.

of the Goddard Profiling Algorithm (GPROF) to retrieve instantaneous rain rate ((Kummerow et al., 1996), (Kummerow et al., 2001)). The basis of this algorithm is a database of brightness temperatures constructed from a set of realistic tropical cloud hydrometeor and thermodynamic conditions simulated using a cloud resolving model (CRM). Bayes theorem is used to determine the probability that a particular rain profile, $\mathbf{R_z}$, is present given a set of brightness temperature observations, $\mathbf{T_b}$:

$$\Pr\left(\mathbf{R_z}|\mathbf{T_b}\right) = \Pr\left(\mathbf{R_z}\right) \times \Pr\left(\mathbf{T_b}|\mathbf{R_z}\right), \tag{2}$$

where the probability of this rain profile, $\Pr\left(\mathbf{R_z}\right)$, follows from the GCM simulations described above, and the probability of a set of brightness temperature observations given this rain profile, $\Pr\left(\mathbf{T_b}|\mathbf{R_z}\right)$, is a function of the physics operating at these frequencies.

At microwave frequencies, the ocean appears relatively cold because of its low emissivity. Emission from rainfall in the overlying atmosphere increases the brightness temperature at the top of the atmosphere (TOA) relative to emission from the underlying surface alone, and this forms the basis of the so-called emission-based algorithms. The lower frequency channels are preferred here because they do not saturate as quickly in heavy rain and are less sensitive to scattering by ice.

Over land, however, it is necessary to utilize the ice scattering signal because the emissivity of the underlying surface is much larger than that of the ocean, and as a result surface emission is indistinguishable from that emitted by the hydrometeors of interest. Ice scattering tends to reduce the brightness temperature at the TOA, and this signal is utilized by the scattering-based algorithms. As frequency increases, the ice scattering signature becomes more prominent (particularly so at 85 GHz). Scattering based methods can be used over land or ocean. GPROF considers both emission and scattering from hydrometeors to form the brightness temperature vector $\mathbf{T_b}$.

The TRMM 2A12 product contains TMI-based rain rates and forms the basis of the comparisons with CPR rain rate in later chapters.[1]

2.3 European Centre for Medium Range Weather Prediction forecast model output

For the primarily observationally-based study, models provide an invaluable means of providing geophysical information where measurement or *in situ* observations are not available. The European Centre for Medium Range Weather Prediction (ECMWF) forecast model analysis is used in this context. The model output is provided by ECMWF at approximately 60 km horizontal resolution at 61 vertical sigma levels. Model state variables are interpolated to the CPR track and provided in the CloudSat ECMWF-AUX product. The spatial interpolation is based on a bilinear interpolation of the four closest ECMWF grid points to the CPR track, which is then linearly interpolated in height between the two bounding ver-

[1]Much of this data was processed or provided by Wesley Berg of Colorado State University, whose assistance is greatly appreciated.

Variable	Use
Temperature	Freezing level height identification, gaseous attenuation calculation
Water vapor mixing ratio, atmospheric pressure	Gaseous attenuation calculation
Surface wind speed, sea surface temperature	Ocean surface backscatter calculation

Table 2.6: ECMWF parameters used for precipitation retrieval.

tical levels (the latter step is not applicable to surface variables). Finally, results from the two bounding forecast times are linearly interpolated to produce a final matched output product. Model variables used in the retrieval algorithm are listed in Table 2.6. More information on how these variables are used in the precipitation retrieval process is presented in the following chapters.

2.4 International Geosphere-Biosphere Programme Land Surface Type Database

The International Geosphere-Biosphere Programme (IGBP) land surface type product is a 10 km resolution database of surface type information derived from 1-km Advanced Very High Resolution Radiometer (AVHRR) data taken between April 1992and March 1993 [United States Geological Survey web site]. All land and sea surfaces are classified according to one of eighteen different types. These data are used in Chapter 5.1.3 to demonstrate how clear-sky surface backscatter observed by the CPR changes with different surface properties, and to characterize the variability associated with any given surface.

2.5 Comprehensive Ocean-Atmosphere Data Set

The COADS data set (Worley et al. (2005), Woodruff et al. (1987)) provides observational ship observations of meteorological conditions over large areas of the global oceans.[2] For the purposes of this study, ship reports for summer 2006-2007 were collected and analyzed for the occurrence of clouds and precipitation. Patterns of ship report density for the 1958-1991 period are shown in Figure 2.3. Major shipping channels, including most of the northern latitude oceans (Arctic Ocean excepted) are well covered by ship reports. Sampling in the southern oceans is more problematic; there are entire 2.5° latitude-longitude grid boxes without a single report in over 30 years of data collection.

Ship reports are excluded from the analysis when the provided quality check flag is not unity. This excludes reports where the sea-surface temperature is not within 2.5 standard deviations of the smoothed climatological mean for that location (this identifies mislocated reports (Petty, 1995)). Omitted station operation codes were considered to have no significant weather occurring (Dai, 2001).

Precipitation incidence is derived from the "ww" code. In general, lower values of these codes indicate a lower probability of precipitation, and higher values a higher probability. For example, code 23 indicates "rain and snow or ice pellets within past hour" while code 63 indicates "rain, not freezing, continuous, moderate at time of observation." Values used to indicate various degrees precipitation certainty are adopted from Petty (1995) and Dai (2001).

[2]COADS data used in this study were analyzed by Todd Ellis of Colorado State University.

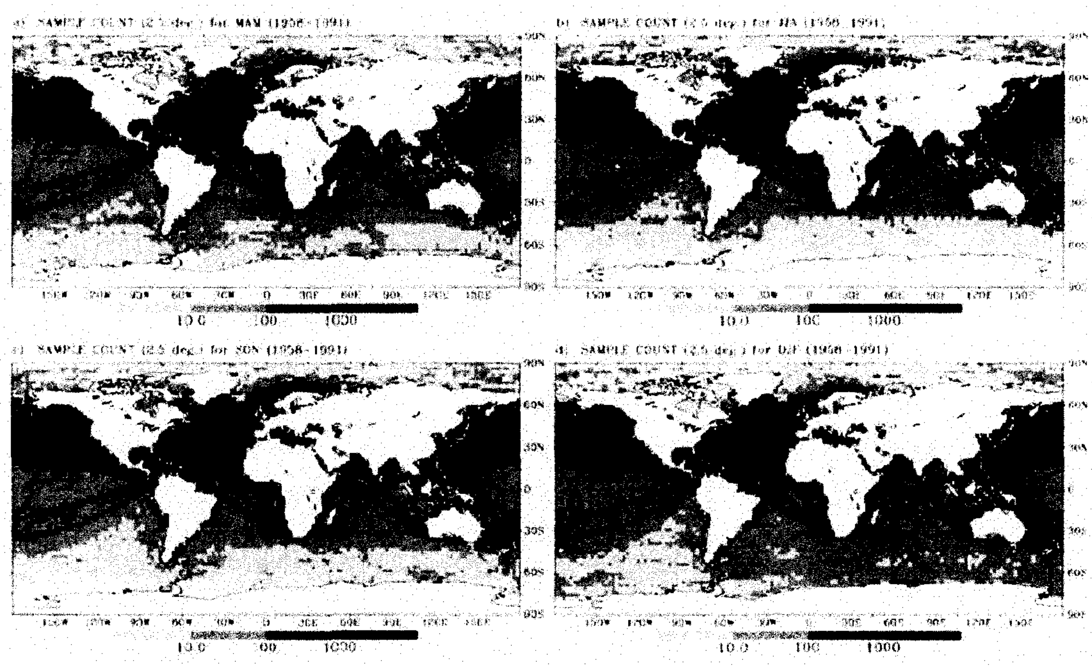

Figure 2.3: Count of ship reports per 2.5° latitude-longitude grid box. From Petty (1995).

3 A Forward Model for the Simulation of Radar Reflectivity: QuickBeam

The ability to model a radar reflectivity profile given a hydrometeor distribution in the atmosphere is of critical importance to understanding how a radar responds to meteorological targets in the atmosphere, and in solving the inverse problem in which retrieval of atmospheric constituents follows from forward model calculations. For these purposes, a radar simulator was developed. The model, named QuickBeam, is suitable for a wide variety of applications, including research, operational purposes, and application to model output. The following sections describe QuickBeam in detail, the background physics, and the assumptions that go into the production of a radar profile given some distribution of hydrometeors in the atmosphere.

This chapter contains the full text of an article published by the author in the Bulletin of the Meteorological Society that serves as a general overview to the simulator. This is followed by a more technical treatment of the radar equation and reflectivity modeling.

Text in section 3.1 is work published by the author (Haynes et al., 2007), and is reproduced with permission of the American Meteorological Society. Figure numbers, equation numbers, and citation styles have been changed for integration into the dissertation.

3.1 A multi-purpose radar simulation package: QuickBeam

3.1.1 Introduction

Since launch in April of 2006, CloudSat has provided the first near-global view of the three-dimensional structure of clouds from space. CloudSat, part of NASAs afternoon A-TRAIN constellation of satellites, flies a 94 GHz cloud radar that takes near-nadir measurements of the vertical structure of both cloud and precipitation systems from a sun-synchronous orbit approximately 705 km above the Earths surface (e.g. Stephens et al. (2002)). Observations of the variability of clouds over the surface of the Earth and through the depth of the atmosphere are creating a continually growing database that is useful for a broad range of meteorological applications, including evaluation of numerical prediction models and development of new and better convective parameterizations.

Meteorological radar systems transmit a pulse of electromagnetic energy and measure the backscattered energy that is returned to the radar dish. The backscatter occurs as a result of interactions with cloud and precipitation particles, as well as intervening atmospheric gases like water vapor and oxygen. The way electromagnetic radiation interacts with these particles is dependent on the frequency of the radiation, and the type, size, orientation, and distribution of the particles. The CloudSat cloud profiling radar (CPR) operates at 94 GHz and is therefore especially sensitive to cloud-sized particles. At this frequency, attenuation by water vapor is non-negligible and attenuation by precipitation can be significant. In contrast, lower frequency radars, such as those used in the NEXRAD system, operate closer to 3 GHz and are sensitive primarily to precipitation. Measurements of backscattered power are typically converted to the meteorological unit of radar reflectivity, expressed in decibels (dBZ). Retrievals of quantities like cloud water content or precipitation rate then typically follow from these reflectivity measurements.

Since CloudSat observations provide detailed information on the structure of cloud systems on a global scale, this information is especially valuable for evaluation of climate and weather prediction models. To compare modeled clouds to the new observations being made by CloudSat, it is useful to have a tool that converts modeled clouds to the equivalent radar reflectivities measured by the CPR. QuickBeam is a user-friendly radar simulation package that performs this function and is freely available to the meteorological community. Though developed with CloudSat in mind, it simulates a wide range of meteorological radar systems, including both spaceborne and ground-based systems, operating at frequencies between L-band and W-band (1 to 110 MHz).

3.1.2 The Simulator

(a) Reflectivity Simulations

To simulate a profile of radar reflectivities with QuickBeam, the user specifies a spectrum of mixing ratios of any number of hydrometeor species, including cloud and precipitation particles, as depicted in Fig. 3.1. These mixing ratios may be derived from sources such as numerical models or field observations. Each species of hydrometeor can have its own distribution, phase, and mass-diameter relationship. The user matches each of these mixing ratios to one of the built-in distributions,

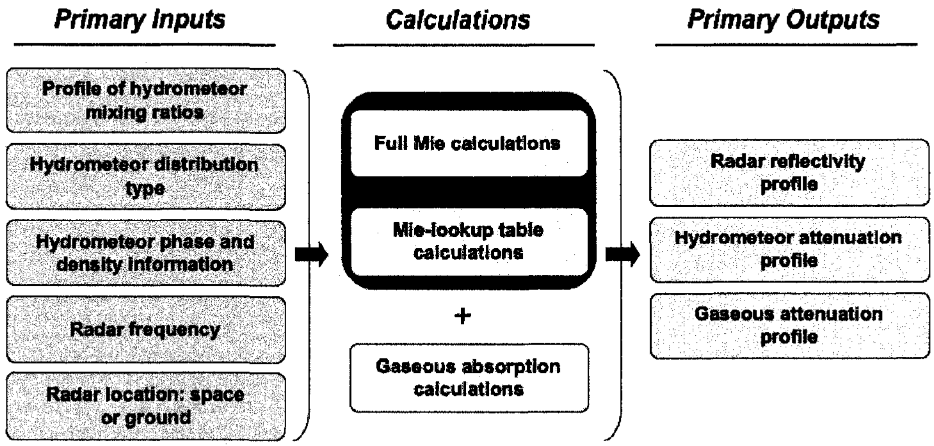

Figure 3.1: Flowchart showing the primary simulator inputs, calculations, and outputs.

including modified gamma, exponential, power law, lognormal, and monodisperse. The user must also input a profile of temperature and ambient relative humidity, or use one of the built-in tropical or mid-latitude profiles. This environmental sounding is used to calculate the absorption by atmospheric gases and thus the gaseous attenuation of the radar beam.

The simulator operates in two modes, either calculating particle scattering properties through full Mie calculations, or using pre-calculated lookup tables of the relevant scattering properties. Full Mie calculations, while more accurate, are computationally more demanding than using the lookup tables. Reflectivity error realized in using the lookup tables is generally less than 2 dB compared to the full Mie calculations.

At the present time all hydrometeors are treated as spheres with densities that vary with diameter in a way that can be specified by the user. The calculation of ice particle scattering properties is a universally difficult task for any microwave application, owing in part to uncertainty in the index of refraction of pure ice at low temperatures, the highly variable nature of ice-crystals shapes and densities, and also since ice often exists as a heterogeneous mixture with both air and melted liquid water. As an attempt to represent the dielectric properties of snow more accurately, the user may optionally specify a melted water content for snowflakes. Such a representation of melting ice particles is useful in the representation of the radar bright band, a region of enhanced reflectivity associated with the presence of the melting layer.

Following the calculation of hydrometeor scattering and absorption properties, the simulator outputs a profile of radar reflectivities, including both unattenuated reflectivity, and the reflectivity attenuated by other hydrometeors and gases between the radar and each range gate. When the simulator is applied to cloud scale model output, these attenuated reflectivities may then be compared directly with observed reflectivities from CloudSat or any other radar platform. To apply this simulator to a General Circulation Model (GCM) where the hydrometeor information is on a coarser scale, sub-grid scale sampling procedures are needed.

(b) Sub-grid scale sampling approach

The resolution of current climate models is of the order of 100 km, so these models are unable to resolve small-scale variability of atmospheric variables, particularly those of cloud fields. However, this sub-grid variability and how clouds overlap within the grid box significantly impact the transfer of radiation through the atmospheric vertical column. Therefore, it is necessary to account for the sub-grid variability in GCMs when simulating reflectivities for comparison with finer-scale observations.

One approach to accounting for this sub-grid scale variability is that of the

Subgrid Cloud Overlap Profile Sampler (SCOPS), developed for the International Satellite Cloud Climatology Project (ISCCP) simulator (see Klein and Jakob (1999), Webb et al. (2001)), but useful for producing sub-grid scale cloud features that may be input into a radar simulator as well. SCOPS samples the sub-grid distribution of clouds within a large-scale GCM grid box using a statistical, pseudo-random sampling algorithm. It provides a sub-grid distribution of clouds that is compatible with the grid box mean vertical profiles of cloud amount and the cloud overlap assumptions.

The Cloud Feedback Model Intercomparison Project (CFMIP), a joint effort by several climate modeling centers, is developing a community simulator for both CloudSat and the lidar platform CALIPSO. This project aims to provide a joint radar-lidar simulator designed to easily plug into a variety of weather prediction models, including high-resolution, cloud resolving models as well as climate models. QuickBeam is utilized as the component that simulates the radar reflectivity. As CloudSat is sensitive to precipitation as well as clouds, CFMIP also includes an algorithm that provides the sub-grid distribution of precipitation compatible with the SCOPS cloud distribution, although this part is currently under development.

3.1.3 Applications

To illustrate the capabilities of the simulator, it has been applied to two different global prediction models. One is the Multiscale Modeling Framework (MMF) GCM (also referred to as a superparameterization, see Randall et al. (2003)) in which most cloud parameterizations are replaced by a three-dimensional cloud-resolving model (CRM) embedded into each grid cell of the GCM on a coarse (approximately 4 km) grid. It is relatively straightforward to take the output of

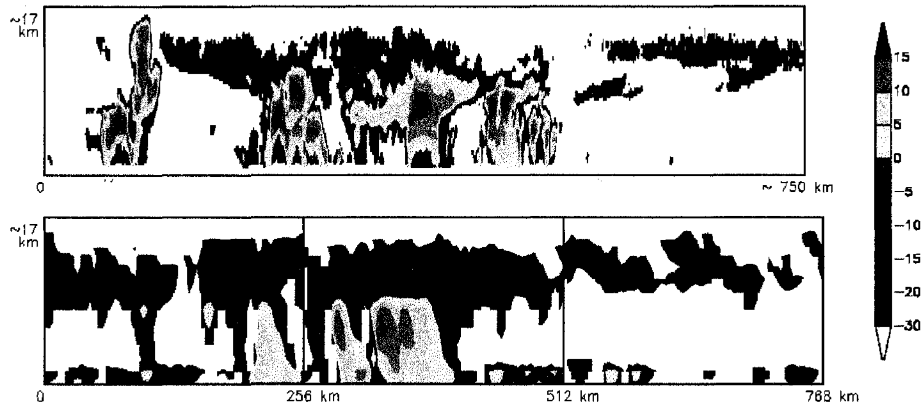

Figure 3.2: Examples of the observed versus simulated tropical convective systems over the Asian summer monsoon region. The upper panel is the radar reflectivity (in dBZ) observed by CloudSat with a horizontal span of ~750 km and vertical extension of ~17 km. The lower panel are selected MMF-simulated systems in three gridboxes within the same region with similar horizontal and vertical extension.

the embedded CRM and couple it to the simulator, thus making it possible to compare the results directly to CloudSat.

Such a comparison is illustrated in Fig. 3.2 for a tropical convective system over the Asian summer monsoon region. The modeled clouds and precipitation were produced by the CSU-MMF model (see Khairoutdinov et al. (2005)). It should be noted that the CSU-MMF is a climate model, and as such does not predict specific weather events. That is, the CSU-MMF was not being used to model the specific convective outbreak observed by CloudSat in the upper panel of Fig. 3.2 (although they do appear somewhat similar). Rather, the model aims at a faithful representation of the collective effects of individual weather events that compose the climate. A better way to compare climate model output to CloudSat observations is through the sort of longer term, broad region analysis presented in Fig. 3.3. Defining cloud occurrence as any time reflectivity exceeds a given threshold (-27.5 dBZ is used here), modeled cloud fraction can be compared to that observed by CloudSat. The figure is striking because it represents some of the first truly global observation of cloud vertical structures. The comparison of model output to observations in this way provides a snapshot of what the model is doing well, and likewise not so well. For example, though one may argue that the large-scale structures in Fig. 3.3 are for the most part well simulated by CSU-MMF, it is also apparent that the model overestimates the cloud fraction in the northern mid-latitudes and underestimates it in the southern subtropics. More detailed analysis of model biases will be discussed in an upcoming publication (see Marchand et al. (2008)).

A second example of application of the simulator to a GCM is shown in Fig. 3.4. Here the simulator is applied to the output of the UK Met Office global forecast model, which has a horizontal resolution of approximately 40 km at mid-latitudes. The sub-grid sampling approach described above has been applied and the grid-box mean radar reflectivity then obtained by averaging. The figure shows a transect through a mid-latitude depression in the North Atlantic on 2006 July 7. The upper panel shows the surface analysis valid at 18 UTC, with the approximate CloudSat track in red, from point A near the Azores to point B off the southeast coast of Greenland. CloudSat passed over a mature mid-latitude system that was traveling eastwards in the North Atlantic, first crossing the warm front and then the core of the system near the occluded front. The middle panel shows the radar reflectivity from CloudSat (dBZ), while the lower panel shows the simulated radar reflectivity. The vertical structure of the frontal system is very well represented by the model, which captures the deepening high clouds approaching the core of the system. The core is dominated by large-scale precipitation, which is also

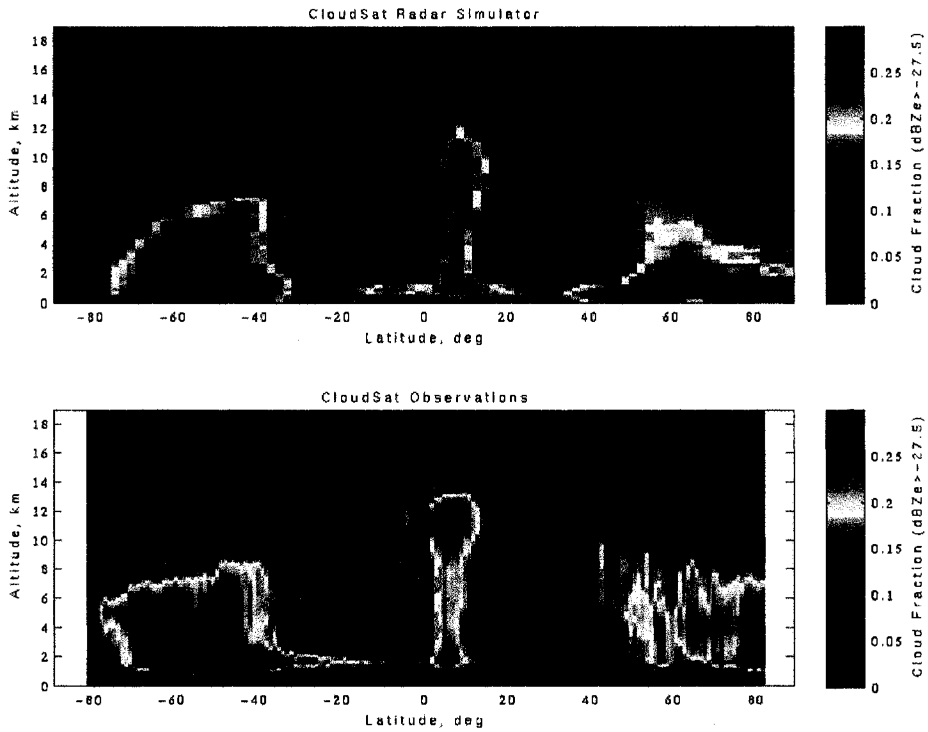

Figure 3.3: Monthly zonal profiles of cloud fraction (defined as reflectivity > -27.5 dBZ) for July simulated from the model (top panel) and from observations (bottom panel). Vertical axis is height above mean sea level (in km) and horizontal axis is latitude. CloudSat is a near-nadir pointing instrument and does not obtain full polar coverage.

reasonably well represented by the model. However, the model produces too much high-level cloud that extends towards the south (left in the image), beyond the area where it is present in the observations, and also produces low-level drizzling clouds in the warm sector beneath the high cloud, which is not observed by CloudSat. A detailed analysis of the application of the simulator to evaluation of cloud systems in the Met Office global forecast model is in progress (Bodas-Salcedo et al., 2008).

3.1.4 Planned updates to QuickBeam

Although spherical ice crystals are convenient because their electromagnetic properties are easily calculated from Mie theory, treating ice crystals as complex combinations of needles, plates, stellars, and aggregates allows for a more realistic simulation of their appearance to radar. Work is currently underway to better account for the various habits of ice crystals that are found in real clouds. One approach is the use of the discrete dipole approximation (DDA) to represent complex ice crystal habits as an array of interacting dipoles (see Shneider and Stephens (1995)). A lookup table incorporating DDA representations of various ice crystal habits is being developed and should be included in future versions of the simulator.

A methodology is also being developed to account for multiple scattering effects within the radar beam. Initial studies show CloudSat radar returns are significantly affected by multiple scattering when rain exceeds about 3 to 5 mm hr1. In these heavier rainfall events, photons may be scattered out of the radar beam and re-enter the beam at a later point in time through multiple scattering. This means that the power returned from a given radar pulse volume may include both the backscatter from particles within that volume and also power from earlier pulses

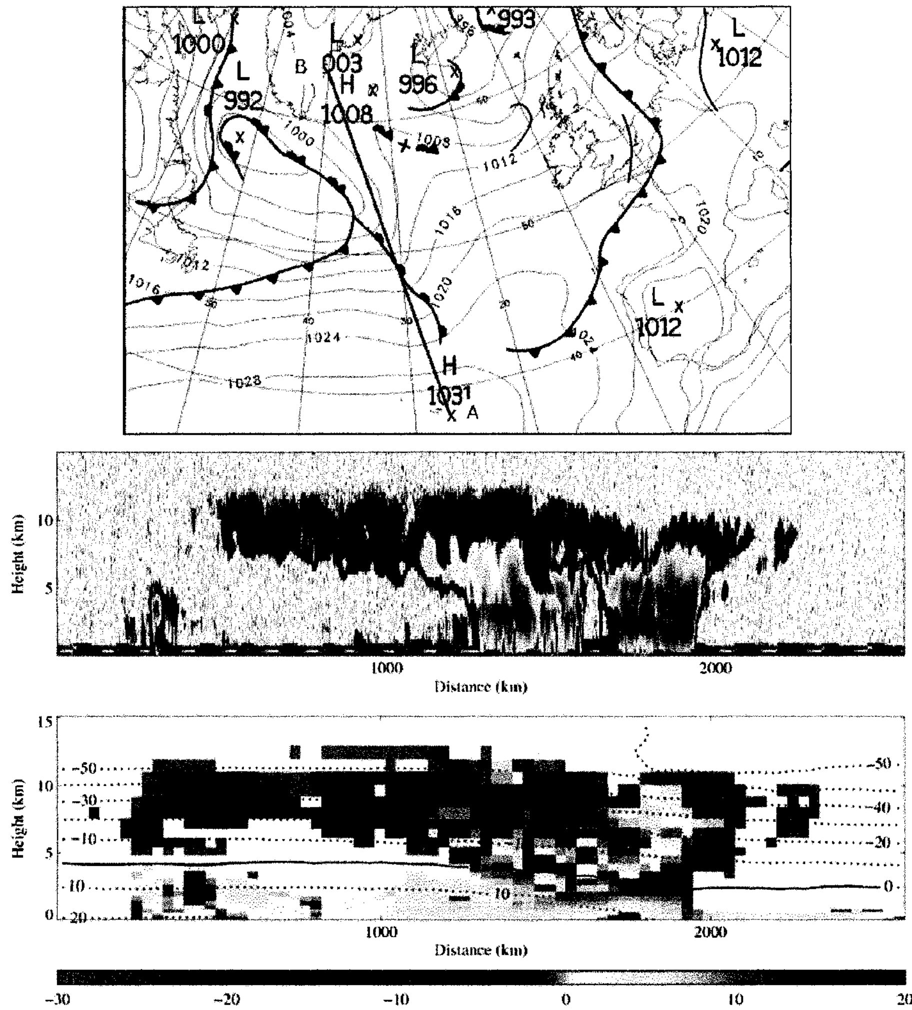

Figure 3.4: Example of simulated mid-latitude system in the UK Met Office global forecast model. The upper panel is the north Atlantic analysis chart at 18 UTC on 2006 July 7. The red line shows the CloudSat track, from A to B. The middle panel shows the radar reflectivity (in dBZ) observed by CloudSat. The lower panel is the simulated reflectivity from the model outputs. Isotherms are contoured, the solid line denoting the freezing level.

that underwent multiple scattering. Efforts are ongoing to parameterize this effect and make simulation of heavier rain at cloud radar frequencies more accurate.

3.1.5 Distribution

The source code is written in Fortran 90 and is thus highly portable to a wide variety of platforms. The package and a more technically oriented guide to the simulator can be downloaded from:

`http://cloudsat.atmos.colostate.edu/radarsim`

For more information about the community CloudSat/CALIPSO simulator, see:

`http://www.cfmip.net`

Acknowledgements

The development of the QuickBeam is supported under NASA contract #NNG06GC10G. Author Bodas-Salcedo is supported by the Department of Environment, Food and Rural Affairs under contract PECD 7/12/37, and thanks to Mark Ringer and Mark Webb for providing comments.

3.2 The radar equation

Pulsed radar systems operate by sending out a series of pulses of microwave radiation, generally in the frequency range of 1 to 110 GHz, and then receiving the backscattered radiation from a distribution of targets in the atmosphere. In general the power returned to a radar P_r which transmits with power P_t at wavelength

λ is given by

$$Pr = \left(\frac{P_t G^2 \lambda^2 \theta \phi h}{512(2 \ln 2) \pi^2 r^2} \right) \exp\left(-2 \int_0^r k_{ext} \, ds \right) \eta \,, \tag{3}$$

where G is the gain of the antenna, θ and ϕ are the vertical and horizontal half-power beamwidth of the antenna, h is the length of the emitted pulse, and r is the distance from the radar to the target volume. Here k_{ext} is the radar attenuation coefficient: this quantity, when integrated over range and multiplied by two to account for both the transmitted and return pulse, gives the attenuation due to all atmospheric components, including hydrometeors and gases, within the volume illuminated by the beam. η is the radar reflectivity and is given by

$$\eta = \int N(D) \, \sigma_b(D) \, dD \,, \tag{4}$$

where σ_b is the backscatter cross section of the particles and $N(D) \, dD$ denotes the number of particles with diameters between D and $D + \delta D$ in the target volume.

If the particles in the volume are small compared to the radar wavelength, i.e. the size parameter $x = \pi \mathrm{D}/\lambda \ll 1$, then the Rayleigh approximation may be used to approximate the backscatter cross section of a particle of diameter D as

$$\sigma_b = \frac{\pi^5}{\lambda^4} |K|^2 D^6 \,, \tag{5}$$

where $|K|^2$ is the dielectric constant of the target, a function of the complex index of refraction, m:

$$|K|^2 = \frac{m^2 - 1}{m^2 + 2} \,. \tag{6}$$

$|K|^2$ is generally assumed to be a constant for any radar system, but may vary from platform to platform even at the same frequency. It is typical to compute it assuming the target is a liquid droplet with a temperature of approximately 10 °C. Thus, at a frequency of 3 GHz, $|K|^2$ is often taken to be 0.93. At 94 GHz, a value closer to 0.67 is used.

With these expressions, the Rayleigh reflectivity can now be expressed as

$$\eta_{ray} = \frac{\pi^5}{\lambda^4}|K|^2 Z\,, \tag{7}$$

where Z is the radar reflectivity factor:

$$Z = \int_D N(D) D^6 dD\,. \tag{8}$$

It is important to note that because $|K|^2$ is defined with respect to liquid water, even pure ice targets that conserve the Rayleigh approximation will have a lower radar reflectivity factor than liquid water targets, the difference being a constant function of frequency. At 3 GHz, this offset is computed to be 7.23 dBZ, at 94 GHz is it approximately 6 dBZ.

In general, however, it can not be assumed that the Rayleigh approximation is valid for all targets viewed by the radar. The higher the frequency of the radar, the wider the variety of common meteorological targets that will violate this assumption. Consider a 500 μm long ice crystal viewed by a 94 GHZ radar, for example: here, the size parameter is approximately equal to 0.5 and the Rayleigh approximation fails. An exact expression for the radar reflectivity η is thus adopted. In general, the backscatter cross section of a spherical target of diameter D can be written:

$$\sigma_b = \frac{1}{4}\, Q_{sca} P(\Theta = 180)\, \pi D^2\,, \tag{9}$$

where Q_{sca} is the scattering efficiency, the ratio of the geometric to the electromagnetic cross section, and $P(\Theta = 180)$ is the scattering phase function evaluated for backscattered radiation. Substituting into (4),

$$\eta = \frac{1}{4} \int_D Q_{sca} P(\Theta = 180)\, \pi D^2 N(D) dD\,. \tag{10}$$

If we substitute the actual reflectivity η for the Rayleigh reflectivity η_{ray} in (7), and an effective radar reflectivity factor Z_e for the radar reflectivity factor Z, then

$$Z_e = \frac{\lambda^4}{4\pi^5 |K^2|} \int_D Q_{sca} P(\Theta = 180)\, \pi D^2 N(D) dD\,, \tag{11}$$

The effective radar reflectivity factor is the most commonly displayed output of weather radars, and it is common referred to, albeit erroneously, as simply 'reflectivity.' It should be noted that, by design, if a liquid target is illuminated with a small enough size parameter such that the Rayleigh approximation holds, then this quantity will equal the radar reflectivity factor Z.

Equation (11) strictly applies to a single range gate and neglects the effects of attenuation by atmospheric gases and hydrometeors between the radar and that range gate. However, these effects can be significant, particularly for radars operating at frequencies above 10 GHz. The attenuation of the beam between the radar and a target at distance r from the radar along path s can be written as

$$A_{ext}(r) = \exp\left(-2 \int_0^r k_{ext}(s) ds\right)\,, \tag{12}$$

where k_{ext} is the sum of attenuation coefficients due to atmospheric gases, $k_{ext,gas}$, and hydrometeors, $k_{ext,hyd}$ (see section 3.6). The effective radar reflectivity factor of any volume along the radar beam path is thus

$$Z_e(r) = \frac{\lambda^4}{4\pi^5|K^2|} A_{ext}(r) \int_D Q_{sca}(D)P(\Theta = 180)\,\pi D^2 N(D,r)dD\,. \qquad (13)$$

3.3 Radar target simulation

To calculate the reflectivity of a set of targets, the distribution and makeup of these targets must be specified. Meteorological targets include liquid cloud droplets and precipitation, ice clouds consisting of single ice crystals and collections of ice crystals, and ice in a variety of additional states such as snow, graupel, aggregates, and hail. Ice particles, in particular, are a challenge to model because they may contain some amount of air or liquid in addition to ice. Hailstones in a wet-growth environment, for example, contain a coating of liquid and thus have the scattering characteristics of a large ball of liquid water. The simulator allows hydrometeors to be classified into a variety of different classes, each of which can have its own distribution, phase, and mass-diameter relationship.

Unless one wishes to simulate an *in-situ* study where the actual particle distribution has been measured, then it is impossible to know all the parameters controlling the distribution of hydrometeors in a volume given a single quantity like ice water content or rain rate. Fortunately, decades of studies of the microphysics of clouds and precipitation allows us to make reasonable assumptions about these distributions that minimize the error of our results. The follow sections describe how hydrometeors may be distributed in the radar model and the parameters necessary to describe the distribution.

3.3.1 General distribution properties

Any particle distribution can be described in terms of $n(D)\,dD$, which is the number of particles with sizes between size D and $D + \delta D$. From this one can define a number of properties of the distribution. The total number of particles is

$$N_{tot} = \int_{D_L}^{D_U} n(D)\,dD\,, \tag{14}$$

where D_L is the smallest size particle in the distribution and D_U is the largest. The mean particle diameter is therefore

$$\overline{D} = \frac{1}{N_{tot}} \int_{D_L}^{D_U} n(D) D\,dD\,. \tag{15}$$

The water content in the distribution is

$$W = \int_{D_L}^{D_U} n(D)\,m(D)\,dD\,, \tag{16}$$

where $m(D)$ is the mass of a particle of diameter D, and the precipitating mass flux is

$$P_T = \int_{D_L}^{D_U} v(D)\,m(D)\,n(D)\,dD\,. \tag{17}$$

where $v(D)$ represents the fall speed of a particle of diameter D.

The mass density of the particles in a distribution is important for two reasons; first, it is directly related to the liquid or ice water content, and second, in the case of ice, the density contains information about how air or ice are mixed with the frozen particle. A commonly used parameterization of the mass-diameter relationship is that of Brown and Francis (1995), whereby the mass of particles can represented by power law relations of the form

$$m(D) = \alpha_m D^{\beta_m} , \tag{18}$$

The model allows specification of particle mass density in two ways, either through specification of α_m and β_m for each class of hydrometeor, or through use of a constant particle density. The density of a hydrometeor of diameter D is the ratio of the mass to the volume of the particle,

$$\rho(D) = \frac{6\alpha_m}{\pi} D^{\beta_m - 3} . \tag{19}$$

It should be noted that particle density is independent of size if β_m is equal to 3; this is taken to be true for all liquid hydrometeors.

Similarly, the fall speed of particles in the distribution may be parameterized by a power law of the form

$$v(D) = \alpha_v D^{\beta_v} , \tag{20}$$

Some values of α_m, β_m, α_v, and β_v reported by Locatelli and Hobbs (1974) for different types of hydrometeors are show in Table 3.1.

3.3.2 Modified gamma distribution

The modified gamma distribution is one of the most commonly assumed particle size distributions in modeling and retrieval applications. It is given by

$$n(D) = N_t \frac{1}{\Gamma(\nu)} \left(\frac{D}{D_n}\right)^{\nu-1} \frac{1}{D_n} \exp\left(\frac{D}{D_n}\right) , \tag{21}$$

where ν is the distribution width, N_t it the total number concentration of particles, and D_n is the particle characteristic diameter. Here the characteristic diameter is given by

$$D_n = \frac{\Gamma(\nu)}{\Gamma(\nu+1)} \bar{D} \, . \tag{22}$$

The mixing ratio r of any class of hydrometeors is thus

$$r = \frac{\alpha_m N_t D_n^{\beta_m}}{\rho_a} \frac{\Gamma(\nu + \beta_m)}{\Gamma(\nu)} \, , \tag{23}$$

which allows one to solve for either the total hydrometeor concentration or characteristic diameter given the mixing ratio of the hydrometeor. The precipitation mass flux is

$$P_t = \alpha_m \alpha_v N_t \frac{\Gamma(\nu + \beta_m + \beta_v)}{\Gamma(\nu)} D_n^{\beta_m + \beta_v} \, . \tag{24}$$

An example of a model which uses the modified gamma distribution for all hydrometeors is the Regional Atmospheric Modeling System (RAMS), parameters of which are shown in Table 3.1. Eight classes of hydrometeors are considered: small clouds drops, large clouds drops, pristine ice, rain, snow, aggregates, graupel, and hail. The distribution of hydrometeors is determined by specification of the mixing ratio, and in some cases temperature, for each of these hydrometeor classes within the radar volume.

3.3.3 Exponential distribution

The exponential distribution is commonly used to represent all kinds of precipitating and cloud water. It is given by

$$n(D) = N_0 \exp(-\lambda D) \, , \tag{25}$$

	α_m	β_m	α_v	β_v	D_L	D_H	ν	Specified
units	kg m$^{-\beta_m}$	-	m$^{1-\beta_m}$s^{-1}	-	μm	μm	-	-
Cloud 1	524	3	3173	2	2	40	2	$N_t = 0.3 \cdot 10^9$ kg^{-1}
Cloud 2	524	3	3173	2	40	80	2	$N_t = 0.3 \cdot 10^9$ kg^{-1}
Pristine ice	110.9	2.91	$5.769 \cdot 10^5$	1.88	15	125	2	(N_t is prognostic)
Rain	524	3	149	0.5	100	5000	2	$\bar{D} = 1$ mm
Snow	$2.739 \cdot 10^{-3}$	1.74	188.146	0.933	100	10000	2	$\bar{D} = 1$ mm
Aggregates	0.496	2.4	3.084	0.2	100	10000	2	$\bar{D} = 1$ mm
Graupel	157	3	93.3	0.5	100	5000	2	$\bar{D} = 1$ mm
Hail	471	3	161	0.5	800	10000	2	$\bar{D} = 1$ mm

Table 3.1: Parameters for the hydrometeor species used in RAMS.

where N_0 is the intercept parameter and λ is the slope parameter of the distribution. The total particle concentration is given by $N_{TOT} = N_0/\lambda$ and the mean particle diameter is $1/\lambda$. The mixing ratio is given by

$$r = \frac{\alpha_m N_0}{\rho_a} \frac{\Gamma(1+\beta_m)}{\lambda^{1+\beta_m}} , \tag{26}$$

and the precipitation mass flux by

$$P_t = \alpha_m \alpha_v N_0 \frac{\Gamma(1+\beta_m+\beta_v)}{\lambda^{1+\beta_m+\beta_v}} . \tag{27}$$

3.3.4 Lognormal distribution

The lognormal distribution is often appropriate for use in characterizing liquid cloud water distributions. It is defined here in terms of particle radius R rather than diameter for consistency with the CloudSat 2B-LWC algorithm:

$$n(R) = \frac{N_t}{\sqrt{2\pi}(\ln \sigma_g) R} \exp\left(-\frac{\ln^2(R/R_g)}{2(\ln \sigma_g)^2} \right) , \tag{28}$$

where R_g is the geometric mean particle radius, N_t is the total particle number concentration, and σ_g is the geometric standard deviation, i.e. $\sigma_g^2 = \overline{\ln^2(R/R_g)}$.

The mixing ratio of hydrometeors is thus given by

$$r = (2R_g)^{\beta_m} \alpha_a N_t \frac{1}{\rho_a} \exp\left(\frac{{\beta_m}^2 (\ln \sigma_g)^2}{2}\right) , \tag{29}$$

and the precipitation mass flux is

$$P_t = (2)^{\beta_m+\beta_v} \alpha_m \alpha_v N_t r_g^{\beta_m+\beta_v} \exp\left(\frac{(\beta_m+\beta_v)^2 (\ln \sigma_g)^2}{2}\right) . \tag{30}$$

3.3.5 Power law distribution

According to Ryan (2000), the population of small ice crystals with diameters from 20 to several hundred μm may be represented be a power-law distribution,

$$n(D) = a_r D^{b_r} . \tag{31}$$

The total concentration of ice crystals is given by

$$N_{TOT} = \frac{a_r}{1+b_r} {D_U}^{b_r+1} \left(1 - \frac{{D_L}^{1+br}}{{D_U}^{1+br}}\right) , \tag{32}$$

where D_U must be specified since the distribution does not tail off as diameter increases. The mixing ratio of hydrometeors is

$$r = \frac{a_r}{\rho_a g} {D_U}^g \left(1 - \frac{{D_L}^g}{{D_U}^g}\right) , \tag{33}$$

with $g = 1 + b_r + \beta_m$. The precipitation mass flux is then

$$P_t = \alpha_m \alpha_v \frac{a_r}{\beta_v + g} {D_U}^{\beta_v+g} \left(1 - \frac{{D_L}^{\beta_v+g}}{{D_U}^{\beta_v+g}}\right) . \tag{34}$$

Observations have shown that b_r can be characterized as a function of temperature, the parameterization of which is shown in Table 1 of Ryan (2000).

3.3.6 Monodisperse distribution

The simplest particle distribution of all is the monodisperse distribution, so named because all particles are of a single size, D_0, with a total concentration of N_0. The mixing ratio is thus simply

$$r = \frac{\alpha_m \, N_0 \, D_0^{\beta_m}}{\rho_a} \,, \tag{35}$$

and the precipitation mass flux is

$$P_t = \alpha_m \, \alpha_v \, N_0 \, D^{\beta_m + \beta_v} \,. \tag{36}$$

3.4 Particulate scattering calculations

To characterize the effective radar reflectivity factor it is necessary to calculate the backscatter efficiency Q_{sca} of all targets in the radar volume as well as the phase function in the backscatter direction, $P(\Theta = 180)$. For attenuation calculations the total extinction efficiency Q_{ext} is required as well. For spherical targets these calculations can be performed with a Mie scattering code (Bohren and Huffman, 1983). The simulator currently uses a routine written by R. Grainger and G. Thomas of Oxford University. Numerical integration of equations (12), (13), and (48) are performed from a series of calculated abscissa and ordinate values using a method based on overlapping parabolas.

To speed execution time, Mie tables containing values of Q_{sca} and Q_{ext} have been compiled for liquid and ice hydrometeors for a range of common radar frequencies (see Table 3.2), size parameters, ambient temperatures between -60 and

Band	Frequency (GHz)	Wavelength (cm)	Example
L-band	1 to 2	30.0 to 15.0	
S-band	2 to 4	15 to 7.5	NOAA NEXRAD (3 GHz)
C-band	4 to 8	7.5 to 3.8	
X-band	8 to 12	3.8 to 2.5	NASA EDOP (9.6 GHz)
Ku-band	12 to 18	2.5 to 1.7	NASA TRMM (13.8 GHz)
K-band	18 to 27	1.7 to 1.1	
Ka-band	27 to 40	1.1 to 0.75	ARM MMCR (34.9 GHz), PARSL (35 GHz)
V-band	40 to 75	0.75 to 0.40	
W-band	75 to 110	0.40 to 0.27	NASA CloudSat, NASA CRS (94 GHz)

Table 3.2: Radar band descriptions and examples. From IEEE Standard 521-1984.

30 °C, and ice fractions from 0.1 to 1.0.

3.5 Dielectric constant for mixed-phase hydrometeors

The dielectric constant ϵ is the square of the complex index of refraction m. To characterize the scattering and absorption by water particles, one must specify ϵ. This quantity is primarily a function of wavelength, temperature, and phase of the water substance. In the case of pure liquid, these values are quite well known, and the parameterization of Ray (1972) is used (see Figure 3.5).

Ice is universally more problematic in the microwave, owing primarily to the lack of laboratory studies of its optical properties in the microwave. Warren (1984) surveyed the optics literature and, utilizing best estimates obtained from combining the results of several independent studies, developed a series of tables that describe m for pure ice in the microwave region. Interpolation is performed to obtain values of m for any set of wavelengths and temperatures desired, as shown in Figure 3.6.

When water exists in a state that is neither purely ice nor purely liquid, but some combination of these mixed together with air, the scattering calculations become even more complex. Ice in the atmosphere is typically mixed in some

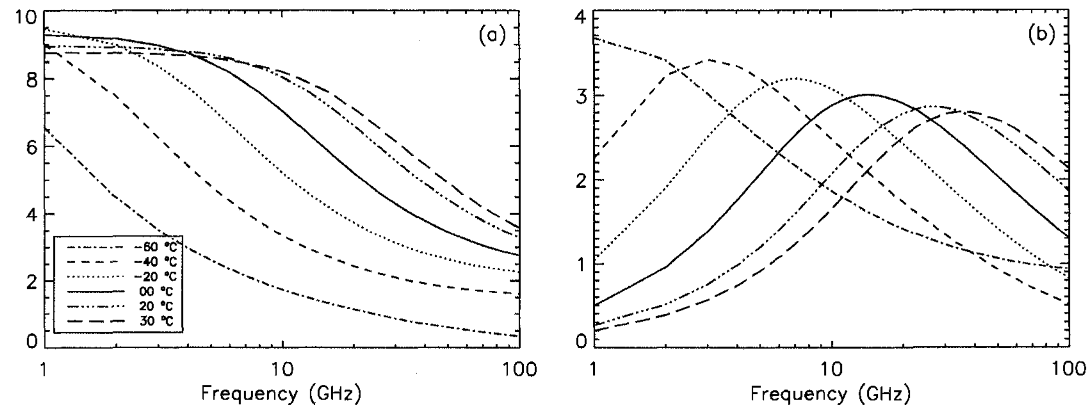

Figure 3.5: Real (a) and imaginary (b) parts of the complex index refraction of liquid water for a selection of frequencies and temperatures (°C).

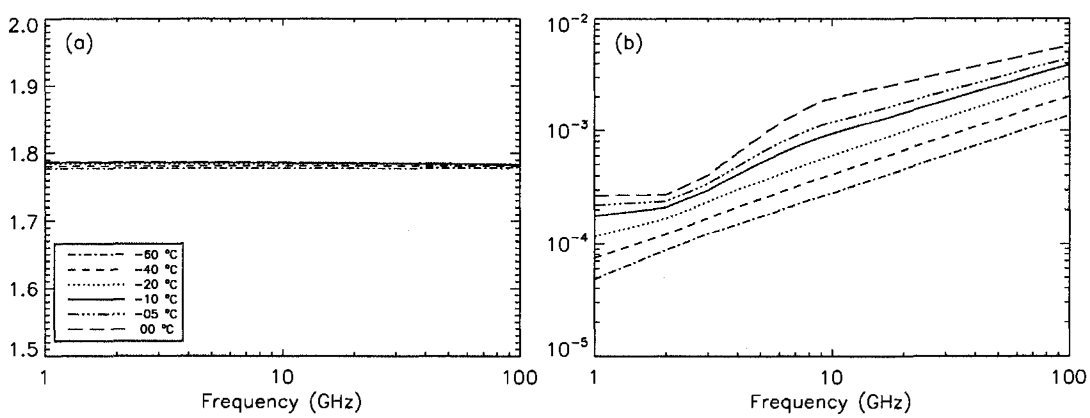

Figure 3.6: As in Figure 3.5, but for pure ice.

proportion with air such that its effective density, ρ_e, is less than that of pure ice, $\rho_i = 917$ kg m^{-3} (e.g. Heysmfield et al., 2004). Several methods have been developed to deal with this problem, but unfortunately each represents an approximation to the governing physics, and as such each produces a different result.

Most methods are some variation of the "matrix-inclusion" methodology, whereby the effective dielectric constant for a mixture of two materials can be calculated through knowledge of the ratio of the mean electric fields due to each component (Meneghini and Liao, 2000). For these methods it is assumed that one substance is a matrix, and is filled with embedded inclusions of the other substance. The way that embedded inclusions are distributed and the model for calculating electric fields differ depending on the method. Methods where the order of selection of matrix and inclusion affects the resulting dielectric constant are referred to as non-symmetric methods, and methods where the order of the components does not affect the result are known as symmetric.

For a mixture of more than two materials, this procedure is repeated (Petty, 2004). For example, consider a mixture of ice, air and water. One might first calculate an effective dielectric constant as ice inclusions in a water matrix, followed by air inclusions in a matrix of the ice-water mixture. This example demonstrates an ambiguity that naturally arises from all methods where more than two components are involved: the question of how the three components should be mixed together. The answer is not clear-cut, but will depend on the nature of the problem. In fact, for a mixture of three substances, there are 12 possible combinations of matrix and inclusion for non-symmetric methods; even symmetric methods may produce slightly different results.

Four methods for calculating the effective dielectric constant, ϵ_{av}, of a two-component mixture are summarized below, followed by a comparison of the methods and selection of the "winning" method.

- **Wiener's Theorem (symmetric)**

  Wiener's Theorem was one of the first methodologies applied to the problem of determining the refractive index of a combination of two distinct materials. Wiener hypothesized that the resulting electric field would be related to volume fraction-weighed contribution from each substance (Oguchi, 1983). The resulting expression is still one of the most common of the mixing formulas in use today:

$$\epsilon_{av} = \frac{-\epsilon_1\epsilon_2 + 2\epsilon_2 f_1 - 2\epsilon_2 - 2\epsilon_1 f_1}{\epsilon_1 f_1 - \epsilon_1 - \epsilon_2 f_1 - 2}\,, \tag{37}$$

  with ϵ_1 and ϵ_2 being the values of the dielectric constant for the first and second components, and f_1 begin the volume fraction of the first component. This method is symmetric in that it does not distinguish between matrix and inclusion.

- **Bruggeman (symmetric)**

  The Bruggeman formulation, also symmetric, is given by

$$f_1\,\frac{\epsilon_1 - \epsilon_{av}}{\epsilon_1 + 2\epsilon_{av}} + (1 - f_1)\,\frac{\epsilon_2 - \epsilon_{av}}{\epsilon_2 + 2\epsilon_{av}} = 0\,, \tag{38}$$

  where symbols are defined in the same way as Wiener's Theorem.

- **Maxwell Garnett (non-symmetric)**

The Maxwell Garnett formula is given by

$$\epsilon_{av} = \epsilon_m \left[1 + \frac{3f\left(\frac{\epsilon-\epsilon_m}{\epsilon+2\epsilon_m}\right)}{1 - f\left(\frac{\epsilon-\epsilon_m}{\epsilon+2\epsilon_m}\right)} \right], \tag{39}$$

with ϵ_m and ϵ being the dielectric constant of the matrix and inclusion, and f being the inclusion volume fraction.

- **Bohren-Battan (non-symmetric)**

  Using a similar methodology, Bohren and Battan (1982) considered the dielectric constant of a mixture of an elliptical set of randomly oriented inclusions of one substance embedded in a matrix of another. They found the dielectric function of such a mixture can be approximated by

$$\begin{aligned} \epsilon_{av} &= \frac{(1-f)\,\epsilon_m + f\beta\epsilon}{1-f+f\beta} \\ \beta &= \frac{2\epsilon_m}{\epsilon-\epsilon_m}\left[\frac{\epsilon}{\epsilon-\epsilon_m}\mathrm{C}\log(\epsilon/\epsilon_m) - 1\right], \end{aligned} \tag{40}$$

  where the notation is the same as used for the Maxwell Garnett formula, and Clog refers to the principle value of the complex logarithm. This methodology can be applied to a variety of situations. For the simple example of air embedded in an ice matrix (i.e. snow), this method reduces to exactly Wiener's Theorem. The differences between these two methods of calculating the dielectric properties of snow will be discussed later.

To compare these methods, a series of computations were performed using these four methods to calculate the effective dielectric constant of an air-ice mixture and water-ice mixture. The dielectric constant for the pure substances was

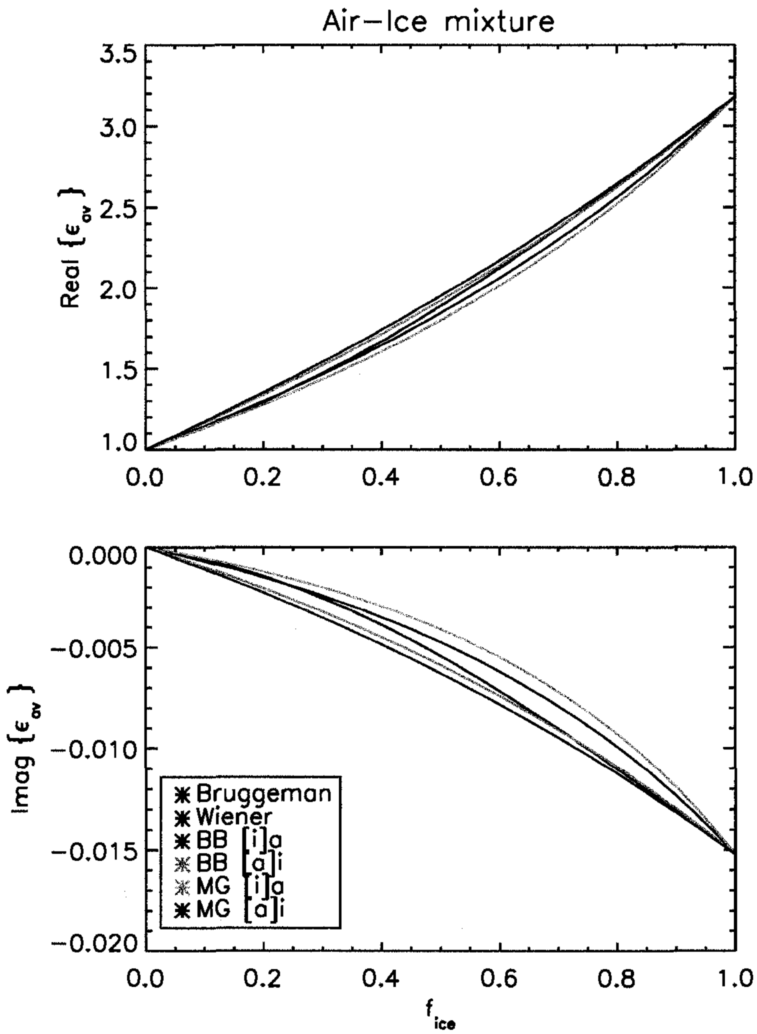

Figure 3.7: Real and imaginary parts of ϵ_{av} for an ice-air mixture at -5 °C for various volume fractions of ice, f_{ice}, using the four methods outlined in the text. BB refers to Bohren-Battan, MG to Maxwell Garnett. For the non-symmetric methods, the [bracketed] component is the inclusion, the remaining component is the matrix.

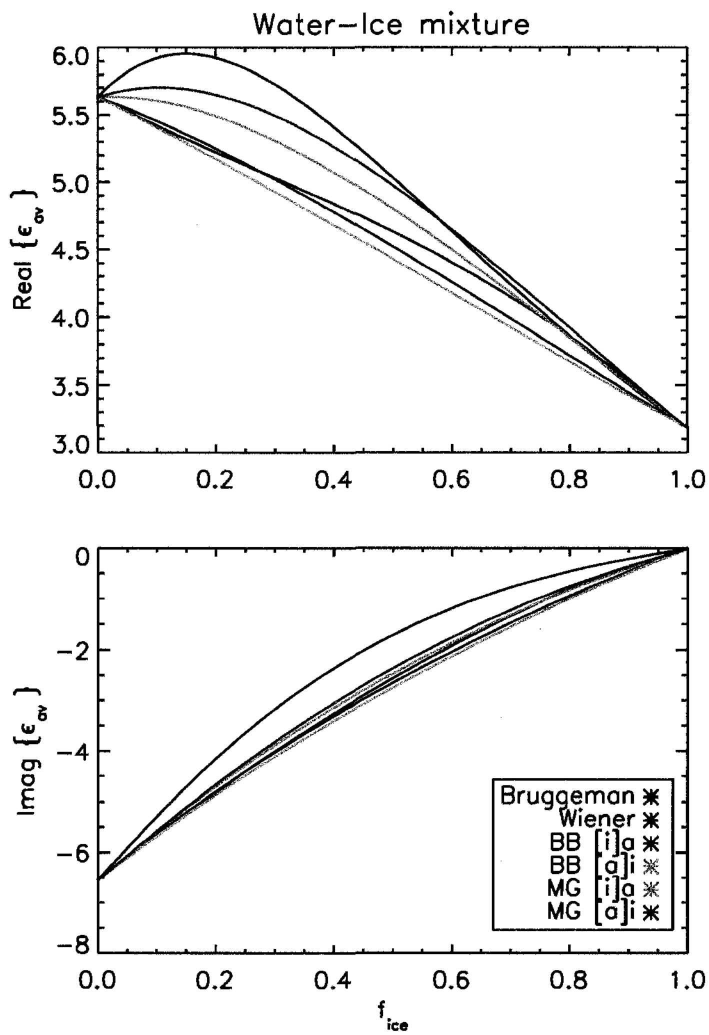

Figure 3.8: As in Figure 3.7, for a water-ice mixture.

computed from either Ray (1972) or Warren (1984). For the air-ice (i.e. snow) mixture (Figure 3.7), all methods agree reasonably for the real part of the dielectric constant, but differ slightly more significantly for the imaginary part, which is related closely to particle absorption. The Maxwell Garnett method is particularly sensitive to the choice of matrix and inclusion, its values generally at the high and low extreme of the other values. For both the real and imaginary parts of ϵ_{av}, the Bruggeman method exhibits the least variance and is bracketed by the other methods.

The water-ice mixture (Figure 3.8) exhibits significant deviations between the four methods, primarily for the real part of ϵ_{av}. In particular, Wiener's theorem with ice as the inclusion presents itself as a high outlier for ice volume fractions less than 0.5. It is noted that, again, the Bruggeman formulation provides a reasonable compromise between the various methods, being neither the low nor high outlier for any volume fraction of ice, but providing a smooth transition between the values for pure water and pure ice.

For this reason the Bruggeman method is chosen as the preferred method for calculating the effective dielectric constant for mixture of two components. Extending the Bruggeman theory to account for a third component is a simply a matter of extending equation (38) to account for another material (personal communication, P.T. Johnson; manuscript in preparation on this topic):

$$f_1 \frac{\epsilon_1 - \epsilon_{av}}{\epsilon_1 + 2\epsilon_{av}} + (1 - f_1) \frac{\epsilon_2 - \epsilon_{av}}{\epsilon_2 + 2\epsilon_{av}} + (1 - f_1 - f_2) \frac{\epsilon_3 - \epsilon_{av}}{\epsilon_3 + 2\epsilon_{av}} = 0 , \tag{41}$$

where f_2 is now the volume fraction of component 2 and ϵ_3 is the dielectric constant for component 3. Solving for this third degree polynomial can be accomplished by rewriting (41) as

$$\epsilon_{av}^3 + a_2\,\epsilon_{av}^2 + a_1\,\epsilon_{av} + a_0 = 0\,. \tag{42}$$

The solution for ϵ_{av} is then

$$\epsilon_{av} = w - \frac{p}{3w} - \frac{1}{3}a_2\,, \tag{43}$$

with

$$\begin{aligned} w &= \left(\frac{1}{2}\left[q + \left(q^2 + \frac{4}{27}\,p^3\right)\right]\right)^{1/3} \\ p &= \frac{1}{3}\,(3a_1 - a_2^2) \\ q &= \frac{1}{27}\,(9a_1a_2 - 27a_0 - 2a_2^3) \end{aligned} \tag{44}$$

and

$$\begin{aligned} a_0 &= -\frac{1}{4}\,(\epsilon_1\epsilon_2\epsilon_3) \\ a_1 &= \frac{1}{4}\,(\epsilon_1\epsilon_2 - 2\epsilon_1\epsilon_3 - 2\epsilon_2\epsilon_3) \\ &\quad + \frac{1}{4}\,f_1(-3\epsilon_1\epsilon_2 + 3\epsilon_2\epsilon_3) + \frac{1}{4}\,f_2(-3\epsilon_1\epsilon_2 + 3\epsilon_1\epsilon_3) \\ a_2 &= \frac{1}{2}\,(\epsilon_1 + \epsilon_2 - 2\epsilon_3) \\ &\quad + \frac{1}{2}\,f_1(-3\epsilon_1 + 3\epsilon_3) + \frac{1}{2}\,f_2(-3\epsilon_2 + 3\epsilon_3) \end{aligned} \tag{45}$$

3.6 Beam attenuation by atmospheric constituents

Although the scattering of radiation by particulate matter is a primary means by which we derive useful information from meteorological radar, the process of absorption can not be ignored, especially for higher frequency radars. Water vapor, oxygen, liquid cloud drops and rain drops, and even ice particles all absorb radiation at microwave wavelengths, and the reduction in power returned to the radar due to these attenuating species can be significant.

Gaseous absorption is treated using the empirical relationships of Liebe (1985). Spectroscopic data describing absorption lines of O_2 and water vapor are considered as well as the continuum region for dry air and water vapor. The oxygen spectrum is divided into resonance information for $N_a = 48$ oxygen lines, and the water vapor spectrum is similarly divided into $N_b = 30$ absorption lines:

$$N_f^{''} = \sum_{i=1}^{N_a}(SF^{''})_i + N_p^{''} + \sum_{i=1}^{N_b}(SF^{''})_i + N_e^{''} \, . \tag{46}$$

Here $N_f^{''}$ is the complex part of the refractivity for frequency f, S is the line strength, $F^{''}$ is the imaginary part of the line shape function, $N_p^{''}$ is the refractivity contribution from the dry air continuum, and $N_e^{''}$ is the contribution from the water vapor continuum. The dry air continuum considers contributions from non-resonant O_2 and pressure-induced N_2 absorption, and the water vapor continuum absorption is derived from more than 100 water vapor lines in the far wings. The specific attenuation $k_{ext,gas}$ in decibels per kilometer is then

$$k_{ext,gas} = 0.182 f N_f^{''} \, . \tag{47}$$

Absorption by hydrometeors can also significant, and at higher frequencies may lead to total attenuation of the beam in even moderate rainfall (e.g. L'Ecuyer and Stephens, 2002). The volume extinction coefficient is defined as

$$\sigma_{ext} = \frac{1}{4} \int_D Q_{ext} \, \pi D^2 N(D) dD \, , \tag{48}$$

where Q_{ext} is the extinction efficiency from Mie calculations or some other suitable source. This is converted into a specific attenuation by a multiplicative constant:

$$k_{ext,hyd} = 0.4343 \times 10^4 \, \sigma_{ext} \, , \tag{49}$$

such that the total attenuation coefficient due to gases and hydrometeors is

$$k_{ext} = k_{ext,gas} + k_{ext,hyd} \, . \tag{50}$$

4 Precipitation Incidence: One Year of Near-Global Results

The question of how often precipitation occurs on our planet is one that CloudSat is well-suited to address. This chapter contains an analysis of precipitation occurrence for one year of CloudSat observations. The first section contains work published in Geophysical Research Letters showing precipitation occurrence results for June-July-August (JJA) 2006. A crude estimate of the regional variation of precipitation efficiency of clouds is also discussed. The precipitation occurrence algorithm is described briefly in this work, but is greatly expanded upon in Chapter 5.1.4.

An analysis for the remainder of 2006 and the first half of 2007 is provided immediately following the article in Chapter 4.2. Notably, this analysis also includes cloud boundary information from the CALIPSO lidar platform.

4.1 Tropical oceanic cloudiness and the incidence of precipitation: Early results from CloudSat

Text in section 4.1 is work published by the author (Haynes and Stephens, 2007), and is reproduced with permission of the American Geophysical Union. Figure numbers, equation numbers, and citation styles have been changed for integration into the dissertation.

4.1.1 Abstract

Results of analysis of CloudSat radar data collected during the first three months of operation are described. It is shown that the global tropical oceans (30N-30S) predominantly favor clouds with tops in two layers centered at about 2 and 12 km. Precipitating clouds occur primarily in three modes, a shallow mode that is the most frequent type, as well as a middle and deep mode. Regional features are also discussed. The Indian and western Pacific Oceans exhibit more predominantly high clouds and deeper precipitation features than the eastern Pacific and Atlantic. The occurrence of a mid-level mode of cloudiness and precipitation is shown to vary regionally, being most evident in areas favoring deep convection. For all regions examined, precipitating clouds are observed to be deeper than non-precipitating clouds. Over the global tropical oceans, 18% of the clouds detected by CloudSat produce precipitation.

4.1.2 Introduction

Tropical convection exerts a fundamental control on our climate system. Convection is responsible for most of the precipitation that falls in lower latitudes. Convective cloudiness has a profound influence on the radiation budget of the lower latitudes, and a number of studies suggest that such influences may be the principal means of regulation of tropical sea surface temperatures (e.g. Ramanathan and Collins (1991); Lindzen (2001); among several others, for review see Stephens (2005)). Convective clouds are also an elementary source of heat that fuels the tropical atmospheric circulation (e.g. Gill (1980); Lau and Peng (1987); many others). Much remains to be understood about tropical cloudiness, the way clouds heat the atmosphere, and how convective cloud systems in particular distribute their heating influence vertically (e.g. Zhang (2005)). This understanding requires more quantitative information about the vertical distribution of clouds and precipitation structures.

On April 28, 2006 the CloudSat satellite carrying a millimeter radar system (the Cloud Profiling Radar, CPR, Im et al. (2005)) designed expressly for the vertical profiling of hydrometeors, was launched from Vandenberg Air Force Base. Both CloudSat and the lidar satellite CALIPSO were inserted into nearly identical orbits each approximately 1 minute behind the NASA Earth Observing System (EOS) Aqua satellite and in formation with the French PARASOL satellite and the EOS Aura satellite. This creates the A-Train satellite constellation (Stephens et al. (2002)). In this note we report early results from the analysis of the first three months (June-July-August, JJA) of the Level 2B Geometrical Profiling product of CloudSat (hereafter 2B-GEOPROF). A simple method to identify precipitation is also introduced and is applied to the 2B-GEOPROF data to provide novel, global-in-scale information about tropical cloudiness and its related precipitation.

4.1.3 The CloudSat 2B-GEOPROF Data

The CloudSat data products (Stephens et al., 2002) are available at the CloudSat data processing center (http://cloudsat.cira.colostate.edu). Two important products currently available are the 1B-CPR product which contains the calibrated raw power profiles measured by the CPR, and the 2B-GEOPROF product now briefly described (see also Mace et al. (2007)). The 2B-GEOPROF product contains two main types of information. The first is the cloud mask information that identifies where hydrometeors occur in individual profiles over the instrument noise floor. The cloud masking algorithm is similar to the algorithm developed by Clothiaux et al. (2000) except that a power probability weighting scheme and an along-track integration scheme have been added. This mask information is used in this study to identify cloud layers and their tops. The second type of information is the radar reflectivity, expressed in dBZ, associated with the mask.

The characteristics of the 2B-GEOPROF product are largely determined by the properties of the CPR. The CPR operates at the frequency of 94 GHz and points nominally in the nadir direction only. The vertical resolution determined by the pulse length is approximately 480 m but backscattered signals are oversampled to produce a range gate spacing of 240 m. From a 705 km orbit, the instantaneous field of view of the CPR at mean sea level is 1.4 km across-track. At least 540 pulses are averaged to produce a nominal along-track footprint of 2.5 km. The volume defined by this footprint and the 240 m range bin is referred to as the radar resolution volume (RRV). Another important characteristic is the radar minimum detectable signal (i.e. MDS). The mission requirement for the MDS was -28 dBZ at the beginning of the mission for nominal pulse averaging. Estimates since launch suggest an MDS between -30 dBZ and -31 dBZ, varying with position along the orbit.

4.1.4 Precipitation Incidence

The power backscattered by atmosphere in any RRV and returned to the CPR is highly sensitive to the presence of precipitation both by scattering within the RRV and by attenuation between the RRV and the CPR. At the frequency of the CloudSat radar, the two-way path integrated attenuation (PIA) of the radar occurs due to a combination of absorption by gases such as O_2 and H_2O, and absorption and scattering by cloud and precipitation sized particles. The gaseous attenua-

(a) 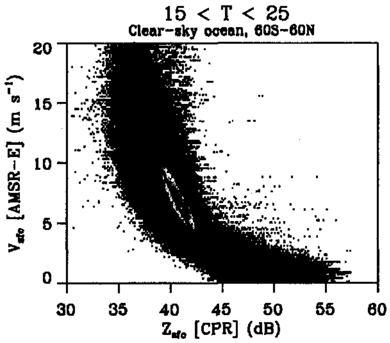

(b) 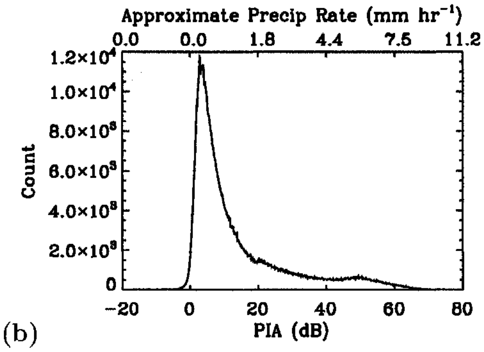

Figure 4.1: (a) The relation between observed ocean surface backscatter and AMSR-E surface wind speed. The red line represents the mean, the black dashed lines one standard deviation from the mean. (b) The probability distribution of path integrated attenuation due to precipitation derived for CloudSat observations collected during JJA over the tropical oceans between latitudes of 30N and 30S. An approximate precipitation scale is included for reference.

tion, determined from the available temperature and moisture profiles taken from ECMWF analyses matched to the CPR footprint, is also provided as part of the 2B-GEOPROF data product. The attenuation by liquid cloud droplets varies systematically with cloud liquid water path with values approaching 1-2 dB and sometimes higher for typical liquid water content values and cloud thicknesses (Stephens et al., 2002). The combined effects of these two contributions can be accounted for within approximately ± 0.5 dB. The PIA due to liquid precipitation is significantly larger than the combination of these two contributions (Fig. 4.1b).

The PIA is derived as the difference between the values of surface backscatter observed under precipitating clouds and the value of an equivalent clear-sky ocean surface backscatter. The latter is estimated over oceans using an appropriate model of the surface backscatter (e.g. Li et al. (2005)) or, as in this study, by developing a database directly from observations. Fig. 4.1a illustrates the relation between observed clear-sky surface backscatter corrected for gaseous attenuation and the AMSR-E wind speed and SST data. The equivalent clear-sky surface reflection under storms is derived from this relationship given the SST and surface wind taken from NOGAPS analysis (Staudenmaier, 1997). This value of surface backscatter is then adjusted to account for the non-precipitation contributions to attenuation thus producing an effective precipitation-free surface backscatter (σ_0).

The method described is similar to that used to produce estimates of attenuation from the TRMM Precipitation Radar (e.g. Marzoug and Amayenc (1994), Amayenc et al. (1996)). It suffers from a combination of uncertainties arising from gaseous and cloud contributions, as well as uncertainties in the relationship between wind speed, SST, and σ_0 as shown in Fig. 4.1a. We estimate this combined uncertainty to be approximately ± 2 dB.

The presence of precipitation is determined primarily by PIA,

$$PIA_{precip} = \sigma_0 - \sigma,$$

where σ is the observed attenuated surface backscatter below the precipitating cloud. When PIA_{precip} is larger than a threshold value, taken here to be 20 dB, precipitation is deemed to be present with high certainty. When it is less than this value, it is required that a reflectivity echo greater than 0 dBZ be present in the lowest atmospheric range gates (e.g. Stephens and Wood (2007)). The probability distribution of the two-way PIA over the global tropical oceans between the latitudes of 30N and 30S is shown in Fig. 4.1b. This distribution exhibits a bimodal structure implying that the frequency distribution of tropical surface precipitation is also bimodal in nature. The scale at the top of the figure provides a qualitative reference scale for interpreting PIA in terms of precipitation rate

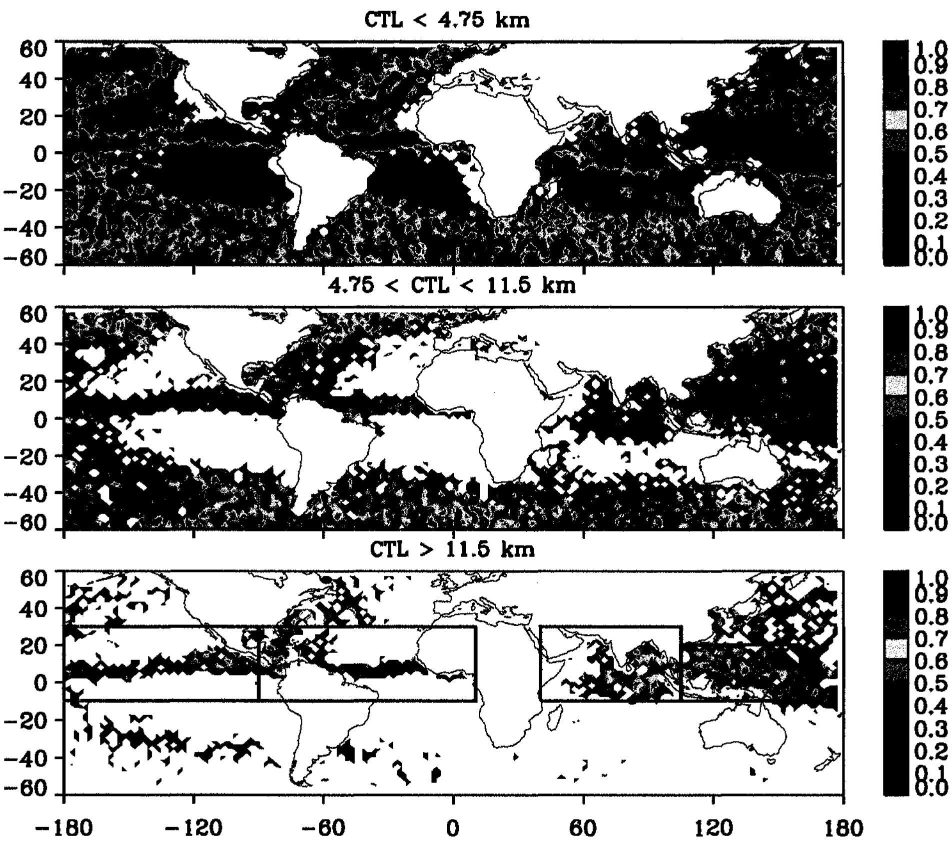

Figure 4.2: The relative frequency of precipitation occurrence grouped by the cloud top height of the lowest layer (CTL) for JJA. For any given grid box, the sum of the three occurrences is unity. On the bottom panel, four regions are defined by boxes: from left to right, the eastern Pacific, Atlantic, Indian, and western Pacific.

for reference only. Developing more quantitative methods for converting the PIA information into precipitation is ongoing.

4.1.5 Results

Global maps of the frequency of occurrence of precipitation are shown in Fig. 4.2 for the three cloud-top height ranges defined in the figure. The data were binned into 2×2 degree boxes with approximately 5000 profiles accumulated in each box for the JJA period shown. Four specific regions are also identified for further analysis. It is noted that this analysis applies only to the oceanic regions of these boxes.

More than one cloud top height commonly exists for any given profile since tropical precipitation often falls from multiple layered cloud systems (e.g. Stephens and Wood (2007)). The cloud top height of the lowest layer (hereafter CTL) best represents the height of the precipitating cloud in a column. The cloud top height of the highest layer (hereafter CTH) is what is traditionally referred to as "cloud top height."

The cloud top height shown in Fig. 4.2 is the CTL for each column. The results indicate that (i) for the global tropicical oceans (30N-30S), the occurrence of precipitation is predominantly from low clouds with the regions of stratocumulus and trade cumulus most notable, (ii) for latitudes poleward of 30 degrees, the occurrence of precipitation is almost equally distributed between both shallow and mid-topped clouds, (iii) the frequency of occurrence of precipitation in regions associated with deep convection (the ITCZ and the western Pacific, for example) stand out both for the presence of deep precipitating clouds and the relative lack of precipitation from shallow clouds in these regions, and (iv) a non-trivial occurrence of precipitation from mid-level clouds (including the congestus mode, e.g. Johnson et al. (1999)) is evident in those regions where deep clouds tend to be most prevalent. Occurrences of this middle-level mode range from 30-60% of the total occurrences of precipitation in these regions, broadly consistent with the surface observations described in Stephens and Wood (2007).

Fig. 4.3 summarizes both the CTL (upper panel) and CTH (lower panel) properties for the regions defined in Fig. 4.2. Two summaries are presented for each region, one being the total occurrence of all clouds (left bars) and the other being

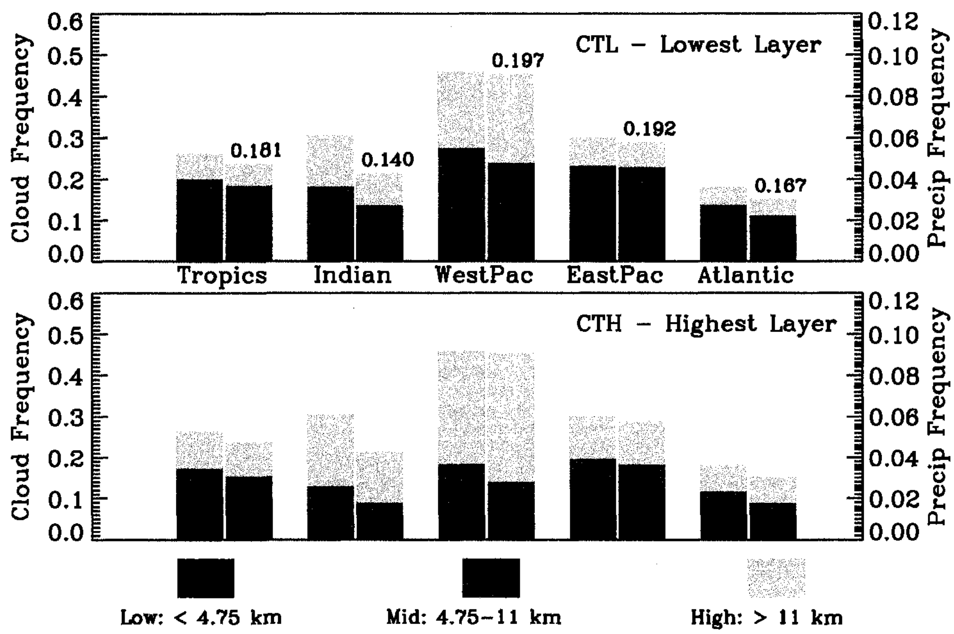

Figure 4.3: Histograms of the frequency of occurrence of cloud top heights for the three height ranges and four geographic regions defined in Fig. 4.2. Shown are the frequency of occurrence of all clouds detected by the CPR (left bars) and the matching frequencies of those clouds determined to be precipitating (right bars, note the different frequency scales). The upper panel refers to the cloud top height of the lowest layer (CTL) and the bottom panel to the highest layer (CTH). Numerals are the ratio of cloud to precipitation occurence for each region.

the occurrence of only precipitating clouds (right bars). The differences in proportions of high to mid-level to low cloud top heights between the two panels is indicative of multiple layering of clouds. For example, in the West Pacific region, clouds higher than 11.5 km are the highest cloud top in the column 27% of the time, but are the lowest cloud top only 18% of the time, indicating significant occurence of multiple cloud layers in the same column. The fractional occurrence of precipitation when cloudy is shown in numerals, being a crude indicator of the precipitation efficiency of the cloud systems observed. This ratio varies between approximately 0.14 and 0.20, being a minimum over the Indian ocean and a maximum over the western Pacific region.

Averaged profiles of cloud top heights, in terms of both CTL (left panels) and CTH (middle panels), and the distributions of PIA (right panels) are shown in Fig. 4.4. The profiles are normalized by the total incidence of all clouds (solid) and precipitating clouds (dashed). These profiles reveal that the global tropical oceans are broadly characterized by two layers of clouds, shallow clouds with maximum occurrence of cloud tops at 2 km and a second with a pronounced maximum near 12 km. A third middle mode between 5 and 8 km is also evident in all regions. The regional differences in the vertical distributions of cloud tops are striking. In the western Pacific, the middle mode is split into two sub-modes (including precipitating congestus) with tops between 5-6 km and between 7-8 km. This bifurcated middle-top mode is also evident in the Atlantic, but less so in the eastern Pacific and Indian Ocean regions. The differences between precipitating and non-precipitating clouds are also remarkable. Precipitating shallow clouds are approximately 1 km deeper than the non-precipitating shallow clouds and deep precipitating clouds are approximately 2 km deeper than non-precipitating deep

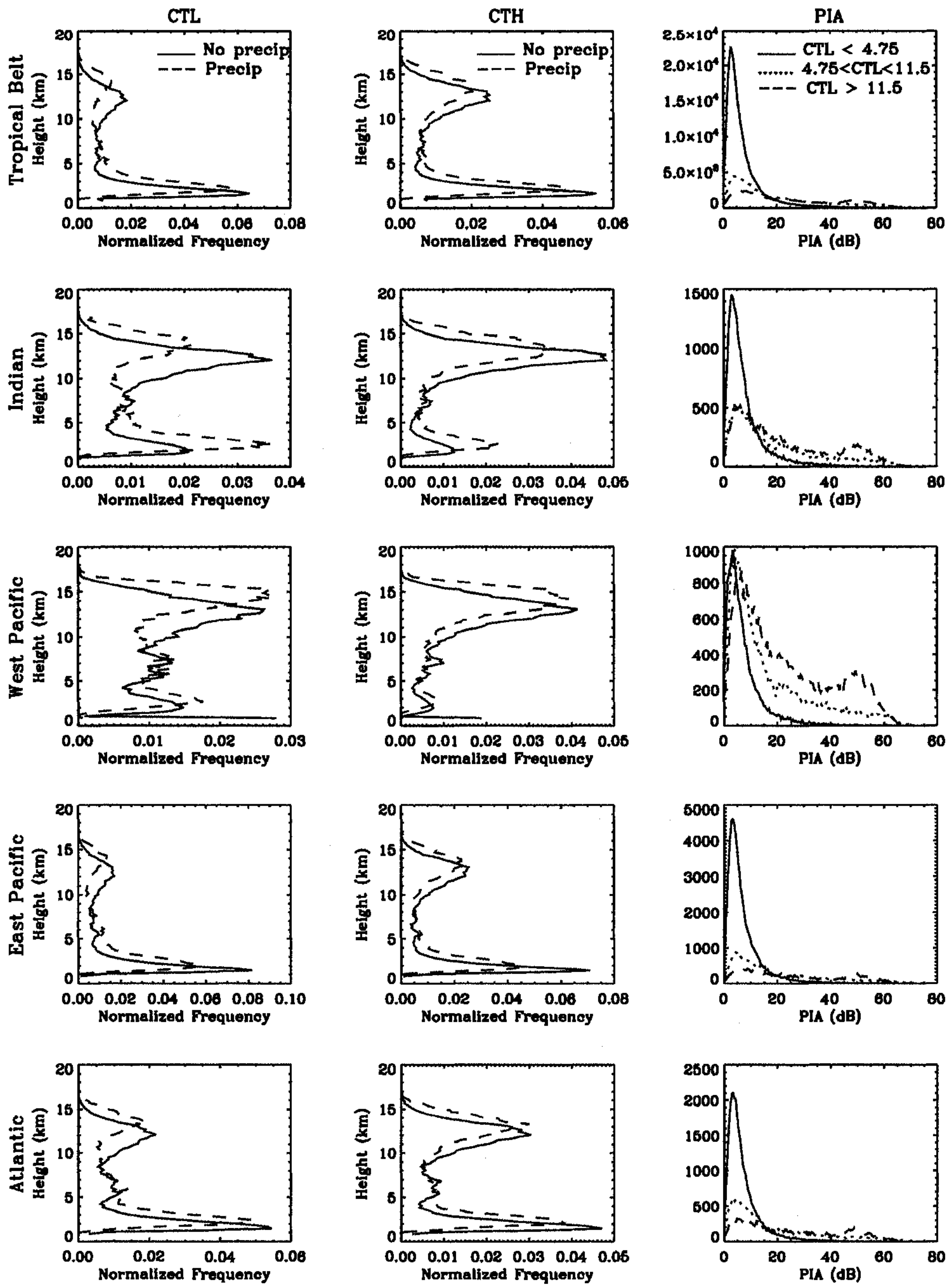

Figure 4.4: Vertical profiles of the incidence of lowest layer cloud top height (CTL, left) and highest layer cloud top height (CTH, center) for the regions indicated. The solid line applies to all clouds and the dashed to precipitating clouds. Each profile is normalized by the total occurrence of the respective cloud type. The panels shown in the right column are the distributions of PIA in 0.5 dB bins for the three CTL height categories defined in Fig. 4.2.

clouds.

The distributions of PIA also hint at a number of features about the precipitation that falls from the clouds in these regions. As noted earlier, the frequency distribution of precipitation is bimodal. The most frequent mode is characterized by low values of PIA with a peak near 5 dB, which is characteristic of light precipitation. The other mode, which peaks between 40 and 60 dB, is most pronounced in the western Pacific and Indian regions where deep convection is most prevalent.

4.1.6 Concluding Comments

CloudSat radar observations collected during JJA reveal a number of remarkable features about tropical cloudiness:
(i) The cloudiness of the global tropical oceans predominantly favors clouds with tops in two layers centered at about 2 km and 12 km. Precipitating clouds also primarily occur in two modes, a shallow mode and a deep mode, although there are hints of a third mode of cloudiness and precipitation in the tropics-wide composite. By far the highest incidence of precipitation over the global tropical oceans arises from the shallow clouds.
(ii) By contrast, regional differences in cloudiness and precipitation structures are dramatic. The vertical distribution of cloudiness over the eastern Pacific and Atlantic ocean regions, where the SSTs are lower compared to the Indian and western Pacific ocean regions, resemble the 30N-30S average structure with low cloud and related precipitation occurrences dominating. The regions over the Indian and western Pacific Oceans tend to exhibit more predominantly high clouds.
(iii) For all regions, and for the broader tropics as a whole, precipitating clouds are markedly deeper than non-precipitating clouds.

(iv) The occurrence of the middle-level mode of cloudiness and precipitation, which includes congestus, varies regionally. The lower mid-level peak in the eastern Pacific and Atlantic is consistent with the cooler SSTs and lower freezing level there. The middle-level mode is most pronounced in the Indian and western Pacific regions. In the latter it occurs at two characteristic cloud-top heights near 6 km and 8 km.

(v) Over the global tropical oceans, 18% of the clouds detected by CloudSat produce detectable precipitation. This fraction varies significantly from region to region. The western Pacific region produces precipitation more frequently for a given amount of cloudiness than any other region of the tropics whereas clouds over the Indian ocean precipitate proportionally less frequently. Factors that might influence this index of precipitation efficiency, such as moisture availability and convergence, SST and wind shear effects, and aerosol influences, amongst others, warrant further study.

Acknowledgments

This study was supported partially by the NASA research contract # NNG04GB97G. We wish to acknowledge the dedicated work of all teams responsible for the success of CloudSat. We specifically acknowledge the work of Prof G. Mace for his leadership in developing the 2B-GEOPROF product and the efforts of the CIRA team in processing the data. We also thank Cristian Mitrescu of the U.S. Naval Research Laboratory for providing the NOGAPS output.

4.2 Addendum: Inclusion of lidar cloud boundaries: Seasonal analysis

Two major developments occurred after the above article was published; first, time marched forward (as is its wont), and as a result the CloudSat mission continued, and more and more data became available. Second, the CALIPSO team publicly released their own cloud boundary data to the scientific community. The latter development is significant because there are two types of clouds that CloudSat can not observe: the lowest boundary layer clouds (those whose radar return is statistically inseparable from surface clutter), and the optically thin (for thinnest cirrus). In this section, near-global results of how often precipitation occurs over the ocean, and in particular the structure of clouds associated with precipitating systems, is examined.

The synergy of combining cloud boundaries detected by the CPR and CALIOP (the visible wavelength lidar onboard CALIPSO) is demonstrated in Figure 4.5. The figure shows the global frequency of occurrence of clouds observed by the CPR, the CPR combined with CALIOP (hereafter CPR+CALIOP), and the improvement that results from the combination. To create these distributions, a cloud is considered to be present when the CPR cloud mask indicates high likelihood of occurrence (a cloud mask value of 30 or 40), or more than 50% of a CPR range volume contains cloud according to the matched CALIOP cloud boundary information. The spatial distribution of the difference between CPR+CALIOP fractional cloud occurrence and the CPR-only fractional cloud occurrence is shown in Figure 4.6. It is apparent from these figures that there are three basic regimes where CloudSat misses a significant fraction of clouds (15% or greater). The first is the tropical upper troposphere, where thin cirrus are often present. This includes cirrus associated with the outflow from deep convection, and the more "ubiquitous" cirrus that are often present near the tropical tropopause (e.g. Jensen et al. (1996), Jensen et al. (1996)(b)). The second region is in the mid-latitudes, and is probably related to cumulus and non-drizzling stratocumulus (Sassen and Khvorostyanov, 2007). The third are clouds with tops in the lowest three CloudSat range bins (i.e. below 1 km), where cloud detection is hampered by surface contamination.

It is important to note that lidar-derived cloud boundaries are *not* used in the CloudSat precipitation detection algorithm. The ability to detect cloud by non-radar observations does not, of course, imply the ability to measure or calculate radar reflectivity in the cloud. The near-surface reflectivity is an essential input in the detection process (this will be explained more fully in Chapter 5.1.4). Unambiguous determination of hydrometeor reflectivity is not possible for the CPR below 1 km, since surface backscatter can not be separated from atmospheric backscatter. In the remainder of this section, when considering the occurrence of precipitation relative to the presence of a cloud layer, it is important to remember that there are certain lidar-detected clouds that are not tested for precipitation occurrence because they can not be observed by the radar. This uncertainty is a factor only for clouds with tops below 1 km (highlighted in Figure 4.7), since high-topped clouds missed by the radar do not precipitate at the surface unless there is measurable hydrometeor elsewhere in the column. In short, precipitation occurrence in regions with a high fraction of low-topped clouds not seen by the CPR may be subject to underestimation of precipitation incidence.

The combined CloudSat and CALIPSO statistics were aggregated seasonally into 2.5 x 2.5° bins between 60° north and south latitude. Cloud occurrence is shown in Figure 4.8. It is first noteworthy that the global oceans are cloudy more

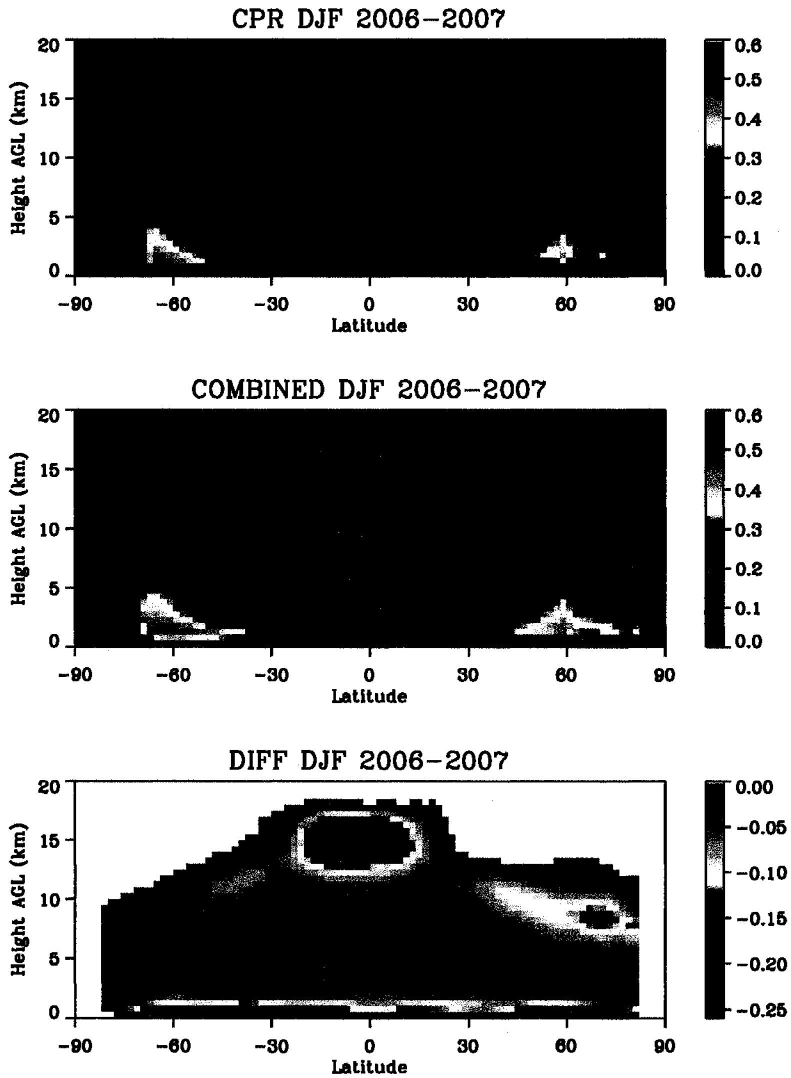

Figure 4.5: Frequency of occurrence of clouds observed by CPR (top panel), CPR+CALIOP (middle panel), and the difference (bottom panel), for DFJ 2006-2007.

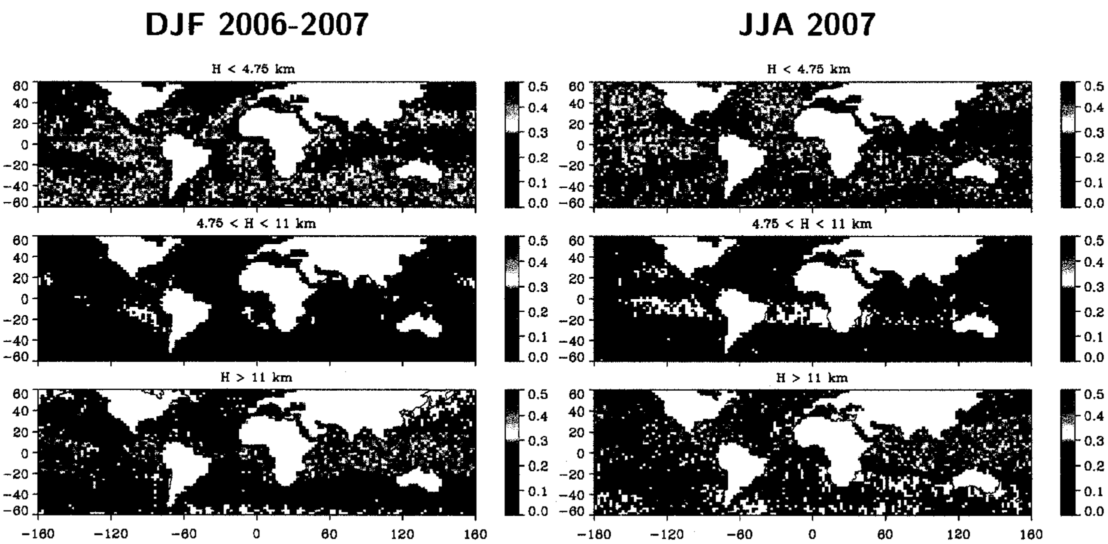

Figure 4.6: The spatial variation of the difference between the CPR+CALIOP fractional cloud occurrence and the CPR-only fractional cloud occurrence. Shown for clouds in three height bins, for both DJF 2006-2007 and JJA 2007.

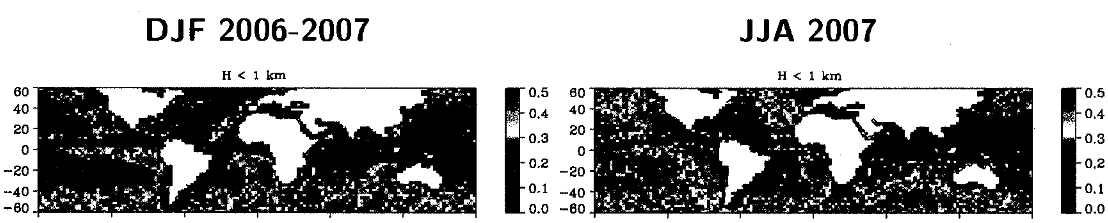

Figure 4.7: As in Figure 4.6, but for the particularly relevant clouds with tops below 1 km (see text).

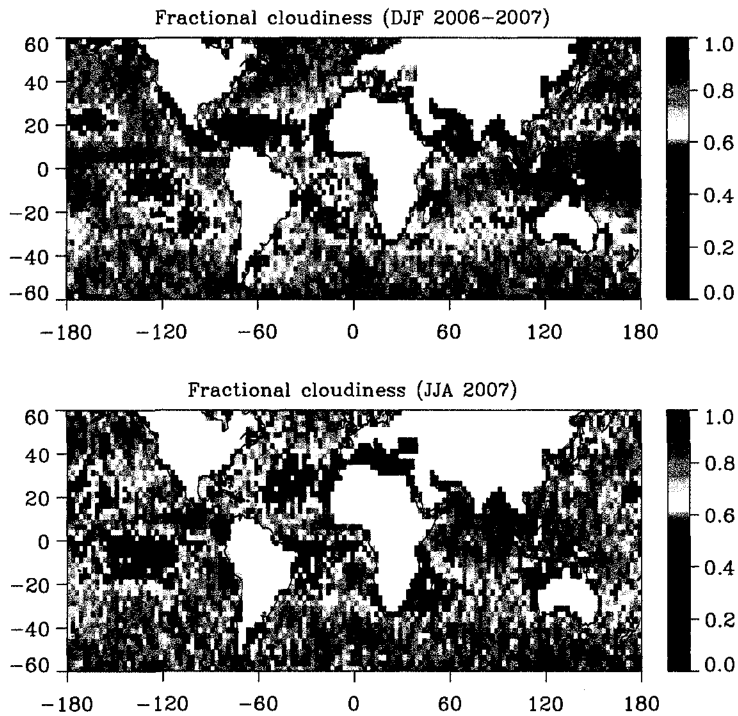

Figure 4.8: Fractional cloud occurrence from combined CPR+CALIOP for DJF 2006-2007 (top panel) and JJA 2007 (bottom panel).

often than clear; on average, greater than 70% of the global oceans contain cloud cover. Persistent clearer regions are found in the subtropics; these are the subsidence regions associated with the downward branch of the Hadley circulation. The interseasonal movement of the ITCZ is largely difficult to observe from cloud fraction alone, given the ubiquitous nature of high clouds over the oceans, but the northward shifting of the subsidence regions during JJA do provide some marker for this movement. Several regions have particularly significant seasonal oscillations in cloud cover, including the monsoon region of southern Asia, the western Atlantic/Caribbean sea, and the Mediterranean Sea.

Fractional precipitation occurrence (defined by those pixels meeting the "rain certain" category in Table 5.1) is show in Figure 4.9. The ITCZ is apparent as a region of 0.3 or greater fractional occurrence, shifting north during JJA and back south during DJF. The middle latitude storm tracks are also particularly active during the local winter months, including the Aleutian and Icelandic lows (DJF) and the southern hemisphere circumpolar vortex (JJA). Some of the rainiest parts of the planet, in fact, are outside the tropics. Precipitation occurrence in the far southern latitudes is often higher than 20%, consistent with the findings of Petty (1995) who derived precipitation incidence from ship reports; see also section 4.3. Regions marked with dark colors on this figure are not necessarily characterized by low precipitation occurrence; as previously discussed, the low-cloud detection capabilities of the CPR must also be considered. In regions where stratus are favored, particularly the west coasts of the continents (including, for example, the stratus-dominated regions of the eastern Pacific at the California coast), precipitation is sometimes not detected because drizzling clouds are too low to be observed by the CPR. Consequently, these footprints are classified as clear by the 2B-GEOPROF masking algorithm, and the precipitation algorithm classifies them as rain-free.

The frequency of occurrence of precipitation in the height categories defined in Haynes and Stephens (2007) is shown in in Figure 4.10. These height categories are defined by the cloud top height of the lowest layer (CTL). The CTL is physically relatable to the portion of cloud in a column that is actively producing precipitation, and as such is a truly new piece of geophysical information provided by the active sensors of the A-Train. The left panels are for DFJ 2006-2007, and the right panels are for JJA 2007. This figure differs from Figure 4.2 in the paper in that cloud boundaries are determined by the combined CPR+CALIOP boundary information.

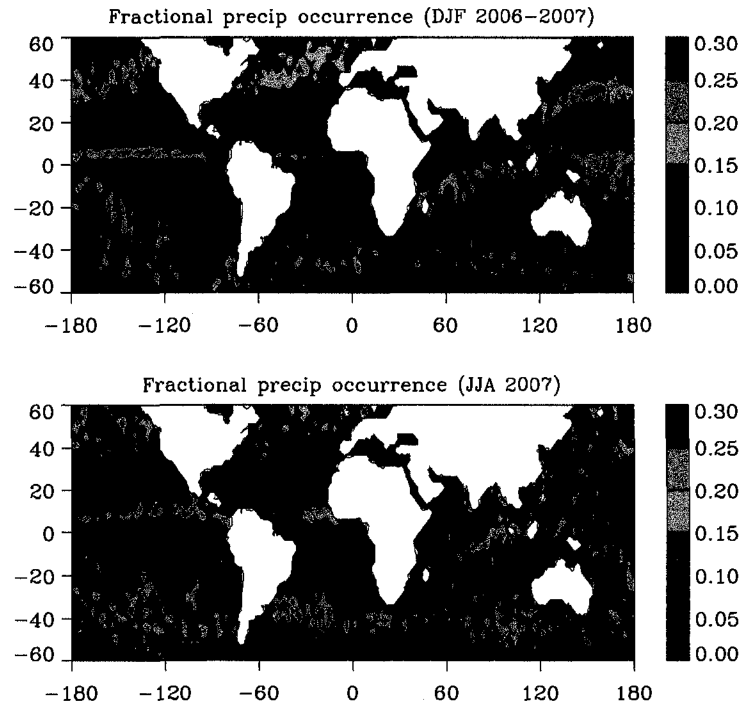

Figure 4.9: Fractional precipitation occurrence observed by CPR for DJF 2006-2007 (top panel) and JJA 2007 (bottom panel).

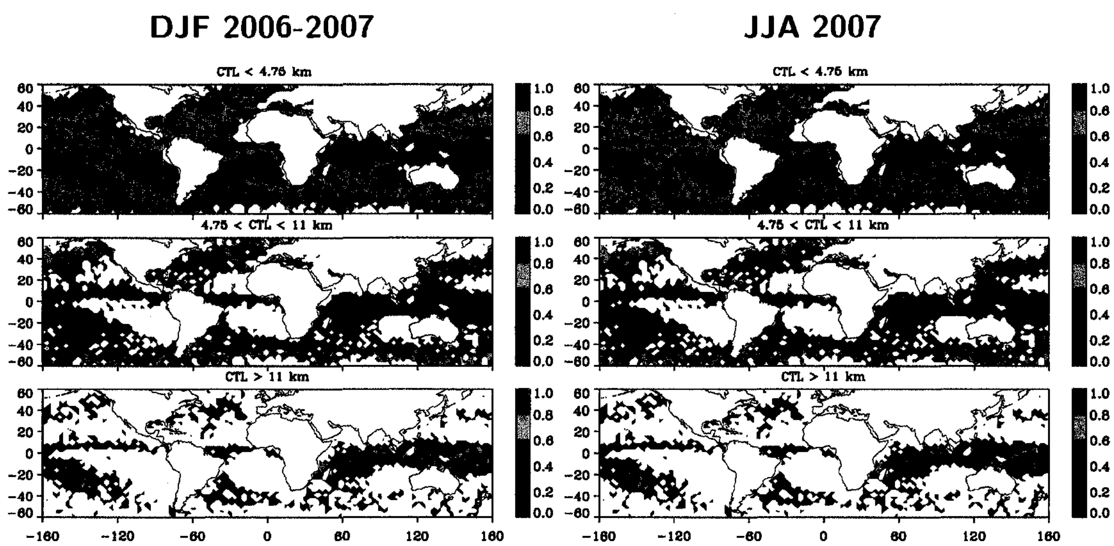

Figure 4.10: The relative frequency of precipitation occurrence grouped by the cloud top height of the lowest layer (CTL). Left panels, DJF 2006-2007; right panels, JJA 2007. For any given grid box, the sum of the three occurrences is unity.

It is first noteworthy that there are large areas of the globe where precipitation falls almost exclusively from warm, low-topped cloud systems. This is particularly true for the broad stratus regions bordering the western edges of the continents. In fact, during the southern hemisphere winter, the majority of the southern oceans between the equator and 40° south latitude are dominated by precipitation falling from systems with a CTL less than 4.75 km. Middle range CTL's, between 4.75 and 11 km, are common virtually everywhere except in the stratus regions, and dominate in some parts of the northern hemisphere storm tracks and (especially) in the southern circumpolar vortex. The highest CTL's, greater than 11 km, are associated almost exclusively with deep convection. There are very few places over the Earth's oceans, however, where the precipitation occurrence fraction due to cloud of this type exceeds 0.4; the western Pacific warm pool and monsoon region are two such locations, for example, during JJA.

An alternate view of the structure of precipitating systems is provided by examining precipitation occurrence according to CTH. Locations where precipitation occurrence by CTL differs significantly from occurrence by CTH are preferred locations of precipitation systems with multiple cloud layers. The most striking areas are those where precipitation occurrence with CTL $>$ 11 km is small, but the same occurrence with CTH $>$ 11 km is large. The western Pacific and northern Indian oceans stand out in this regard. Consider the region of the western Pacific north of New Guinea; here, approximately 20 to 40% of precipitation falls from cloud systems with a CTL of at least 11 km, but *over 85%* of precipitating systems in this region contain a cloud layer whose top is at least 11 km.

The prevalence of clouds and precipitation in the five regions defined in Haynes and Stephens (2007), now determined using the CPR+CALIOP cloud identifica-

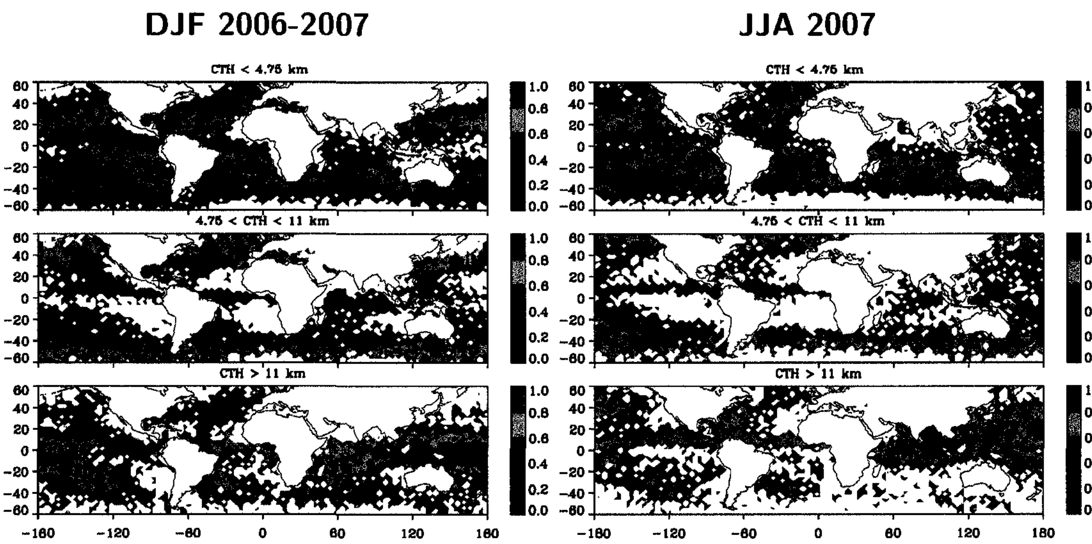

Figure 4.11: As in Figure 4.10, but for cloud top height of the highest layer (CTH).

tion scheme, is shown in Figure 4.12. The inclusion of CALIOP-detected clouds, particularly thin cirrus near the tropical tropopause and boundary layer clouds, significantly increases the observed cloud fraction, and therefore decreases the fraction of cloud systems determined to be precipitating (as described in the paper, this ratio is a crude indicator of precipitation efficiency). The amount of high cloud (CTH > 11) km increases substantially with this change, such that in the western Pacific region approximately 70% of cloudy scenes (alternately 60% of all scenes) observed by the combined CPR and CALIOP sensors contain cloud above 11 km. The fraction of clouds that produce precipitation remains highest in the western Pacific region (11-12% depending on season). The lowest fraction of precipitating clouds is in the Atlantic region, rather than the Indian region. However, it is noted the fraction of clouds detected by CPR+CALIOP but but not CPR alone is considerably higher in the Atlantic region, such that precipitation efficiency may be underestimated here. The tropical-ocean estimate of the fraction of cloudy scenes that produce precipitation is reduced to approximately 10% (from the 18% quoted

DJF 2006-2007

	Tropics	Indian	WestPac	EastPac	Atlantic
Low	0.032	0.013	0.033	0.045	0.021
Middle	0.019	0.021	0.028	0.019	0.011
High	0.018	0.025	0.039	0.010	0.007
Total	0.069	0.059	0.100	0.074	0.039

JJA 2007

	Tropics	Indian	WestPac	EastPac	Atlantic
Low	0.037	0.022	0.018	0.042	0.026
Middle	0.017	0.025	0.030	0.013	0.014
High	0.016	0.036	0.043	0.011	0.014
Total	0.070	0.083	0.091	0.066	0.054

Table 4.1: Precipitation occurrence by CTL for the four geographic regions and cloud height modes defined in Figure 4.2.

in Haynes and Stephens (2007)).

The precipitation occurrence categorized by CTL for each region is reproduced numerically in Table 4.1. The western Pacific basin is the rainiest during both seasons, and the Atlantic the driest. It it remarkable that in the western Pacific, there is comparable precipitation incidence from each of low, middle, and high topped clouds during the winter season. During the summer, precipitation falls from middle top clouds only slightly less than from high topped clouds. Over the tropical oceans as a whole, precipitation falls about twice as often from clouds with CTL's less than 4.75 km than any other type of cloud. The mean vertical structure of both precipitating and non-precipitating cloud systems is further examined in Figure 4.13 and 4.14. The result that the global oceans exhibit two dominant modes of cloud cover associated with precipitation remains unchanged, but the heights of these clouds are amended to 2 and 15 km. Also unchanged is the

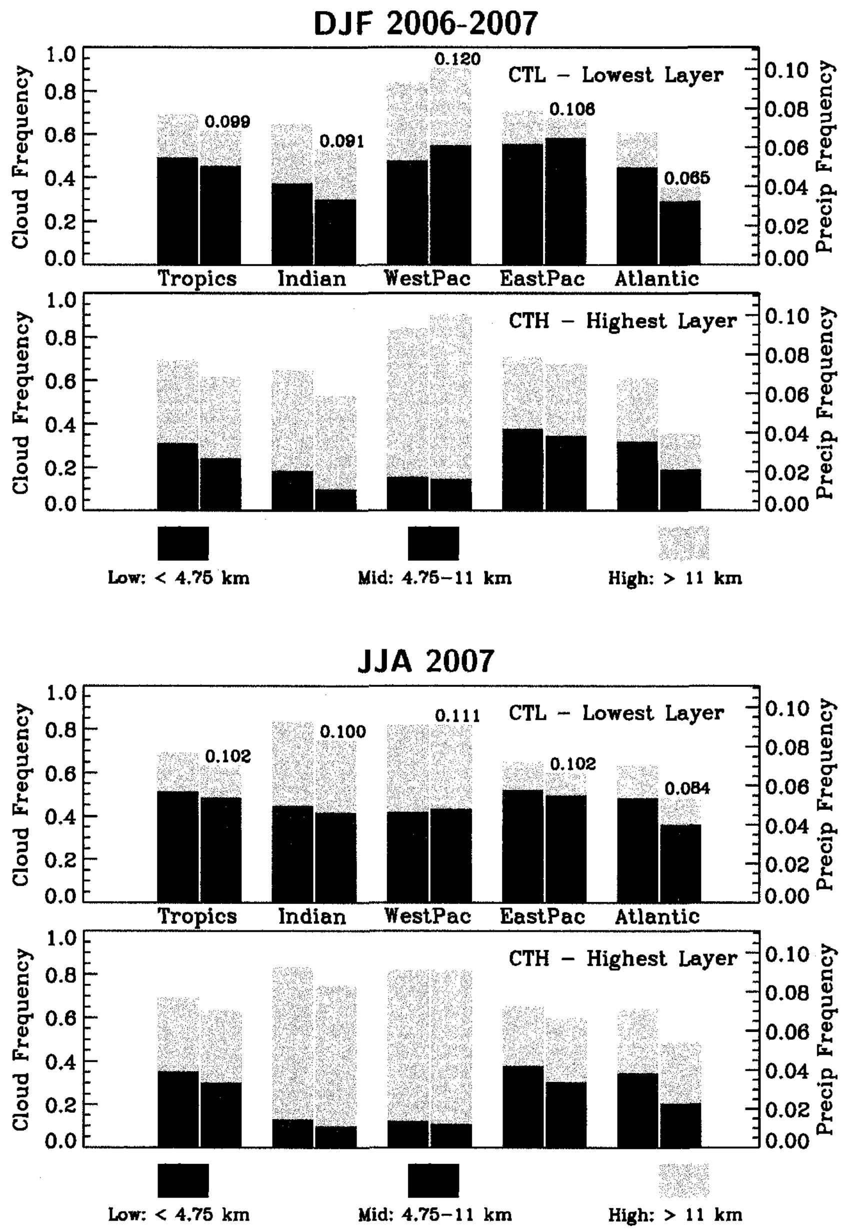

Figure 4.12: Histograms of the frequency of occurrence of cloud top heights for the three height ranges and four geographic regions defined in Figure4.2. Shown are the frequency of occurrence of all clouds detected by the CPR+CALIOP (left bars) and the matching frequencies of those clouds determined to be precipitating (right bars, note the different frequency scales). For each season, the upper panel refers to the cloud top height of the lowest layer (CTL) and the bottom panel to the highest layer (CTH). Numerals are the ratio of cloud to precipitation occurrence for each region.

finding that a third mode of cloud cover associated with precipitation exists in certain areas, namely the western Pacific and Indian ocean basins, but also the Atlantic ocean basin to a lesser extent.

The vertical structure of precipitating clouds is further elucidated in Figures 4.15 and 4.16. In the tropics, precipitation incidence is mainly from either clouds with low to middle CTL's, or high CTL's (deep convection). In the subtropical stratus regions and moving toward the middle latitudes, low cloud dominates rain incidence. In the higher latitudes, there is a continuum of CTL's that contribute to rain incidence. Stratifying by CTH, however, results in a different picture; in this case, the lower cloud influence is greatly reduced everywhere except the stratus regions of the winter hemisphere. This indicates, again, that multiple layer clouds are ubiquitous, not only in the tropics, but into the middle and high latitudes as well. The rain structure between 40 and 60° latitude of both hemispheres is remarkable; while CTL's are distributed nearly evenly between 1 km and the ~10 km tropopause, CTH's are concentrated mainly near the tropopause, particularly in the winter hemisphere. This may be partially related to the phenomenon of jet stream cirrus; Menzel et al. (1992) found that during 1986-1988, an average 25-30% of the continental United States was covered by cirrus related to the jet stream at any given time.

Precipitation occurrence results from CloudSat over the near-global oceans are summarized as zonal means in Figure 4.17. Cloud cover over the oceans is found to be extensive, the area-weighted mean being 72% between 60° N and 60° S latitude. Over the tropical oceans, cloudy scenes containing multiple layers are more common than single layer scenes, and the majority of precipitation occurrence is not from continuous, deep convective columns, but from broken cloud columns

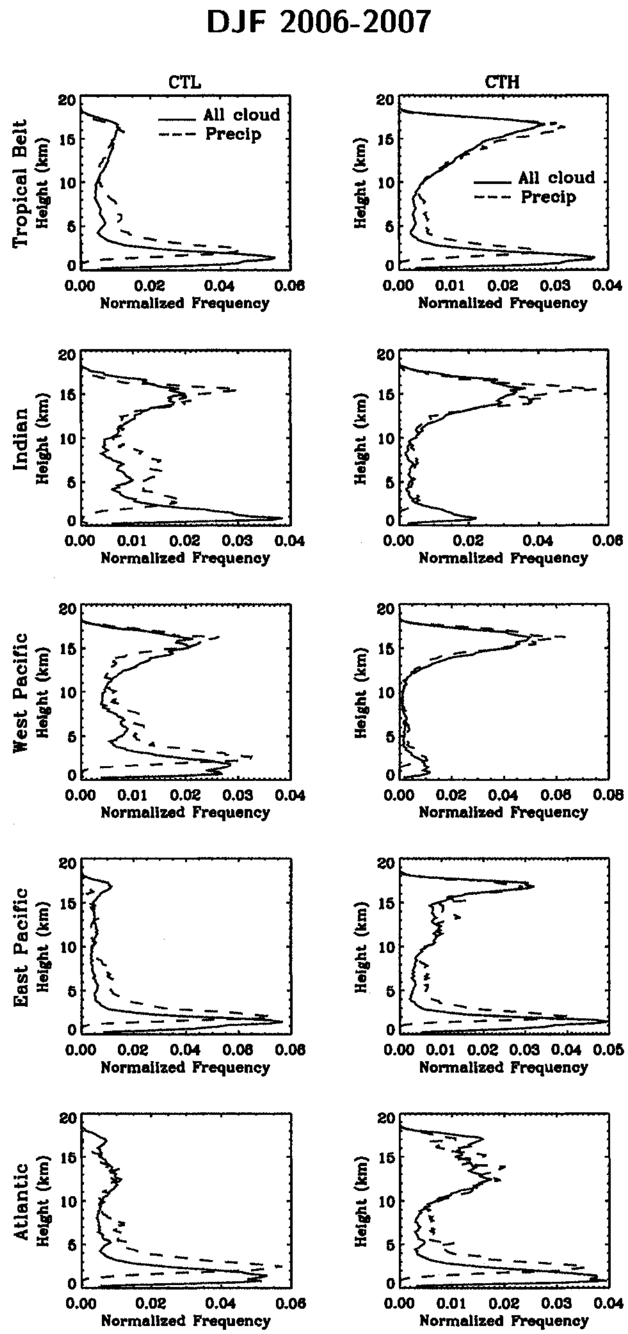

Figure 4.13: Vertical profiles of the incidence of lowest layer cloud top height (CTL, left) and highest layer cloud top height (CTH, center) for the regions indicated. The solid line applies to all clouds and the dashed to precipitating clouds. Each profile is normalized by the total occurrence of the respective cloud type. For DJF 2006-2007.

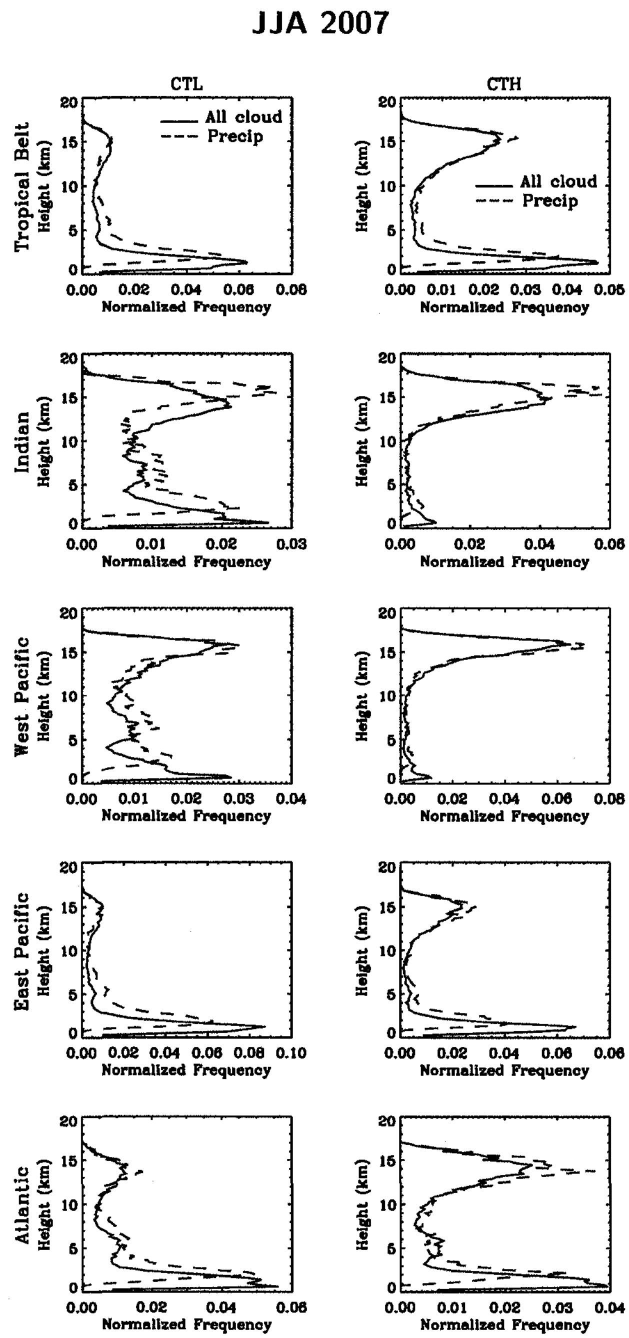

Figure 4.14: As in Figure 4.13, but for JJA 2007.

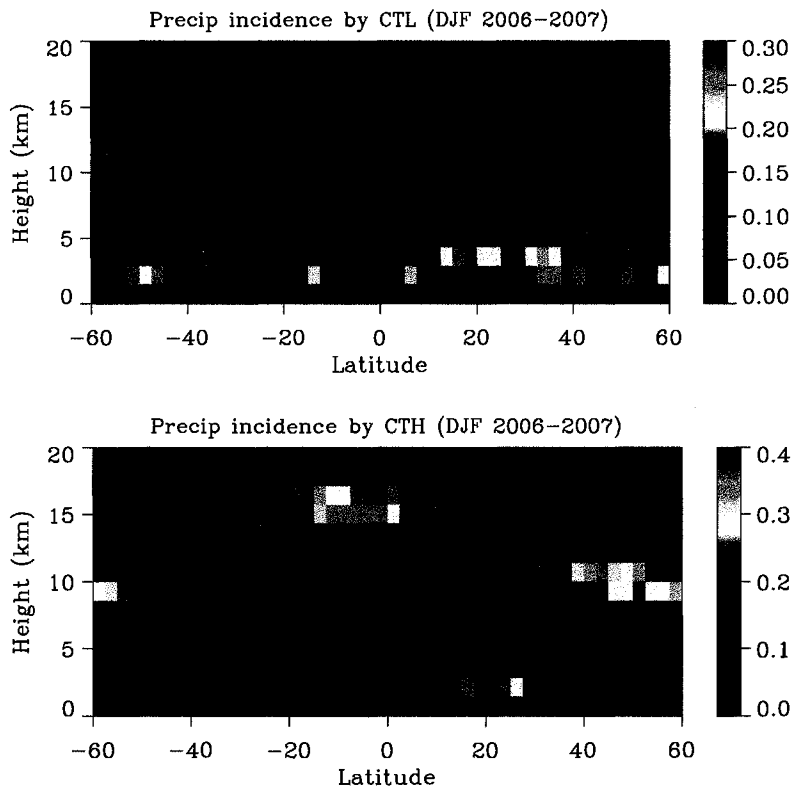

Figure 4.15: Zonal distribution of CPR precipitation incidence as a function of CTL (top panel) and CTH (bottom panel). For DJF 2006-2007.

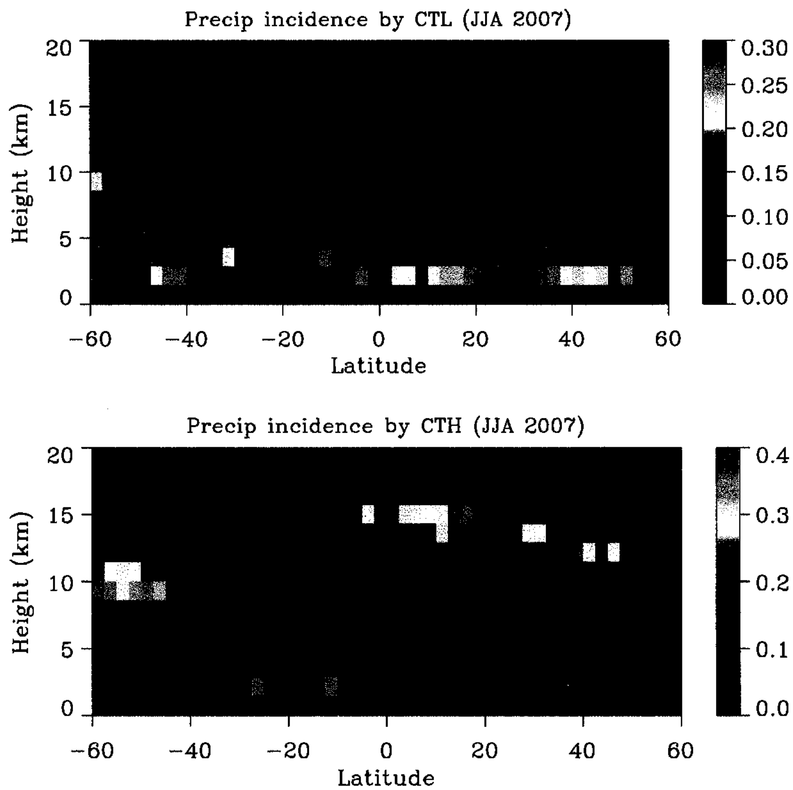

Figure 4.16: As in Figure 4.15, but for JJA 2007.

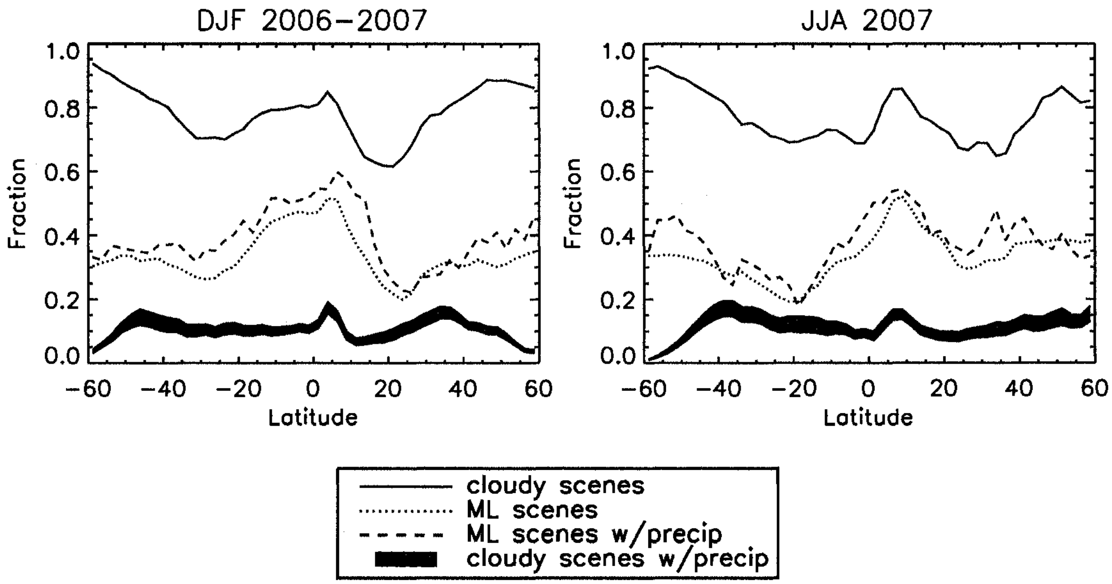

Figure 4.17: Zonal mean fraction of: cloud scenes observed by CPR+CALIOP (solid line), multi-layer scenes (dotted line), multi-layer scenes with precipitation detected (dashed line), cloudy scenes with precipitation detected (shaded region). Shading represents the difference between the "rain certain" and "rain probable" precipitation categories.

(often low or middle level clouds with overlying cirrus). The average tropical ocean-wide fraction of cloudy scenes with precipitation present is found to be approximately 0.10, with the highest average efficiency found in the ITCZ.

4.3 Addendum: Precipitation incidence validation

Oceanic precipitation incidences from derived from the passive microwave outside the tropics are considerably lower that those obtained from the CPR. Petty (1995) found that shipborne surface observations of precipitation over the higher latitude oceans are significantly higher than indicated by passive microwave estimates. To test the CPR precipitation occurrence fractions, the COADS ship reports were obtained for the 2006-2007 time period and processed as described in Chapter 2.5.

Figure 4.18 shows the rain and snow precipitation incidence when cloud is detected *by CloudSat* (note that CloudSat detects cloud less often then does CPR+CALIOP). COADS observations are given by the gray shaded bars (the width of the bars indicating uncertainties in interpretation of the present weather codes), the CPR "rain certain" observations as orange dots, the CPR "rain or snow certain" observations as green dots, and AMSR-E observations (conditional on CloudSat-observed cloud) as purple dots. It is evident from the figure that the CPR captures most of the latitudinal variations in precipitation that are present in the surface observations. Furthermore, while AMSR-E precipitation incidence falls toward zero at high latitudes (since frozen precipitation is problematic), the CPR and COADS observations indicate that the higher latitudes are amongst the wettest places on the planet. Inconsistencies between CloudSat and the COADS observations at the highest latitudes may be related to the lack of ship reports that contribute to the COADS dataset above 60° latitude. These findings support those of Petty (1995) and give confidence in the CPR rainfall detection capabilities.

Results when the cloud presence requirement is removed are show in Figure 4.19 (see also Figure 5.13). In the tropics, CPR and AMSR-E show very similar patterns of total precipitation incidence, and for liquid precipitation this extends even into higher latitudes. The CPR incidence values tend toward the lower (i.e. most conservative) of the COADS incidences. The reason for this is unknown but may be related to human psychology; when no significant weather is occurring, ship reports are sometimes neglected by observing personnel (this is probably especially likely when the sky is clear and a report is deemed completely unnecessary). This effect more than likely inflates precipitation incidence in the COADS reports.

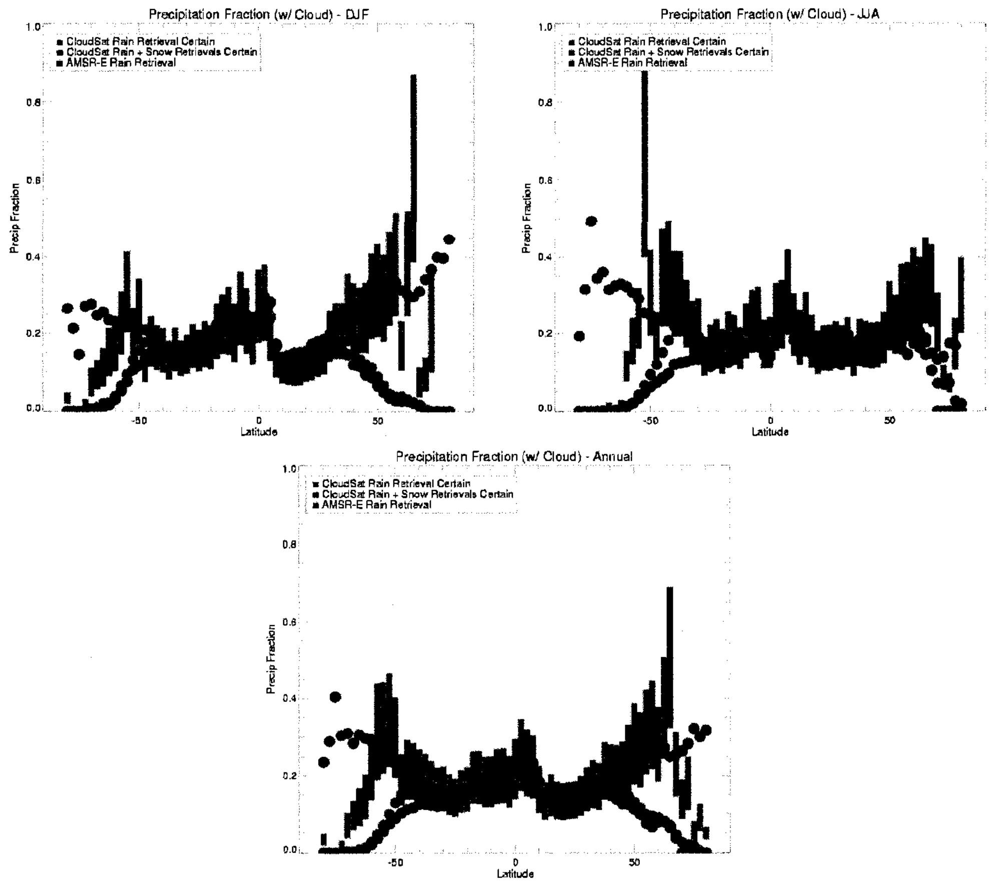

Figure 4.18: COADS seasonal shipborne observations of precipitation occurrence when cloud is detected by CloudSat (gray bars). Overlayed are CPR "rain certain" occurrences (orange dots), "rain or snow certain" occurrences (green dots), and AMSR-E rain occurrences (purple dots). The spread in the gray bars represents uncertainties in interpretations of the COADS present weather observations codes. Figure courtesy of Todd Ellis, Colorado State University.

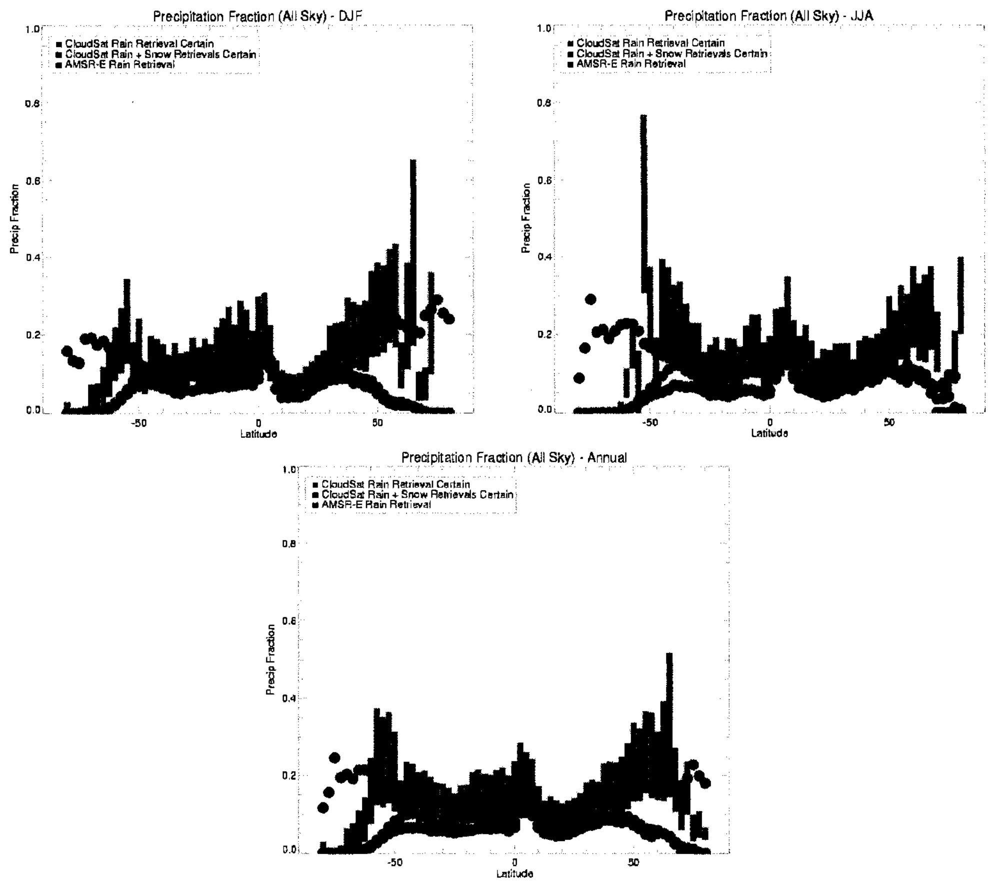

Figure 4.19: As in Figure 4.18, but without the conditional cloud presence requirement. Figure courtesy of Todd Ellis, Colorado State University.

5 Precipitation Detection and Quantification with CloudSat

Details of the CloudSat column precipitation algorithm are described in this chapter. The bulk of the chapter is comprised of a journal article describing the algorithm, which contains some example applications, comparisons with other sensors, and chief results. The article is followed by several addendums that expand upon information that was omitted because of space constraints, including details of the discrete dipole approximation and Monte Carlo calculations, and a more in depth look at the uncertainties associated with the retrieval. Additional results from application of the algorithm will be discussed in the next chapter.

5.1 Rainfall retrieval over the ocean with spaceborne W-band radar

Text in section 5.1 is work submitted for publication by the author (Haynes et al., 2008). Figure numbers, equation numbers, and citation styles have been changed for integration into the dissertation.

5.1.1 Abstract

A method for retrieving precipitation over the ocean using spaceborne W-band (94 GHZ) radar is introduced and applied to the CloudSat Cloud Profiling Radar. Measurements of radar backscatter from the ocean surface are combined with

information about surface wind speed and sea surface temperature to derive the path integrated attenuation through precipitating cloud systems. The scattering and extinction characteristics of rain drops are modeled using a combination of Mie theory (for rain drops) and the discrete dipole approximation (for ice crystals and melting snow), and a model of the melting layer is implemented to represent the transition between ice and liquid water. Backward Monte Carlo modeling is used to model multiple scattering from precipitating hydrometeors between the radar and ocean surface, which is shown to be significant for precipitation rates exceeding 3-5 mm h^{-1}, particularly when precipitating ice is present. An uncertainty analysis is presented and the algorithm is applied to near-global CloudSat observations and compared with other near-global precipitation sources. It is found that in the tropics, total seasonal water accumulation derived from CloudSat generally agrees well with other precipitation sensors. In the middle latitude storm tracks, however, CloudSat observes precipitation more often and with greater resulting accumulation than other spaceborne sensors.

5.1.2 Introduction

Precipitation is a key process contributing to the exchange of energy between the Earth's surface and its atmosphere. This energy exchange is an important component of the global water cycle which determines, for example, the availability of water for human use and consumption. Satellite measurements of rainfall have led to great advances in our understanding of how often rain falls and where it falls on the Earth's surface. CloudSat, part of the afternoon A-train constellation of satellites (Stephens et al., 2002), contains the first meteorological high frequency radar to observe the Earth's atmosphere from space, providing an opportunity to advance our understand of not only the vertical structure of cloud systems, but the distribution of the rain they produce as well. It is similarly the first metorological active, spaceborne observing system to regularly see precipitation on the planet outside of the tropics.

CloudSat carries the 94 GHz Cloud Profiling Radar (CPR). The CPR is a W-band, nadir-pointing radar system designed for the vertical profiling of hydrometeors in the atmosphere. The performance of the radar since launch is detailed in Tanelli et al. (2008). Although usually optimized for the observations of clouds, high frequency radars such as the CPR are also highly sensitive to the presence of both solid and liquid precipitation. The effects of attenuation on the radar signal may be significant; the basis of most liquid precipitation retrievals with such radars is related to the principle that attenuation may be utilized as a source of information, rather than a source of geophysical noise.

Several previous studies have examined the feasibility of precipitation retrieval using millimeter wavelength radars. L'Ecuyer and Stephens (2002) determined that there was sufficient information in the path integrated attenuation (PIA) and reflectivity to retrieve profiles of light to moderate rainfall in the tropics. Matrosov (2007) demonstrated that under the assumption of a uniform raining layer, the vertical gradient of reflectivity at any height is related to the magnitude of the attenuation at that height, which can then be related back to rain rate.

The basic principle underlying these retrievals is that under single-scatter conditions and assuming perfect knowledge of the drop size distribution in a raining medium, it is possible to use Mie theory to predict the attenuation that would be observed at any number of differing precipitation rates. By matching the observed attenuation to the set of predicted values, one can then obtain an estimate of the intensity of the precipitation that produced the attenuation. There are several complications to such methods. The first involves separation of the effects of precipitation intensity from those of attenuation; both can lead to variations in the primary measured quantity, radar reflectivity. Knowledge of PIA partially mitigates this uncertainty. Next are the effects of multiple phases of precipitation, due to the presence of both melting particles and ice phase precipitation. A third complication is multiple scattering of radiation by raindrops and snowflakes between the target and the antenna, which means that observed scattering may be greater than the component due to backscattering alone.

The methodology described here attempts to account for each of these complications while still utilizing the basic physical relationship between radar beam attenuation and precipitation rate. In section 5.1.3, a method for deriving PIA that is based on the relationship of ocean surface backscattering cross section to wind speed and sea surface temperature is described. Section 5.1.4 outlines the basis of the algorithm, section 5.1.5 details a model of the radar return through the melting level, and section 5.1.6 describes the calculation of multiple scattering effects utilizing a backward Monte Carlo model of the radiative transfer equation. Section 5.1.7 presents an uncertainty analysis of the algorithm and section 5.1.8 describes retrieval results from CloudSat over the near-global oceans, as well as comparison with other precipitation data sets. The last section summarizes the methodology and principle results.

5.1.3 Estimation of PIA over ocean

Attuenation by hydrometeors can be significant at W-band. Consider a column of depth H containing clouds and precipitation. Neglecting melting effects and multiple scattering for the time being, the PIA (given here in dB) is defined as the two-way, integrated extinction due to these hydrometeors,

$$PIA = 2\,\psi \int_0^H k_{ext}(s)\,\mathrm{d}s\,, \tag{51}$$

where k_{ext} is the height-dependent extinction coefficient due to clouds and precipitation and $\psi = 10/\ln 10$. Here s is defined perpendicular to the surface and increasing with height such that the integration is carried out over all range gates between the surface and H. From the persepective of a W-band spaceborne radar, the surface of the Earth scatters orders of magnitude more radiation than any atmospheric target, and as such is easily detectable unless masked by intervening hydrometeor attenuation. This reduction in surface backscatter provides a means to estimate attenuation. The PIA in a raining column can be estimated through observations of the normalized backscattering cross section of the surface, σ_0, relative to the clear sky value of this quantity, σ_{clr}:

$$PIA = \sigma_{clr} - \left(\sigma_0 + 2\,\psi \int_0^\infty k_{gas}(s)\,\mathrm{d}s\right)\,, \tag{52}$$

where k_{gas} is the extinction coefficient due to atmospheric gases. Gaseous attenuation can be significant for millimeter wavelength radar, especially in the relatively moist tropics where it typically exceeds 6 dB (two-way), and its contribution to σ_0 must be removed. With knowledge of the atmospheric temperature and moisture structure at the point of measurement, taken here from the ECMWF auxiliary data matched to the observations (Stephens et al., 2008), this contribution can be calculated with high accuracy (Liebe, 1985).

The ability to determine PIA therefore depends on knowledge of σ_{clr}. Figure

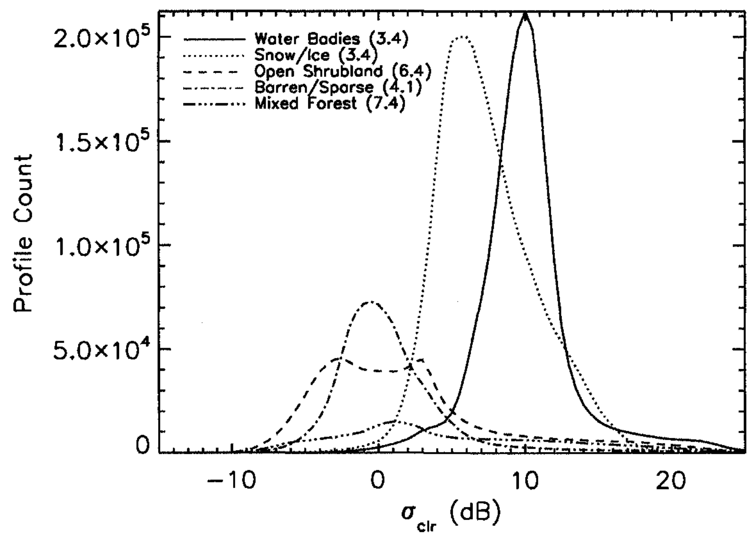

Figure 5.1: Histograms of σ_{clr} for the five most common surface types observed by the CPR during SON 2006, classified according to the IGBP land surface type database. Standard deviation in dB shown in parenthesis. Water bodies scaled by 1/7.

5.1 shows histograms of clear-sky surface backscatter for the five most common surface types observed by the CPR during September-November (SON) 2006, classified according to the International Geosphere-Biosphere Programme (IGBP) land surface type database (at 10 km resolution). While certain surface types show low variability, particularly water bodies, snow/ice surfaces, and barren/sparse vegetation, most land surfaces exhibit considerably higher variability of σ_{clr}. This is because backscatter from land surfaces depends on vegetation, surface slope, soil moisture, presence and evaporation rate of recent rainfall, age and depth of snow cover, and other factors. It is noted that the CPR may classify some scenes as clear when clouds are present below approximately 1 km due to surface clutter effects (Tanelli et al., 2008), but the contribution of these clouds to PIA is generally small.

An analysis of σ_{clr} from October 2006 (Figure 5.2) demonstrates the spatial variability of this parameter. As expected, the variance is largest over land surfaces, excluding certain arid regions, particularly the Sahara and deserts of western Australia. The edge of the Antarctic ice sheet is visible as a region of high backscatter near 60° south latitude, and the heterogeneous/shifting nature of the sheet is represented by the region of high variability south of the edge. For water surfaces, the standard deviation of σ_{clr} is approximately 3.4 dB, but the latitudinal banding suggests a dependence on other physical processes. It will be demonstrated that knowledge of these physical processes allows the variance of σ_{clr} to be reduced, resulting in the ability to estimate PIA within approximately 2 dB. Over land, however, the physical processes controlling σ_{clr} are not easily resolved, and a PIA-based land-surface precipitation retrieval is therefore beyond the scope of this study.

The normalized backscatter of the surface of the ocean, σ_{clr}, can be calculated as a function of viewing angle given measurements of surface wind speed, V, and sea surface temperature, SST [e.g. Li et al. (2005); Freilich and Vanhoff (2003)]. The wind speed dependence arises from roughening of the ocean surface by wind-generated waves, which scatter radiation out of the field of view of the receiving antenna. The SST dependence, which is considerably smaller than that due to wind, is related to the variation of the Fresnel coefficient for sea water with temperature. In this study, the relationship between V, SST, and σ_{clr} was established using wind speed measurements derived from the microwave radiances observed by AMSR-E and SST from the ECMWF forecast model. Aqua, the satellite platform containing AMSR-E, flies approximately 1 minute ahead of CloudSat in the A-Train formation, providing nearly simultaneous views of the same scene (albeit

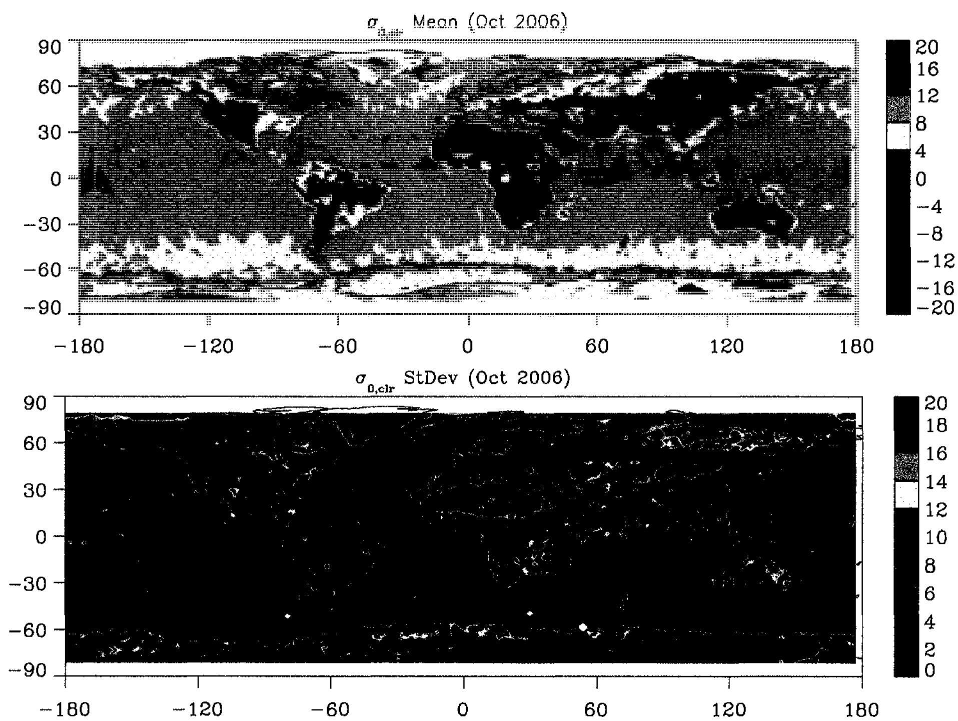

Figure 5.2: Mean (top panel) and standard deviation (bottom panel) of clear-sky ocean surface normalized backscattering cross section for October 2006.

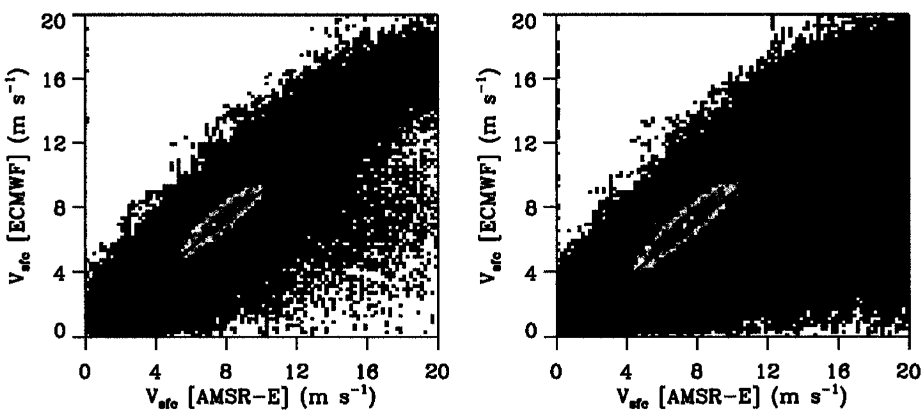

Figure 5.3: Wind speed derived from AMSR-E microwave estimate versus that of the ECMWF operational forecast model for clear-sky conditions (left) and all-sky conditions (right). The mean and standard deviations are shown in solid and dashed lines, respectively.

with a larger field of view).

AMSR-E derived wind speeds, although useful in clear skies, are contaminated by rainfall and cannot be used in the presence of precipitation. For this reason, ECMWF wind data were also matched to the CloudSat track for comparison purposes. A scatter plot of these two wind speed estimates for a number of points along the CloudSat track is shown in Figure 5.3. The scatter is small for clear-sky conditions, but increases in all-sky conditions because AMSR-E radiances are contaminated by rainfall or high values of cloud water path. Given these results, the operational ECMWF winds are used in the retrieval when the presence of precipitation is unknown.

Several months of observations of σ_{clr}, utilizing AMSR-E derived winds and corrected for gaseous attenuation, were gathered for each CloudSat pointing angle epoch (CloudSat currently points 0.16° off nadir, and only results from this epoch are discussed here) and a range of SST's. The resulting relationships between σ_{clr} and V have an uncertainty of approximately 2 dB and largely agree with the

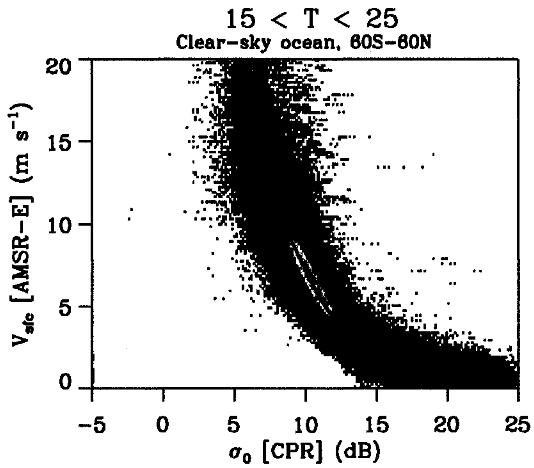

Figure 5.4: The relationship between observed ocean surface backscatter and AMSR-E derived wind speed. The red line represents the mean, the black dashed lines one standard deviation from the mean.

parameterization described by Li et al. (2005). Backscatter off the ocean surface is largest for small wind speeds, when the ocean backscatter becomes quasi-specular, as shown in Figure 5.4. As the wind speed increases, roughening of the surface results in scattering of power outside the field of view of the radar receiver, and σ_{clr} decreases accordingly. The wind speed dependence is clearly visible in Figure 5.2; ocean values of σ_{clr} are smallest between 40 and 60° S latitude, where the circumpolar vortex produces strong surface winds resulting in a roughened sea surface. The tropical and subtropical oceans, by contrast, have generally calm seas with relatively high values of σ_{clr}.

5.1.4 Rainfall algorithm in its simplest form

Neglecting melting effects and multiple scattering (which are accounted for in sections 5.1.5 and 5.1.6), the basis of a PIA-based precipitation retrieval lies in the implied relationship between the observed surface backscatter, σ_0, and the integrated extinction coefficient, k_{ext}. Assuming a constant rain profile between the surface and a height H above the surface, (51) and (52) may be combined to obtain

$$\sigma_0 = \sigma_{clr} - 2\,\psi \left[\int_0^\infty k_{gas}(s)\,\mathrm{d}s + k_{ext} H \right] . \tag{53}$$

In an idealized case, H may be considered the lesser of the height of the melting layer and cloud top height, as determined from the reflectivity signature. For CloudSat, the cloud top height is determined from the 2B-GEOPROF cloud mask.

k_{ext} can in turn be related to precipitation rate, R, given knowledge of the drop size distribution (DSD) of the rain drops. Without *a priori* knowledge of the DSD for the myriad of scenes that the radar may observe, for simplicity we assume a rain drop size distribution given by the classic Marshall and Palmer (1948) exponential relation:

$$N(D) = N_0\,\exp(-\lambda\,D) \tag{54}$$

$$\lambda = A_\lambda\,R^{B_\lambda} \tag{55}$$

where N is the particle number concentration, $N_0 = 8 \times 10^6$ m^{-4} is the distribution intercept parameter, λ is the slope parameter, $A_\lambda = 4100$ m^{-1} (mm h^{-1})$^{0.21}$, and $B_\lambda = -0.21$. Furthermore, a log-normal distribution of cloud water is assumed (Austin and Stephens, 2001) with the ratio of cloud water to rain water content specified as a function of rain rate using averaged values from the Goddard Profiling Algorithm (GPROF) cloud resolving model database, as shown in Figure 5.5. GPROF, it is noted, forms the basis of the TRMM and AMSR-E surface precipitation products (Kummerow et al., 2001).

For spherical particles,

$$k_{ext} = \frac{\pi}{4} \int_0^\infty Q_{ext}(D)\,\left[N(D) + N_c(D) \right] D^2\,\mathrm{d}D\,, \tag{56}$$

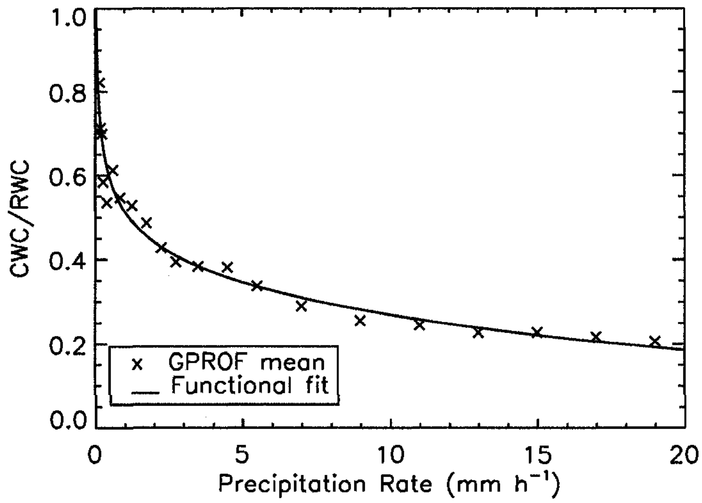

Figure 5.5: Mean value of the ratio of cloud water content (CWC) to rain water content (RWC) as extracted from the GPROF database.

where Q_{ext} is the extinction efficiency obtained from Mie theory for a large range of particle sizes (Bohren and Huffman, 1983) and N_c is the total concentration of cloud drops [see Austin and Stephens (2001)]. This relationship is shown at a variety of common radar frequencies in Figure 5.6. The viability of this approach for cloud radars (such as the W-band CPR) is immediately apparent; higher frequency radars experience more attenuation for a given rain intensity than lower frequency radars. Furthermore, the sensitivity of attenuation to rainfall is greatest for small R, indicating that PIA based rainfall retrievals work best for light rainfall. It is noteworthy that this approach is not applicable to radars with frequencies lower than Ku band (about 12-18 GHz) as the influence of rain on the surface signal will be smaller than the uncertainty in the measurement of σ_0.

The combination of equations (53) through (56) provides the relationship be-

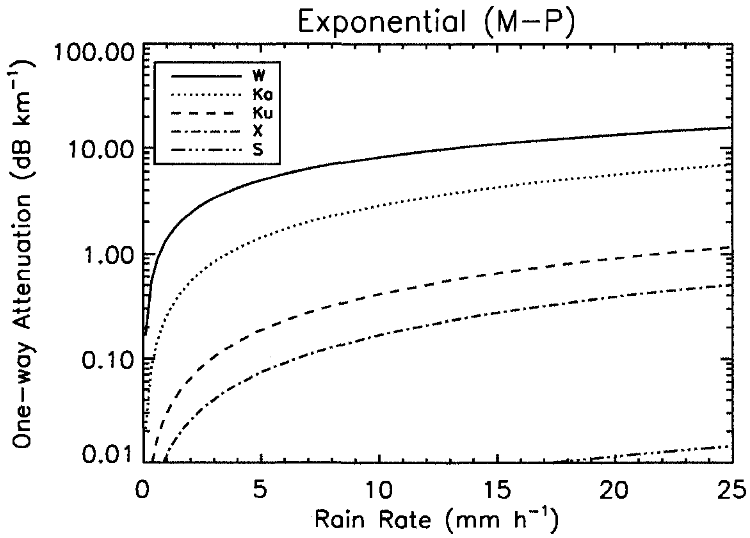

Figure 5.6: Attenuation coefficients for a Marshall-Palmer type distribution of rainfall at a variety of common radar bands as indicated by their IEEE identification. The CloudSat CPR is a W-band radar.

tween σ_0 and R, whose solution is given by

$$\begin{aligned}\sigma_0 &= \sigma_{clr}(V, SST) \\ &- 2\,\psi \left[\int_0^\infty k_{gas}(s)\,\mathrm{d}s + \frac{\pi H}{4} \int_0^\infty Q_{ext}(D)\,[N_0 \exp(-A_\lambda\, R^{B_\lambda} D) + N_c(D)] D^2\,\mathrm{d}D \right] .\end{aligned} \tag{57}$$

Thus (57) indicates that given knowledge of the ocean surface wind speed, SST, depth of the raining column, column temperature and humidity (to derive the gaseous attenuation), and an observation of σ_0, one can derive the rain rate R for that profile. This formulation neglects multiple scattering and ice phase precipitation within the radar beam, and as such is only useful in those cases with purely liquid precipitation and R less than approximately 3 mm h^{-1}, as described in coming sections. An accurate model of frozen and melting particles is required to expand the applicability of this algorithm beyond rain-only scenes.

The CPR is an excellent detector of precipitation because, unlike other radars, the instrument is sufficiently sensitive to the presence of small water droplets that even the incipient stages of precipitation formation can be detected (Stephens and Wood, 2007). The detection problem is distinct from quantification; equation (57), for example, should only be applied in those instances when rain is known to occur. Precipitation detection is based on the concept that unattenuated radar reflectivity increases as precipitation rate increases. The larger the value of this reflectivity in the range bins between 480 and 720 m above the ocean surface (given by Z_u), the more likely is precipitation at the surface. Since Z_u is simply the sum of the observed near-surface reflectivity, Z_{ns}, and the contributions from PIA and gaseous attenuation, then from equation (52),

$$Z_u = Z_{ns} + \sigma_{clr} - \sigma_0 \ . \tag{58}$$

Threshold values of Z_u have been chosen to indicate the likelihood of precipitation, as shown in Table 5.1. For example, using the precipitation and cloud water distribution described in this section, an unattenuated near-surface reflectivity of 0 dB or higher is nearly certain to produce appreciable rain, corresponding to about 0.03 mm h^{-1}. To produce the same precipitation rate in pure snow, DDA calculations (see section 5.1.6) suggest only -5 dB is required, so the threshold is adjusted accordingly when the ECMWF operation temperature profile indicates the entire atmosphere is colder than 0° C. For both rain and snow, Z_u less than -15 dB is unlikely to be associated with precipitation except, perhaps, the very lightest of drizzle [e.g. Stephens and Wood, 2007]. Intermediate values between these limits are assigned increasing likelihoods of precipitation occurrence.

Condition	Z_u range (dB)
Rain definite	> 0
Rain probable	-7.5 to 0
Rain possible	-15 to -7.5
Snow definite	> -5
Snow possible	-15 to -5
No precipitation	< -15

Table 5.1: Rain likelihood as defined by unattenuated near-surface reflectivity, Z_u.

5.1.5 Melting precipitation effects on PIA

Although it has been assumed that precipitation rate is constant with height, this does not necessarily mean that the profile of hydrometeor extinction need be constant. Precipitation may begin as snow, fall through a melting layer, and reach the surface as liquid. To simulate this effect, a model of the melting layer is developed that follows a snowflake as it makes the transition to rain drop. This model follows the general methodology employed by Klassen (1988), Hardaker et al. (1995), Szyrmer and Zawadzki (1999), and others, with one chief exception: the discrete dipole approximation (DDA) is used to represent the radiative properties of snow and weight the radiative properties of the particles during the beginning stages of melting. For now we will consider all hydrometeors as spheres, and will leave the DDA correction to be discussed later.

Microphysical model

The mass of any given rain drop and its corresponding melting particle and snow aggregate (m_r, m_m, and m_s) are taken to be equal throughout its lifetime, neglecting evaporation and the small amount of water that may collect on the particle due to vapor diffusion. Coalescence and drop breakup are neglected following Fabry and Zawadzki (1995), who found that these effects, while present, had little contribution to radar reflectivity during the melting process. With these assumptions,

$$\rho_w D^3 = \rho_m D_m^3 = \rho_s D_s^3 \,, \tag{59}$$

where ρ_w is the density of liquid water, D is the particle melted diameter, ρ_m and ρ_s are the densities of the melting particle and snowflake, and D_m and D_s are the diameters of the same. The mass of snowflakes is taken to follow the power-law relation

$$m_s = \alpha_{m,s}\, D_s^{\beta_{m,s}} \,, \tag{60}$$

with D_s and ρ_s (truncated between 5 and 917 kg m^{-3}) following from (59) and (60). The values of constants used in this section are given in Table 5.2. It is further assumed that the density of the melting particle is related to the inverse of the mass fraction of melt water in the particle, f:

$$f = \frac{m_w}{\rho_w D^3} \tag{61}$$

$$\rho_m = \frac{\rho_s \rho_w}{f\rho_s + (1-f)\rho_w} \,, \tag{62}$$

where m_w is the mass of melt water, such that the density of the particle smoothly varies between that of the initial snow aggregate and the final raindrop.

The melting model for spherical particles used in this study is the formulation of Szyrmer and Zawadzki (1999) (hereafter SZ99), whereby the energy used to melt snow aggregates is supplied by the ambient environment and the latent heat that is released as water vapor condenses on the particle. With some key assumptions, SZ99 demonstrate the following relation between the energy used per unit time to

Symbol	Value
$\alpha_{m,s}$	0.07854 kg $m^{-\beta_{m,s}}$
$\alpha_{v,s}$	60.74 kg $m^{-\beta_{v,s}}$
$\alpha_{v,r}$	627.714 kg $m^{-\beta_{v,r}}$
$\beta_{m,s}$	2.0
$\beta_{v,s}$	0.61
$\beta_{v,r}$	0.7619
ρ_i	917 kg m^{-3}
ρ_w	1000 kg m^{-3}
L_f	3.34×10^5 J kg^{-1}
L_v	2.5×10^6 J kg^{-1}
K	2.4×10^{-4} J cm^{-1} K^{-1} s^{-1}
D_v	2.77×10^{-7} m^3 cm^{-1} s^{-1}
A_{fm}	1.7
B_{fm}	33.0 $cm^{-0.7}$

Table 5.2: Values of constant quantities used in the manuscript.

melt the particle (which is related to the change of melt water), the heat available from the environment, and the heat released as vapor condenses on the particle:

$$L_f \frac{\mathrm{d}m_w}{\mathrm{d}t} = \frac{\mathrm{d}q}{\mathrm{d}t} + L_v \frac{\mathrm{d}m_{cond}}{\mathrm{d}t} \,, \tag{63}$$

where L_f is the latent heat of fusion, L_v is the latent heat of vaporization, $\mathrm{d}q$ is the heat transferred across from the environment to the surface of the particle, and $\mathrm{d}m_{cond}$ is the mass of vapor that condenses onto the particle surface. The rate of energy transfer between the environment and the melting particle is a function of the temperature difference δT across the surface of the particle (and thus the environmental lapse rate Γ_e), the efficiency of heat conduction in the atmosphere, ventilation effects, and the size of the particle. SZ99 demonstrate that

$$\frac{\mathrm{d}m_w}{\mathrm{d}t} = \frac{2\pi B_{fm}}{L_f} \left(K\delta T + D_v L_v \delta\rho_v\right) D^{A_{fm}} \,. \tag{64}$$

where A_{fm} and B_{fm} are parameters determining the ventilation coefficient, K is the thermal conductivity of air at 273.15K, D_v is the water vapor diffusivity in air, and $\delta\rho_v$ is the vapor density difference across the particle calculated from the Clausius-Claperyon equation.

As in SZ99, aggregation or drop breakup are not considered, such that one snowflake melts into one raindrop [e.g. Toit (1967); Ohtake (1969); Fabry and Zawadzki (1995). If the concentration of droplets in the melting and snow phase are given by N_m and N_s, respectively, then this assumption requires the flux of particle number density to be conserved (Klassen, 1988). Noting that both N and fall speed U are defined in terms of equivalent melted diameter, then for snow, melting particles, and rain:

$$N_s(D)\,U_s(D) = N_m(D)\,U_m(D) = N(D)\,U_r(D)\,, \tag{65}$$

where $N(D)$ is given by equation (54). The fall velocity of rain and snow are taken to follow power law relations,

$$\begin{aligned} U_r(D) &= \alpha_{v,r}\, D^{\,\beta_{r,r}} \\ U_s(D) &= \alpha_{v,s}\, D^{\,\beta_{r,s}}\,, \end{aligned} \tag{66}$$

while for melting particles the Battaglia et al. (2003) parameterization is used:

$$\begin{aligned} U_m(D) &= \gamma\,(u_r - u_s) + u_s\,, \\ \text{with } \gamma &= \frac{f + f^2}{9.2 - 3.6(f + f^2)}\,. \end{aligned} \tag{67}$$

Differentiating equation (61) with respect to time and using the chain rule to introduce s as the independent variable,

$$\frac{\mathrm{d}f}{\mathrm{d}s} = \frac{\mathrm{d}f}{\mathrm{d}t} \cdot \frac{\mathrm{d}t}{\mathrm{d}s} = \frac{\mathrm{d}f}{\mathrm{d}t} \cdot \frac{1}{w - U_m} , \tag{68}$$

with w representing the large scale vertical motion. w can be neglected with relatively small error in stratiform rain scenarios, but may be significant in deep convection; ideally, *a priori* information about w could be used in this calculation. Combining with (64) results in

$$\frac{\mathrm{d}f}{\mathrm{d}s} = -\frac{12\, B_{fm}\, D^{\,A_{fm}}}{L_f\, \rho_m\, D_m^3\, U_m} \, (K\delta T + D_v L_v \delta\rho_v) \ . \tag{69}$$

When this equation is integrated over height, one obtains the desired expression for the melted fraction f_j of a particle of melted diameter D, at any height H_j:

$$\begin{aligned} f_j(D,s) &= \int_0^{f_j} \mathrm{d}f \\ &= -\frac{12 B_{fm}\, D^{A_{fm}}}{L_f} \int_{H_f}^{H_j} \frac{K\, \delta T(s) + D_v\, L_v\, \delta\rho_v(s)}{\rho_m(s)\, D_m{}^3(s)\, U_m(s)}\, \mathrm{d}s \end{aligned} \tag{70}$$

where H_f is the height of the freezing level. Choosing a suitable height increment, approximately 30 m, equation (70) is integrated downward in height for each particle in the distribution, starting with a melted fraction of zero and increasing until the fraction becomes unity. When a particle of a given size is completely melted, it is transferred to the 'rain' category. The assumed in-cloud environmental lapse (taken to be 3 K km^{-1}) is used to calculate δT and $\delta\rho_v$.

Radiative transfer model

The formulation of the melting layer model outlined above predicts the melted fraction as a function of height and melted diameter, D. Although rain drops and highly melted particles may be modeled as spheres, dry snowflakes are highly non-spherical. Liu (2004) showed that significant errors are incurred when dry snow flakes are modeled as variable density "soft spheres" at cloud radar frequencies, since non-Rayleigh effects quickly increase with particle size. A better solution is to represent these snowflakes using DDA, whereby complex ice habits can be constructed as a collection of closely-spaced dipoles that interact with each other and incident radiation to produce a scattered electric field. At some point, when melting has progressed sufficiently, the particles begin to take on a more spherical form, and a spherical representation containing a mixture of air, ice, and water is appropriate. The transition between these two states is difficult to represent in a physical model, so a hybrid model is adopted that ensures a smooth translation between the optical properties of the snowflake and the partially melted sphere.

First, the optical properties of the partially melted spherical particles are derived. The volume fraction of each species (air, liquid water, ice) must be determined as a function of melted fraction for particles of all sizes. Since the sum of the volume fractions of air, liquid water, and ice must be unity, it can be easily shown that

$$
\begin{aligned}
f_w &= \frac{\rho_m}{\rho_w} f \\
f_a &= \frac{\rho_m \left[1 - \rho_i - f\left(1 - \frac{\rho_i}{\rho_w}\right)\right]}{\rho_a - \rho_i} \\
f_i &= 1 - \frac{\rho_m \left[1 - f\left(1 + \rho_a\right) - \frac{\rho_i}{\rho_m}\right]}{\rho_a - \rho_i} \, .
\end{aligned}
\tag{71}
$$

The index of refraction of mixed phase hydrometeors follows using a three-component variation on the traditional two-component Bruggeman formulation [Bruggeman (1935); Johnson and Petty (2008). Using this information, the single-scatter scatter, extinction, and backscattering coefficients may then be calculated as a function of height for each profile,

$$\begin{bmatrix} k_{sca,o} \\ k_{ext,o} \\ \eta_o \end{bmatrix} = \frac{\pi}{4} \int_0^\infty \begin{bmatrix} Q_{sca}(D) \\ Q_{ext}(D) \\ Q_{sca}(D)\, p_o(\Theta = 180, D) \end{bmatrix} \left[N_m(D) + N_c(D) f_{tot}\right] \, D_m^2 \, \mathrm{d}D \, , \tag{72}$$

with the distribution-integrated phase function following as

$$P_o(\Theta) = \frac{\pi}{4\, k_{sca,o}} \int_0^\infty p_o(\Theta, D)\, Q_{sca}(D) \left[N_m(D) + N_c(D) f_{tot}\right] \, D_m \, \mathrm{d}D \, . \tag{73}$$

Here Q_{sca} and Q_{ext} are the scattering and extinction efficiencies, respectively, and p_o is the phase function ($\Theta = 180$ indicating the backscatter direction) calculated from Mie theory. In this formulation, the cloud water droplet number concentration has been scaled by the total melted fraction of particles in the distribution,

$$f_{tot} = \frac{\int_0^\infty f \cdot D^3 \, \mathrm{d}D}{\int_0^\infty D^3 \, \mathrm{d}D} \, . \tag{74}$$

Moving from spheres to more complex ice habits, DDA calculations of the scattering and extinction efficiencies and phase function of snow flakes of various sizes were obtained from the microwave single-scatter property database for non-spherical ice particles constructed by Liu (2004). Individual snowflakes are simulated as aggregates of hexagonal columns. The 6-arm bullet rosettes is chosen for this study because they provide reasonable reflectivity and attenuation profiles when integrated over an exponential size distribution. The area ratio of the bullets, defined as the ratio of the cross sectional area of the particle to that of a circumscribed sphere with diameter equal to the maximum particle dimension D_{max}, is given by

$$A_r = 0.125\, D_{max}^{-0.351}\,, \tag{75}$$

(in cgs units) a relation derived by Heymsfield and Miloshevich (2003) based on measurements from the Cloud Particle Imager probe. The database was used to derive the scatter, extinction, and backscattering coefficients ($k_{ext,d}$, $k_{sca,d}$, η_d) as well as the phase function $P_d(\Theta)$ using equations analogous to (72) and (73).

The equivalent "hybrid" electromagnetic properties can then be evaluated as a mixture of those of a soft sphere and pure snowflake:

$$\begin{bmatrix} k_{ext,m} \\ k_{sca,m} \end{bmatrix} = \zeta \begin{bmatrix} k_{ext,o} \\ k_{sca,o} \end{bmatrix} + (1-\zeta) \begin{bmatrix} k_{ext,d} \\ k_{sca,d} \end{bmatrix} \tag{76}$$

$$P_m(\Theta) = \frac{1}{k_{sca,m}} \left[\zeta\, k_{sca,o}\, P_o(\Theta) + (1-\zeta)\, k_{sca,d}\, P_d(\Theta) \right]\,,$$

with

$$\zeta = \begin{cases} f/f_c & , f < f_c \\ 1 & , f \geq f_c\,, \end{cases} \tag{77}$$

and the backscattering coefficient of the mixture follows as

$$\eta_m = k_{sca,m}\, P_m(\Theta = 180)\,. \tag{78}$$

When the total melted mass fraction reaches f_c, taken to be 0.25 in this study, the particles revert to pure spheres. In this way the the electromagnetic properties are nudged toward the DDA values in the initial stages of melting, but revert to spheres containing ice, air, and liquid water as melting progresses.

Now, finally, the radar reflectivity can be calculated as a function of radar range, r. The equivalent radar reflectivity (units of dBZ) is defined as

$$Z_e(r) = 10\log_{10}\left[\frac{\lambda^4}{\pi^5\left|K^2\right|}\eta_m \exp\left(-A(r)\right) \times 10^{18}\right] , \tag{79}$$

where λ is the radar wavelength, $|K^2|$ is the radar dielectric constant, with the attenuation between the radar and range r given by

$$A(r) = 2\int_0^r k_{ext,m}(s')\,\mathrm{d}s' . \tag{80}$$

An example of the melting layer model output is shown in Figure 5.7 (multiple scattering is included; this is discussed in the next section). Here a 2 mm h^{-1} liquid equivalent precipitation rate was simulated with a lapse rate of 3 K km^{-1}. The thick gray lines show the results with DDA-modeled snowflakes, and the thin solid lines the results for spheres. The radar reflectivity profiles both show a bright band approximately 300 m below cloud top. The spheres-only bright band is more pronounced, primarily because the backscatter efficiency of the volume of DDA-simulated snowflakes at cloud top is higher than that of the melted rain drops at cloud base. It is noted that the presence of a bright band at 94 GHz is often due largely to attenuation effects in the rain below the freezing level, consistent with the findings of Sassen et al. (2007).

The attenuation profile in both cases peaks near the level of the bright band. The attenuation profile, and thus Z_e, are most uncertain at and just below the freezing level because of uncertainties in ice crystal habit. Once melting has pro-

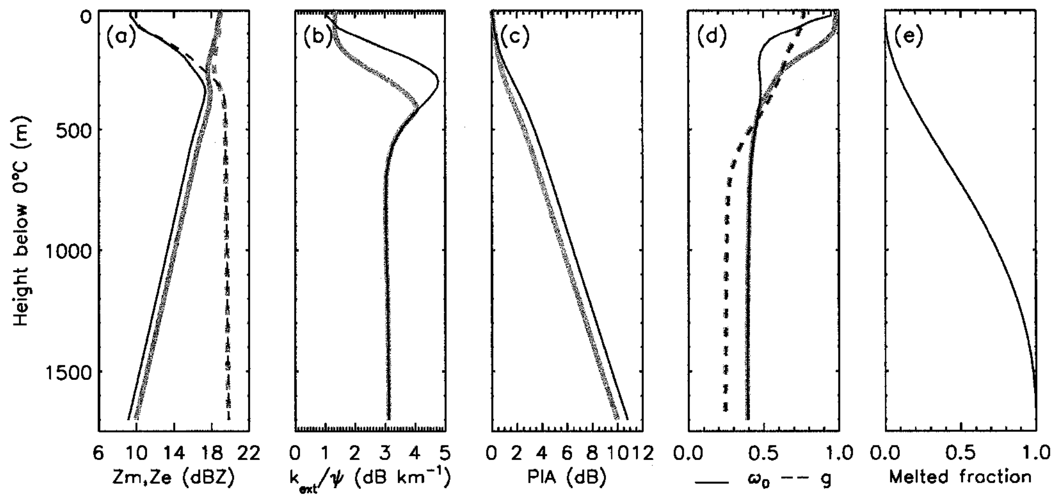

Figure 5.7: Melting layer model output with DDA (thick gray lines) and soft spheres (thin black lines). (a) Radar reflectivity, both attenuated (solid) and unattenuated (dashed); (b) Attenuation coefficient; (c) PIA; (d) single scattering albedo (solid) and asymmetry parameter (dashed); (e) melted fraction.

gressed sufficiently, depending partially on the value chosen for f_c, the two methods become nearly identical. PIA, however, is an integrated quantity, and as such the effects of melting near the freezing level propagate downward through the column to the surface. A chief results here is that the presence of a melting layer tends to produce more PIA (through the enhancement just below the melting level) than would result if only warm rain were considered. Therefore, neglecting this additional melting layer contribution to PIA causes a high bias in retrieved precipitation rates.

5.1.6 Multiple scattering effects

The Mie solution to particle scattering, as utilized in the rain-only formulation described in section 5.1.4, is a single-scatter solution only. Multiple scattering (MS), by contrast, occurs when photons undergo two or more scattering events between the transmitter and receiver. The MS problem is familiar to the lidar community [Bissonnette (1988) and others], but has traditionally been less problematic for radar systems. Two chief factors conspire to make MS a factor that cannot be ignored for spaceborne cloud radars like the CPR. First, at W-band scattering by rain and precipitating ice can be significant; the single scatter albedo, ω_0, for rain approaches 0.5, and for snow is often greater than 0.9. The asymmetry parameter, g, which represents the degree of forward scattering, is also particularly high for snow (often greater than 0.8). Second, the CPR field of view (FOV) is characterized by a relatively large cross-track footprint (nominally 1.4 km). Since at W-band this is larger than the mean free path of photons in even moderately raining systems, the probability of more than one scattering event is relatively high.

In heavy precipitation events photons may be scattered several times before arriving at the receiving antenna. This time delay translates into an increase in the apparent range of the source of the scatter. Therefore MS manifests itself as an increase in return power, and thus radar reflectivity, at range gates farther from the radar than the source of the initial scattering event. An indicator of MS in heavy rainfall, often observed by the CPR, is the occurrence of an elevated reflectivity layer that is apparently positioned below the Earth's surface [see Battaglia et al. (2008)].

To investigate and quantify the effects of multiple scattering, the CloudSat viewing geometry was incorporated into a backward Monte Carlo modeling of the radiative transfer equation [O'Brien (1992); O'Brien (1998)]. Backward Monte Carlo models conceptually work by firing photons from the receiver antenna and tracing backward, through an absorbing and scattering medium, to the transmitter. Some calculations of received power, P_r, for a homogeneous 4000 m thick raining column are shown in Figure 5.8. Two examples are shown, one for a rain rate of 1 and the other for 5 mm h^{-1}. At 1 mm h^{-1} nearly all the return power is in the first order scatter (i.e. the backscatter), with the slope of the backscatter power line relating directly to the single-scatter attenuation coefficient. The power returned from second order scatter is an order of magnitude less than the backscatter, and therefore second order and higher terms may be neglected. In this case, the traditional radar equation adequately represents the profile of backscattered energy. At 5 mm h^{-1}, however, contributions from higher orders of scatter increase rapidly with depth into the cloud. At cloud base the contribution of terms third order and higher is larger than that from single scatter. Thus it is clear that multiple scattering can only be neglected when rain rates are small, and in practice a value of 3 mm h^{-1} or less is suggested, although more rigorous criteria based on PIA are introduced in Battaglia et al. (2008). In all cases it is noteworthy that MS tends to increase the received power at levels below the precipitation top height, and thus the contribution from MS can also appreciably increase the backscatter from the range bin intersecting the surface. From (52) this indicates that for a given R and raining layer depth, the apparent PIA with MS is smaller than that expected from single-scatter theory only.

The formulation of the full precipitation retrieval algorithm, which includes both melting and multiple scattering effects, proceeds as follows. First, a database of received powers as a function of depth below cloud top, freezing level height, and environmental lapse rate is created for a finite set of cloud depths and rain rates. These received powers follow from application of the backward Monte Carlo model, and the power profiles are converted to profiles of attenuated backscattering

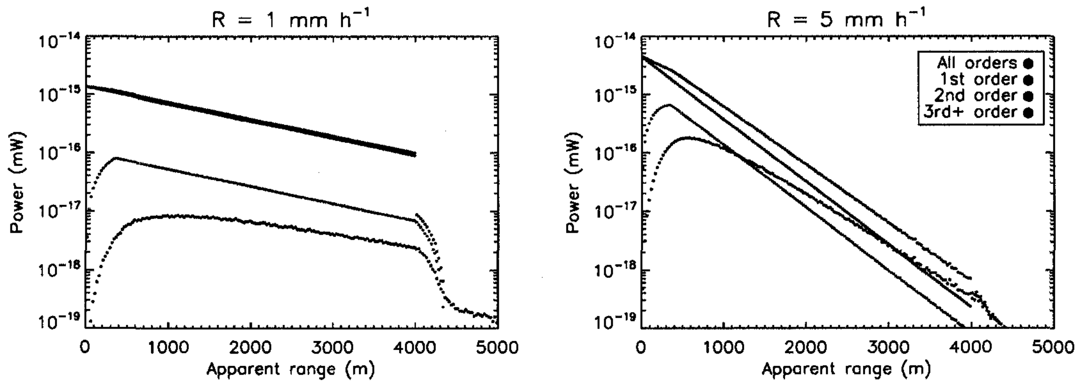

Figure 5.8: Simulated received power as a function of apparent range for a 4000 m thick cloud raining at a constant 1 mm h^{-1} (left) and 5 mm h^{-1} (right), relative to 1 mW transmit power. Color indicates order of scatter.

coefficient, η_{MC}, through the radar equation,

$$\eta_{MC} = \frac{P_r}{P_t} C\, r^2 \,, \tag{81}$$

where P_t is a reference transmit power, C is a calibration constant determined from boundary conditions at the top of the profile, and r is the range to the target. The corresponding attenuated reflectivity is then

$$Z_{MC} = 10 \log_{10} \left(\frac{\lambda^4}{\pi^5 \left| K^2 \right|} \eta_{MC} \times 10^{18} \right) \,. \tag{82}$$

and the apparent PIA for the profile (i.e. that which includes the effects of multiple scattering) is given by

$$PIA_{app} = Z_u(CB) - Z_{MC}(CB) \,, \tag{83}$$

where Z_u is the unattenuated reflectivity derived from evaluation of equation (13) with A set to zero, and CB refers to the level of the cloud base.

Following generation of this database, the algorithm is applied to CPR profiles where precipitation is occurring (as discussed in section 5.1.3), utilizing the ECMWF analyzed temperature structure matched to the CPR footprint to determine the height of the freezing level. When the melted fraction at the surface is less than 0.8, determined from the assumed lapse rate, no quantitative retrieval is performed (although the occurrence of precipitation may still be determined). This criterion is enforced to avoid uncertainties associated with mixed phase precipitation near the surface, and because uncertainties associated with the algorithm are largest when the freezing level is low (discussed further in Section 5.1.7). The appropriate table is selected using the observed liquid/mixed layer depth, frozen precipitation depth, and freezing level height. The liquid/mixed layer depth is taken to be the lesser of the cloud top height of the lowest cloud layer, derived from the reflectivity profile, and the freezing level height. The effects of purely frozen precipitation on PIA are only considered when a core of significant radar return ($>$ 10 dBZ) extends in a continuous column above the freezing level. This is generally only the case in convective cores, and represents less than 6% of CloudSat retrievals. Finally, the observed PIA is matched to the apparent PIA's contained in the table to derive an associated rain rate.

Some examples of calculated PIA versus rain rate relations for warm rain only, with and without multiple scattering effects, are shown in Figure 5.9. It is apparent that for very light rain, MS has a negligible contribution to PIA. Above a few millimeters per hour, however, the MS contribution can be significant. For example, consider a 0.8 km deep raining layer with an observed PIA of 15 dB; the retrieved rain rate without MS is approximately 13 mm h^{-1}; with MS it is

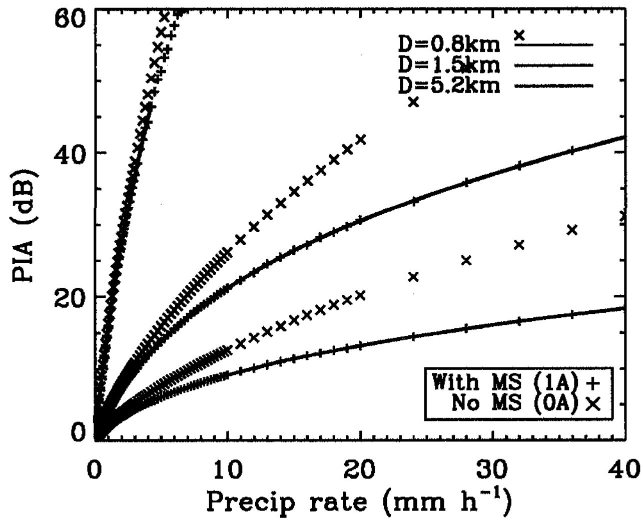

Figure 5.9: PIA calculated as a function of rain rate for various precipitating layer depths, with and without multiple scattering.

nearly 30 mm h^{-1}. Since MS adds energy to the surface return, the apparent PIA required to achieve the same rain rate is reduced when properly accounting for MS; failure to account for MS biases retrieved rain rates low.

As discussed earlier, at W-band precipitating ice has both a high single scattering albedo and asymmetry parameter (Figure 5.7), and as a result significant MS can occur. MS tends to "turn on" quickly above a threshold precipitation rate, as demonstrated also in Battaglia et al. (2007). This is also found to be the case with the full algorithm. Figure 5.10 shows precipitation retrievals for one day of CloudSat orbits. The blue points indicate retrievals with only rain, and the red points are retrievals containing a mix of precipitating ice, melting particles, and possible rain. The tendency to underestimate R without properly accounting for MS is demonstrated by the departure of the blue points from the one-to-one line. The rapid turn-on of ice phase scattering at approximately 2-3 mm h^{-1} and large

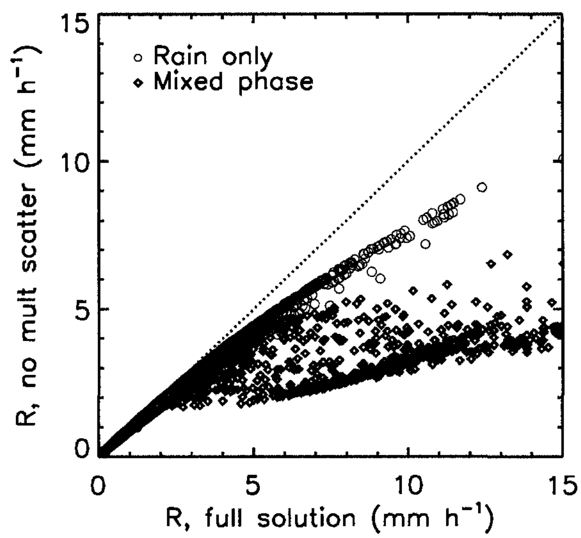

Figure 5.10: One day of CloudSat-based precipitation retrievals. Blue points contain only rain, red points contain a mixture of precipitating ice, melting particles, and possibly rain.

departures from single-scatter theory are also apparent.

Combining the effects of attenuation, MS, and particle melting together, one can estimate the maximum possible retrievable precipitation rate (MRP) for the CPR using this method. Although the CPR is capable of detecting more than 50 dB of two-way attenuation, Battaglia et al. (2008) suggest a cutoff of approximately 40 dB for the applicability of surface reflectance technique (SRT) methods such as the present retrieval. It is argued that when PIA exceeds this threshold, MS in the atmosphere is so significant that it potentially masks scattering from the surface itself. Thus, using this 40 dB threshold, a conservative estimate of the MRP may be obtained as a function of precipitating layer depth and freezing level height (Figure 5.11). For warm rain (points above the one-to-one line), MRP is a function of precipitating layer depth only; while it is possible to retrieve 25 mm h^{-1}

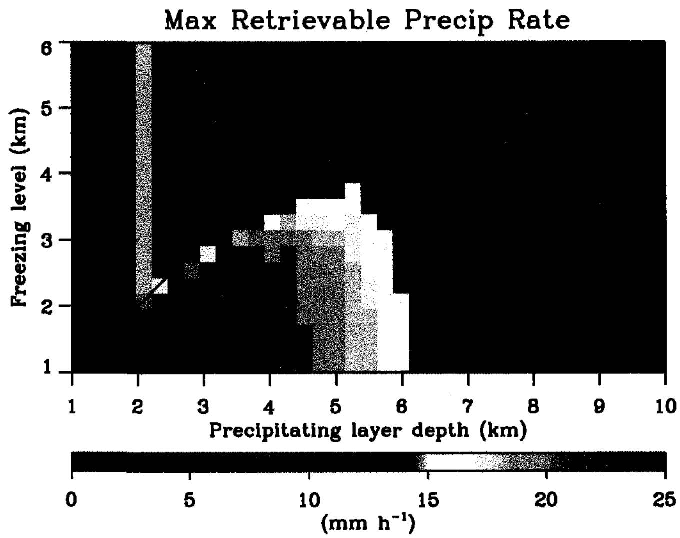

Figure 5.11: Maximum retrievable precipitation rate, estimated using a conservative 40 dB PIA cutoff for applicability of SRT methods.

or greater for a 1 km deep system, this reduces to about 7 mm h^{-1} for a 4 km deep system. When melting effects are considered, MRP increases since MS by ice and melting particles tends to increase return power, providing additional measurable signal (whereas attenuation acts to decrease it).

5.1.7 Uncertainty analysis

When making deductions about a physical quantity by applying measurements to a forward model, it is important to quantify the sensitivity of the model to the measurements, input parameters, and various assumptions, as well as the measurement uncertainties of the instrument. To this end an uncertainty analysis is performed. Six parameters are considered as chief contributers to uncertainty in precipitation rate using this method: the cloud to rain water ratio, the drop size distribution, the environmental lapse rate, the slope of the rain profile, the height of the freezing level, and the uncertainty in measured PIA. To test the influence of these parameters on retrieved precipitation rates, the retrieval is run multiple times on two full weeks of near-global CloudSat observations, each time perturbing one of these parameters by an amount sufficient to capture the uncertainty in the parameter. Considering a system of p independent parameters such that covariances may be neglected, the total fractional uncertainty in retrieved precipitation rate, ϵ, is given by the square root of the sum of the squares of the fractional uncertainty in each parameter,

$$\epsilon_{i,j} = \sqrt{\sum_{k=1}^{p} \left[\left(\frac{\delta R_k}{R_{i,j}} \right)^2 \right]} \, . \tag{84}$$

Here the uncertainties are broken down into 25 precipitation rate bins between 0 and 25 mm h^{-1}, and 10 freezing level height bins between 1 and 6 km, with bin numbers represented by the i and j subscripts. The fractional uncertainty in retrieved precipitation rate due to each of these parameters is shown in Figure 5.12.

To assess the influence of the ratio of assumed cloud to rain water content, the ratio is varied by a factor of 2 in both the positive and negative directions. This ratio reflects uncertainty in whether attenuation is due to cloud drops or precipitation drops, and also the inherent ambiguity between the two during the incipient stages of precipitation formation. Since the ratio is largest for small R (Figure 5.5), it is not surprising that the fractional uncertainty is largest (about 0.6) for $R < 0.1$ mm h^{-1}, but drops off quickly as R increases.

To test the effects of DSD, two different modified gamma distributions of precipitation drops of the form used in the TRMM PR 2A25 algorithm are substituted

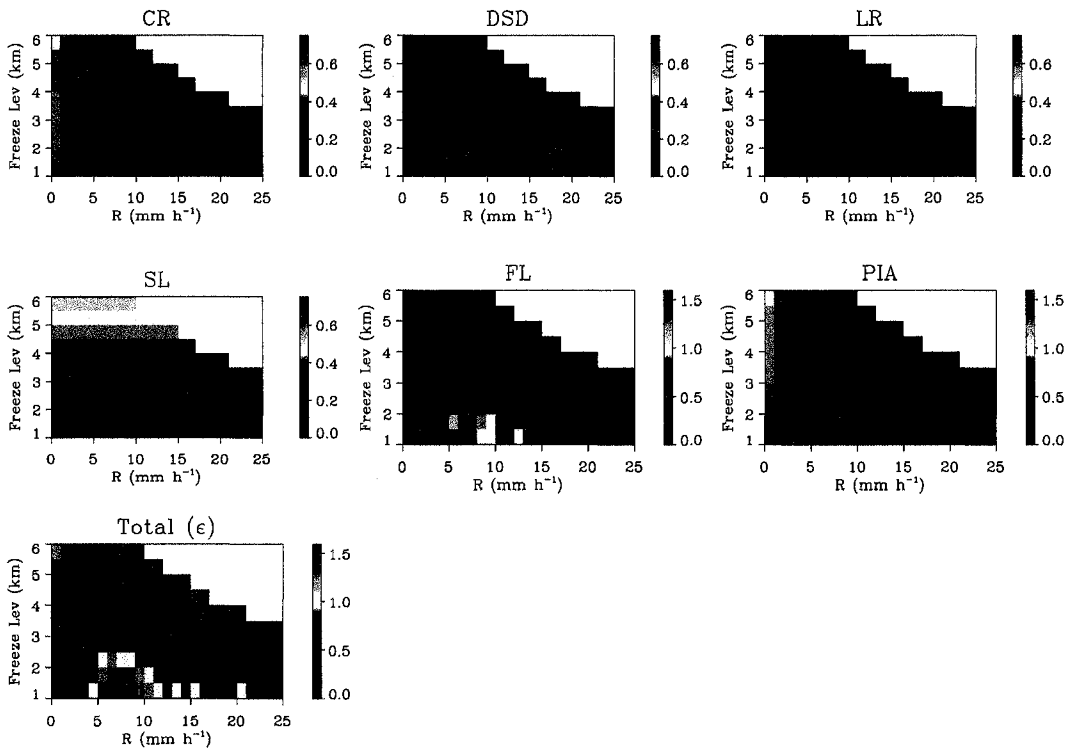

Figure 5.12: Fractional uncertainty in retrieved precipitation rate due to each of six parameters (CR - cloud to rain water ratio; DSD - drop size distribution; LR - environmental lapse rate; SL - rainfall slope; FL - freezing level height; PIA - measured path integrated attenuation) as a function of precipitation rate and freezing level height. Total fractional uncertainty is shown in the last panel.

for the assumed Marshall-Palmer distribution:

$$N(D) = N_0\, D^{\mu} \exp\left(-\left[\frac{3.67+\mu}{D_0}\right] D\right) , \tag{85}$$

with μ taken the be 3. The values of N_0 and D_0 are derived as a function of R from the TRMM stratiform and convective power law relations between radar reflectivity and rain rate (Iguchi et al., 2000) as well as the rain drop fall velocity relations described in Section 5.1.5. Resulting fractional uncertainties in R are generally less than 30%, being largest for moderate rain rates at low freezing levels. The magnitude of these uncertainties is consistent with the findings of Matrosov (2007), who estimated DSD-related uncertainties in rain rate from a PIA-based method based on observed DSD's. Perturbing the environmental lapse rate by 1 K km^{-1} each direction from the assumed 3 K km^{-1} is shown to have a smaller overall effect than perturbing the DSD, but the effects are concentrated in similar regimes.

The retrieval algorithm assumes a constant rainfall profile below the freezing level, as described in Section 5.1.4. To assess errors in retrieved rain rate produced by rain profiles that vary with height, sets of rain profiles are constructed that vary linearly between the surface and the freezing level. The slope of these profiles, normalized by the mean rain rate, is taken to vary between -0.15 km^{-1} and 0.03 km^{-1}, with a negative slope indicating rain rate increasing toward the surface. These representative slopes are based on the work of Fu and Liu (2001) who analyzed the shape of precipitation profiles observed by the TRMM PR. They found that although stratiform rain profiles are generally height invariant below the freezing level, convective rainfall may either increase or decrease between the freezing level and the surface. Applying these perturbed rain profiles to the current algorithm is found to produce uncertainties that are very small compared with the inherent uncertainty arising because the surface rain rate may vary considerably from the column mean; it is these errors that are reflected in the fourth panel of Figure 5.12. The fractional uncertainty is shown to vary between approximately 0.1 and 0.6, with the largest errors associated with the highest freezing levels.

Uncertainties due to specification of the freezing level are a function of uncertainty in the ECMWF temperature. Assuming a 0.73 K uncertainty in temperature at 700 hPa (Eyre et al., 1993) and a in-cloud lapse rate of 3 K km^{-1}, this translates to a height uncertainty of approximately 250 m. This is doubled to ensure a conservative estimate, resulting in a perturbed freezing level height of 250 m in either direction. The resulting uncertainties are greatest for low freezing level heights, since R is most sensitive to PIA when precipitation layer depth is small. When the freezing level is low and R is between 5 and 10 mm h^{-1}, the fractional uncertainty approaches 2. This is because multiple scattering by ice in this regime tends to partially compensate for attenuation effects in the rain below [see Battaglia et al. (2007)], producing a regime where apparent PIA is nearly invariant over a range of R.

Finally, uncertainties in the measured PIA are assessed by perturbing these measurements by one standard deviation, the value of which depends on wind speed (see Section 5.1.3). The resulting uncertainties are largest for small R, and again for lower freezing level heights. The resulting total fractional uncertainties are shown in the last panel of Figure 5.12. As expected, there are two regimes where fractional uncertainty in retrieved R can be expected to exceed 100% when the precipitation rate is less than about 0.5 mm h^{-1}, and when the freezing level is below 2 km and the precipitation rate is between approximately 5 and 10 mm h^{-1}.

In practice, uncertainties are expected to be largest in the middle and higher latitudes in storm systems with moderate precipitation.

5.1.8 Results

The full algorithm is applied to CloudSat data to produce near-global precipitation distributions. These results are also compared with other data sets. One of the most direct possible comparisons is with the passive microwave, GPROF-based precipitation estimates from AMSR-E. AMSR-E passes over any given scene within approximately 60 seconds of the time it is viewed by the CPR. It is noted that the CloudSat footprint is considerably smaller than the 14 by 8 km footprint of the 37 GHZ channel of AMSR-E, such that there may be considerable variability captured by the CPR within the AMSR-E FOV. Recognizing this limitation, retrieved oceanic rainfall at the CPR resolution is matched to the nearest AMSR-E retrieval for two seasons of observations.

Figure 5.13 shows the zonal mean occurrence of liquid precipitation (the "rain definite" category of Table 5.1) as observed by CloudSat for December through February 2006-2007 (DJF) and June through August 2007 (JJA). Each panel suggests a trimodal structure of precipitation occurrence, with peaks in the intertropical convergence zone (ITCZ) and both the northern and southern mid-latitude storm tracks. The CPR results compare well with AMSR-E in all rain rate categories in the tropics and subtropics. Considerable differences are present in higher latitudes, where the CPR observes nearly twice the precipitation occurrence as AMSR-E in some latitude bands. These differences are particularly pronounced in region of the southern hemisphere winter storm tracks. These high-latitude differences are not unexpected since the GPROF cloud property database that forms

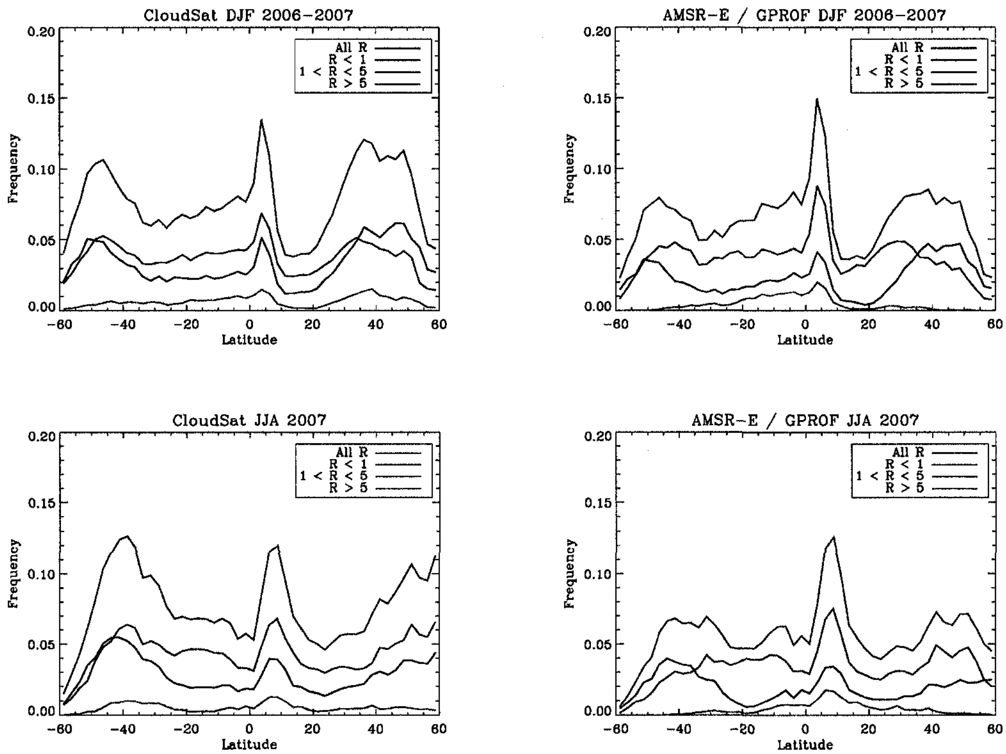

Figure 5.13: Frequency of occurrence of oceanic, liquid precipitation by rate category (indicated by colors). Top row is DJF 2006-2007, bottom row JJA 2007. Left side CloudSat, right side colocated AMSR-E.

the basis of the AMSR-E rain retrieval is tuned to tropical cloud systems. More results on the frequency of occurrence of precipitation observed by CloudSat, particularly in relation to the types of cloud systems present, may be found in Haynes and Stephens (2007).

The full retrieval algorithm is also compared against direct matches with TRMM PR overpasses. Although TRMM flies in a lower altitude, higher inclination orbit that the A-Train, crossovers occur approximately twice per day. A crossover match is considered to be any oceanic observation where the center of the TRMM and CPR footprint fall within 3.5 km and 5 minutes of each other. Since the nadir footprint of the PR, about 5 km, is larger than the CPR footprint, up to seven overlapping CPR precipitation rates must be averaged together for comparison with a single PR precipitation rate. The period from June 2006 to November 2007 was scanned for crossover matches in the tropical region between 30° south and 30° north latitude, resulting in approximately 30000 independent PR footprints where either PR or CPR observed rain.

A histogram of precipitation rates resulting from these crossover matches is shown in Figure 5.14. First, it is noted that the CPR observes more rain than the PR, particularly for $R < 2$ mm h^{-1}. The CPR peak occurs at about 0.5 mm h^{-1} whereas the PR peak is closer to 1.3 mm h^{-1}. This is an expected consequence of the higher sensitivity of the CPR. Second, for higher precipitation rates, the counts are comparable. The PR observes more rainfall in excess of approximately 12 mm h^{-1} than the CPR, which is also expected given the aforementioned limitations of attenuation-based methods at millimeter wavelengths.

An example crossover match from the central Pacific on 1 December 2006 is shown in Figure 5.15. The CPR is sensitive to both clouds and precipitation, so

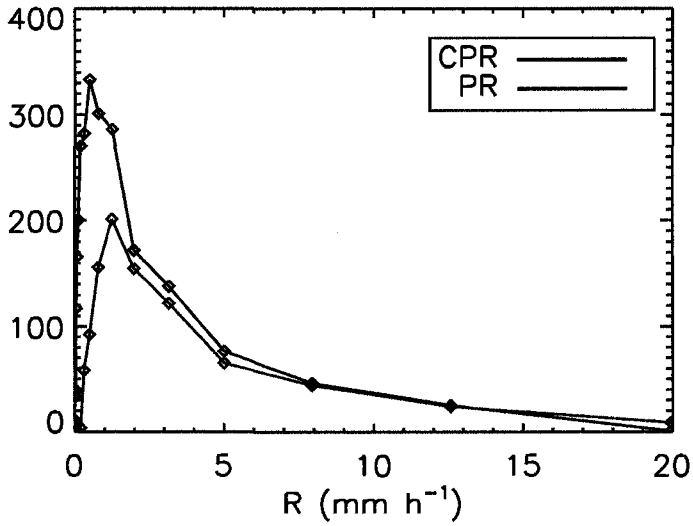

Figure 5.14: Histogram of frequency of occurrence of precipitation viewed by the TRMM PR and CPR for all crossover matches between 30° south and 30° north latitude, during the period from June 2006 to November 2007. Bin size increases with R, as shown by the diamond symbols.

the area of detectable reflectivity covers a much larger area than what is observed by the PR. In this example the CPR detects precipitation (particularly less than 1-2 mm h^{-1}) more often than the PR, consistent with the aggregated statistics shown in Figure 5.14. The period between 34.7 and 35.2° latitude is notable and illustrates this point; here the PR detects no significant reflectivity, but the CPR observes constant light precipitation falling through a bright band feature near 4.5 km. There are also periods when the PR retrieves heavier precipitation than the CPR, such as near 33.9° latitude. In this case the CPR beam is significantly (but not completely) attenuated. It should be noted that individual retrievals may differ for reasons other than the methodology utilized, including differences due to the time and distance parameters that define a match, spatial translation of the precipitation systems, and footprint differences between the two sensors.

Finally, Figure 5.16 shows the accumulated water mass as a function of latitude derived from the CPR and a variety of other datasets during the DJF 2006-2007 season (now presented at their native resolutions with no "matching" performed). In addition to AMSR-E and the TRMM PR, data from the TRMM Microwave Imager (TMI) and the Global Precipitation Climatology Project (GPCP) are also displayed. GPCP combines precipitation observations from a variety of sources aiming to formulate a climatological "best estimate" of accumulated global rainfall (Adler et al., 2003). This figure shows two distinct tropical peaks, one north of the equator representing the primary ITCZ, and one south of the equator resulting from a split ITCZ. Between 20° N and 20° S latitude, agreement is fair, with total CPR accumulated rainfall varying from 69 to 176% the mean of the AMSR-E, PR, and TMI results. The CPR retrieval accumulates less precipitation in the southern branch of the ITCZ, and this is likely related to the fact that the CPR signal

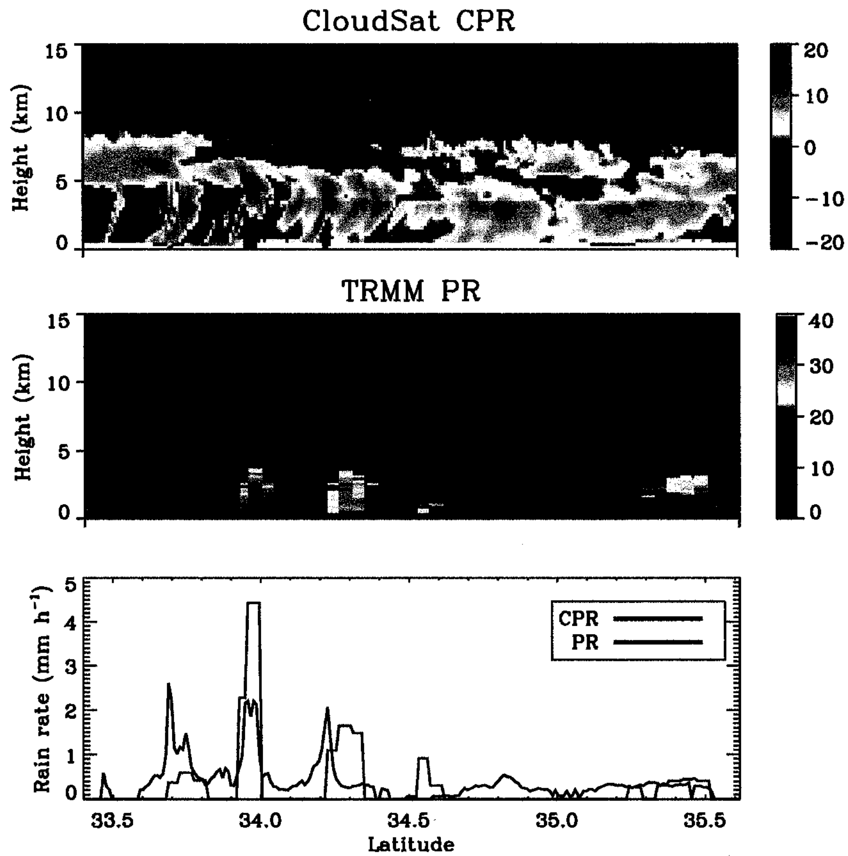

Figure 5.15: CPR reflectivity (dBZ, top panel), PR reflectivity (dBZ, middle panel), and rain rate retrievals (bottom panel) for a 1 December 2006 crossover match.

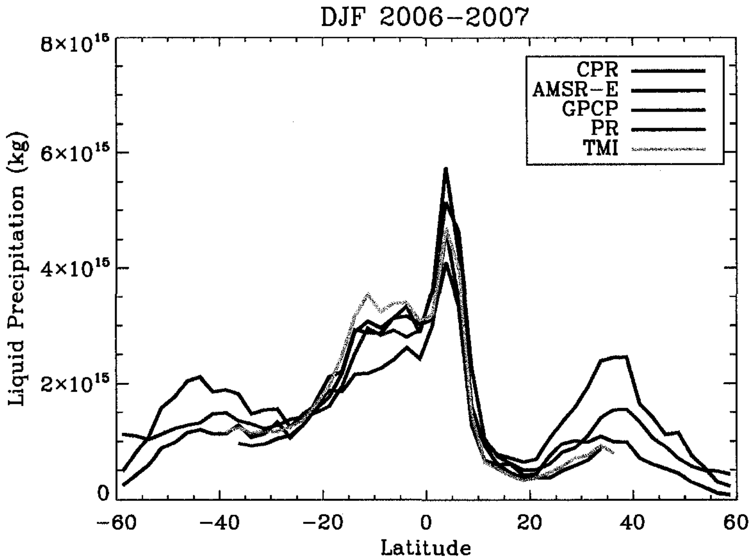

Figure 5.16: Area weighted liquid precipitation accumulation over the global oceans as a function of latitude.

became saturated (i.e. reached the MRP) 79% more frequently between −16.25° and −3.75° latitude as it did between −3.75° and 3.75° latitude. This suggests that heavy precipitation occurred more frequently in the southern branch of the ITCZ than the northern branch during this time period. While the CPR retrieval performs best at the lower end of the rainfall intensity spectrum, sensors like the PR are well suited to observe heavy rain. The synergy of combining the different types of information provided by these two instruments is again emphasized.

Transitioning into the middle latitude storm tracks, however, there is considerable variance between all estimates. CPR accumulated rainfall is considerably higher than both passive microwave and PR estimates. The source of these differences is not known, but some speculation is possible. As discussed earlier in this section, performance of the full retrieval algorithm becomes more uncertain as the freezing level lowers to 1-2 km, particularly for precipitation rates between 5 and 10 mm h^{-1}, and retrieval analysis (not shown) shows that the bulk of this precipitation occurs from cases where $R > 5$ mm h^{-1}. Therefore CloudSat estimates may be biased high. It is also known, however, that microwave precipitation estimates based on GPROF (AMSR-E and TMI) are degraded when applied outside the tropics. Unfortunately it is difficult to validate rainfall retrievals (and the effects of omnipresent uncertainties such as DSD) over the middle latitude oceans since virtually no regular *in situ* measurements of rainfall exist. It is noteworthy, however, that these uncertainties in mass of accumulated water are unrelated to the finding that the CPR observes precipitation significantly *more often* over the middle-latitude oceans, particularly during the winter season, than is indicated by passive microwave measurements. This is consistent with the findings of Petty (1997), who compared passive microwave precipitation estimates over the ocean with shipboard observations and concluded that, poleward of about 45°, the surface observations showed a significantly higher frequency of precipitation occurence than the satellite estimates.

5.1.9 Conclusions

W-band radars such as the CloudSat CPR are sensitive to both clouds and precipitation, and are particularly well suited to the discrimination of raining clouds from non-raining clouds, as well as the quantification of light to moderate precipitation. For this purpose, attenuation by hydrometeors is an advantage of W-band radars, because the magnitude of this attenuation is related to the intensity of precipitation in the atmospheric column observed by the radar. By measuring the strength of backscatter from the ocean surface and the low-level radar reflectivity, it is possible to determine, with high confidence, whether precipitation is occurring within the radar footprint. It has also been demonstrated that the radar is sensitive to precipitation rate, within the limits of saturation. Multiple scattering effects are significant for precipitation more intense than approximately 3 mm h^{-1}, and melting particle effects may also be important, particularly when precipitating ice is present. Failure to account for either of these processes results in biases in retrieved precipitation rates.

Seasonal retrieval statistics suggest that a greater amount of rain falls over the middle and high latitude oceans than has previously been detected using passive microwave techniques. It is difficult to verify these retrievals, however, due to lack of *in situ* rainfall measurements over high latitude oceans. Validation campaigns will be essential to verify the amount of rain that falls in storm tracks and establish a baseline for comparison.

Finally, it is notable that CloudSat is the first active, spaceborne observing system to regularly view rain outside the tropics. It has been demonstrated that the CPR detects light rainfall more often than the TRMM Precipitation Radar, owing primarily to the operating frequency and higher sensitivity of the CPR. The PR, in turn, quantifies heavier rain that is beyond the measurement capabilities of the CPR. This is one example of the synergy resulting from the combination of CloudSat observations with other precipitation sensors; this combination has great potential to provide new information about how precipitation is distributed on our planet.

Acknowledgments

This study was supported partially by NASA Grant #NNX07AR97G. We wish to thank Denis O' Brien of Colorado State University for providing the backward Monte Carlo model used in this study and for his assistance adapting it for use in the CloudSat configuration.

5.2 Addendum: Discrete dipole approximation calculations

As described in Chapter 5.1.5, the discrete dipole approximation (DDA) is used to represent pure ice. It is worth repeating that a surface snowfall retrieval is not attempted. In fact, when the melting layer model produces a surface melted fraction less than 0.8, no quantitative retrieval is performed so as to avoid incurring large errors from uncertainties due to particle habit and other assumptions associated with the melting layer model (such as neglecting the collision-coalescence process, assuming a constant particle concentration flux, etc.).

Guosheng Liu's database of single scatter properties for non-spherical ice crystals was obtained (Liu, 2007). The database contains scattering properties for five ice crystal habits: hexagonal columns and plates, rosettes, sector snowflakes, and dendrite snowflakes (Figure 5.17). The 6-arm bullet rosette was chosen to represent snow aggregates, since the remaining habits better represent pristine ice or individual snowflakes. Distributions of snowflakes were created according to equations (65) through (67) for a set of 21 distinct values of melted fractions, f, between 0 and 1, and the single scatter parameters were derived for these distributions as

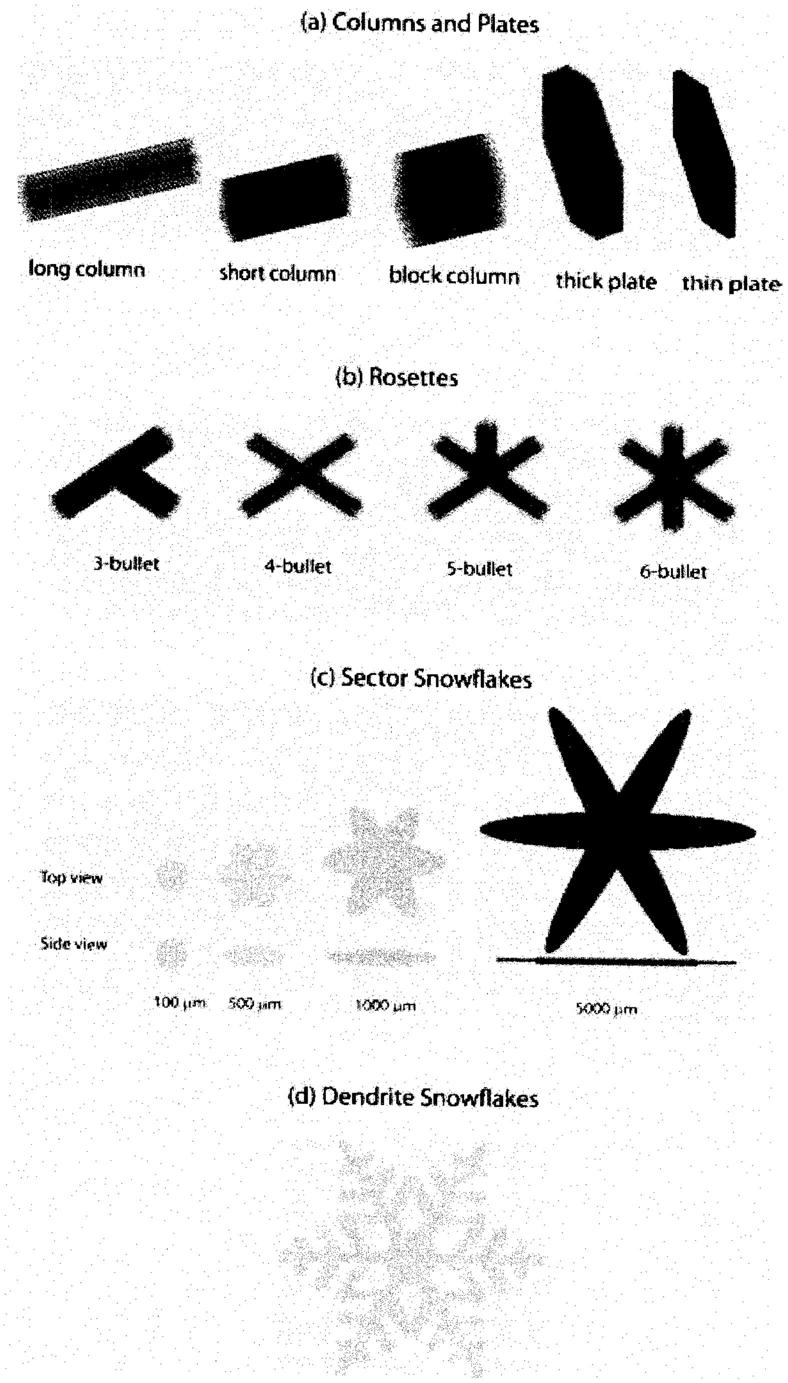

Figure 5.17: Ice crystal habits, from Liu (2007) database. Courtesy Guosheng Liu.

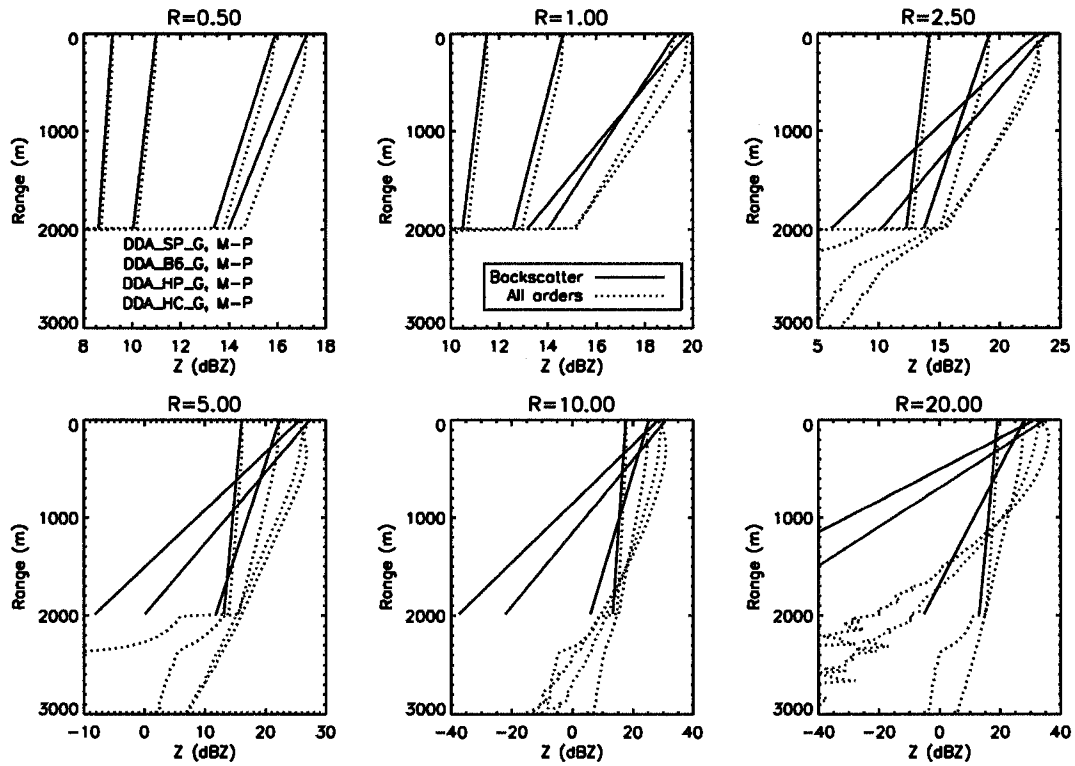

Figure 5.18: 94 GHz reflectivity profiles for a 2 km deep cloud precipitating at equivalent liquid precipitation rate R (mm h^{-1}) for a melt fraction $f = 0$. Solid lines show reflectivity due to backscatter only, dashed lines include up to 10 orders of scatter. Blue line - sector plates, green line - bullet rosettes, red line - hexagonal plates, black line - hexagonal columns.

discussed in the previous section[3].

The Monte Carlo model was then applied to these distribution-integrated scattering properties. Sample reflectivity profiles for a 2 km deep cloud ($f = 0$) raining at a variety of liquid-equivalent precipitation rates are shown in Figure 5.18. The bullet rosettes used in the operational retrieval are shown in green, other habits are indicating by the different colors. Solid lines show reflectivity due to backscatter only, and dashed lines show reflectivity due to up to 10 orders of scatter. Thus

[3]The assistance and DDA expertise provided by Norman Wood of Colorado State University was much appreciated for this task.

the difference between the solid and dashed lines of any given color is a measure of the reflectivity component due to MS. As expected, MS universally increases reflectivity over the backscatter-only component. The slope of the solid lines is the single-scatter attenuation coefficient (dB m^{-1}), and the slope of the dashed lines effectively represents a modification of the attenuation coefficient by MS. The saturation of reflectivity that occurs at W-band near 20 dBZ is also apparent.

The differences in reflectivity provided by the various habits is remarkable. At cloud top, the sector plates produce 9 dBZ of reflectivity while the hexagonal columns produce 17 dBZ. The hexagonal plates and column are also are most affected by MS, and probably to a non-physical degree. These results for plates and columns are most likely the product of application of a precipitation-type particle size distribution to what are more representative of pristine, non-precipitating ice particles. The low reflectivities of the sector plates can, at least partially, be attributed to the DDA database assumption that these crystals fall with random orientation; in reality, sector plates prefer to fall with their longest dimension parallel to the surface, and this would considerably increase their reflectivity when viewed from a top-down perspective.

The bullet rosettes provide a compromise between these two extremes. The reflectivities produced by the bullet rosettes is also supported by observations during the Canadian CloudSat/CALIPSO Validation Project (C3VP) experiment on 22 January 2007 near Egbert, Ontario. Snowfall rates of approximately 1 mm h^{-1} liquid equivalent, as measured by surface gauge, produced a peak surface reflectivity near 13 dBZ as observed by the 94 GHz Airborne Cloud Radar. The snowflakes were described as a mix of stellar dendrites and aggregates. This reflectivity measurement is within 1.5 dBZ of the DDA derived reflectivities for bullet rosettes,

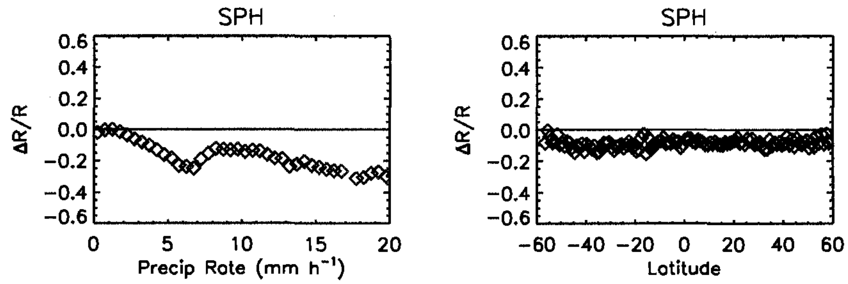

Figure 5.19: Fractional change in precipitation rate produced by assuming spheres rather than bullet rosettes (red symbols). Shown as a function of precipitation rate (left panel) and latitude (right panel).

but nearly 8 dBZ higher than the reflectivity produced by "soft spheres" (Chapter 5.1.5, not shown). It is also noteworthy that for heavier precipitation rates the MS contribution to reflectivity can extend far below the physical base of the cloud. This is consistent with the findings of Battaglia et al. (2007), and confirms that precipitating ice can produce a signature near the surface (specifically, a contribution to σ_0) even when the freezing level is relatively high.

Figure 5.19 shows the fractional change in precipitation rate obtained by assuming spherical snow rather than the hybrid of spheres and bullet rosettes used in the retrieval. This provides a quantification of the differences between the two assumptions, although it can not be stated with high certainty that one representation is better than the other for the types of scenes that CloudSat observes. Spheres produce smaller precipitation rates that the sphere/bullet rosette hybrids because, for a given precipitation rate, the distribution of spheres attenuates more than the corresponding hybrid distribution (see Figure 5.7). It is noted that the choice of ice crystal habit has a substantial effect on the retrieval only for the limited subset of cases where precipitating ice is present above the freezing level.

5.3 Addendum: The Monte Carlo model

The Monte Carlo model used for creation of the PIA lookup tables is that described by O'Brien (1992) and O'Brien (1998). Monte Carlo models provide a stochastic (i.e. brute force) solution to the radiative transfer equation (RTE). Such solutions are generally much slower than analytical solutions, and are most often used when analytic solutions are essentially impossible (for example, the multiple scattering problem with more than a few orders of scatter). Considering a scattering and absorbing medium, the RTE requires that the radiance at any point $\mathbf{x}$ in a direction given by $\mathbf{s}$ is $I(\mathbf{x}, \mathbf{s})$, given by

$$\begin{aligned} s \cdot \nabla I(\mathbf{x}, \mathbf{s}) = & -\sigma_{ext}\, I(\mathbf{x}, \mathbf{s}) \\ & + \sigma_{sca} \int_{\Omega} P(\mathbf{x}, \mathbf{s}, \mathbf{s}')\, I(\mathbf{x}, \mathbf{s})\, \mathrm{d}\Omega(\mathbf{s}') \,, \end{aligned} \tag{86}$$

where σ_{ext} and σ_{sca} are the volume extinction and scattering coefficients, respectively, P is the scattering phase function, and the integration is carried out over solid angle, Ω. The phase function is an intrinsic property of the scattering medium; $P(\mathbf{x}, \mathbf{s}, \mathbf{s}')$ represents the scattering of radiation at $\mathbf{x}$ from direction $\mathbf{s}'$ into direction $\mathbf{s}$. The radiance at any point $\mathbf{x_0}$ in direction $\mathbf{s_0}$ may be partitioned into contributions from up to n individual orders of scatter:

$$I(\mathbf{x}_0, \mathbf{s}_0) = \sum_{k=0}^{n} I_k(\mathbf{x}_0, \mathbf{s}_0) + \epsilon \,, \tag{87}$$

where the remainder, ϵ, approaches zero as n approaches infinity. The radiance transmitted directly from the boundary is

$$I_0(\mathbf{x}_0, \mathbf{s}_0) = t(\mathbf{x_0}, \mathbf{u_0}) I(\mathbf{u}_0, \mathbf{s}_0) \,, \tag{88}$$

where $\mathbf{u}_0$ is the point found by tracing $\mathbf{s}_0$ back from $\mathbf{x}_0$ to the boundary of the medium, and $t(\mathbf{x}_0, \mathbf{u}_0)$ is the transmission between $\mathbf{x}_0$ and $\mathbf{u}_0$. If kth order scattering occurs at point $\mathbf{x}_k$, where radiation enters direction $\mathbf{s}_{k-1}$ from $\mathbf{s}_k$ (which can be traced back through the previous scattering point to boundary point $\mathbf{u}_k$), then the radiance contribution from any order of scattered radiation can be written

$$\begin{aligned}I_k(\mathbf{x}_0, \mathbf{s}_0) = &\int_{\mathbf{u}_0}^{\mathbf{x}_0} t(\mathbf{x}_0, \mathbf{x}_1)\,\mathrm{d}\mathbf{x}_1\,\sigma_{sca}(\mathbf{x}_1) \int_\Omega P(\mathbf{x}_1, \mathbf{s}_0, \mathbf{s}_1)\,\mathrm{d}\Omega(\mathbf{s}_1) \\ &\ldots \int_{\mathbf{u}_{k-1}}^{\mathbf{x}_{k-1}} t(\mathbf{x}_{k-1}, \mathbf{x}_k)\,\mathrm{d}\mathbf{x}_k\,\sigma_{sca}(\mathbf{x}_k) \int_\Omega P(\mathbf{x}_1, \mathbf{s}_0, \mathbf{s}_1) t(\mathbf{x}_k, \mathbf{u}_k) I(\mathbf{u}_k, \mathbf{s}_k)\,\mathrm{d}\Omega(\mathbf{s}_1)\,.\end{aligned} \tag{89}$$

Thus, determination of the radiance from the kth order of scatter requires evaluation of a $3k$ dimensional integral (one line integral and one integral each over azimuth and zenith angle for each scattering event).

O'Brien (1992) shows that these integrals can be transformed into unit integrals over a $3k$ dimensional hypercube,

$$I_k(\mathbf{x}_0, \mathbf{s}_0) = \int q_k(\mathbf{z})\,\mathrm{d}\mathbf{z} \tag{90}$$

where the points $\mathbf{z}$ compose a vector of k sets of three variables each. The first variable represents the spatial location of a given scattering event, while the last two represent the azimuth and zenith angles associated with the scatter. The quantity q provides a weighting by the optical properties of the medium (single scatter albedo, phase function, and extinction) and boundary radiances. The points z may be chosen from random numbers in the interval [0,1], but in the O'Brien model Halton points (Halton and Smith, 1964) are utilized to more evenly sample the hypercube domain and hasten convergence of the scattering series.

Since the model does not strictly use random point distributions to select photon paths, it is more properly designated a "quasi Monte Carlo" model.

For backward Monte Carlo modeling, photons with paths determined by z are followed backward from the detector toward the transmitting antenna, for up to 10 scattering events. This is considerably more efficient than firing photos forward in time from the transmitter, since the vast majority of these photons will never encounter the detector (they will either be absorbed within the medium or at the surface, or be scattered out of the field of view without returning). Backward Monte Carlo modeling greatly reduces the number of photon packets which must be fired and averaged to develop a stable radiance solution.

For this study, 40 salvos of 50,000 photons are fired to calculate any given dimension of a single PIA lookup table. This provides excellent convergence for all but the optically thickest cases, and curve fitting is used to estimate values where convergence does not occur (see Appendix A). To generate one complete lookup table (with 556 height dimensions representing various combinations of precipitation layer depth and freezing level height, and 83 discrete precipitation rates) therefore involves tracing approximately 92.3 billion photons through a medium with height-varying optical properties. Not surprisingly, this is a computationally intensive task; the generation of one lookup table takes approximately 48 hours running on a 14 node cluster, each node utilizing a 3.06 GHz processor.

5.4 Addendum: The relationship between apparent PIA and precipitation rate

The lookup tables generated from the Monte Carlo simulations as described in Chapter 5.1.6 are represented graphically in Appendix A for the specific case of

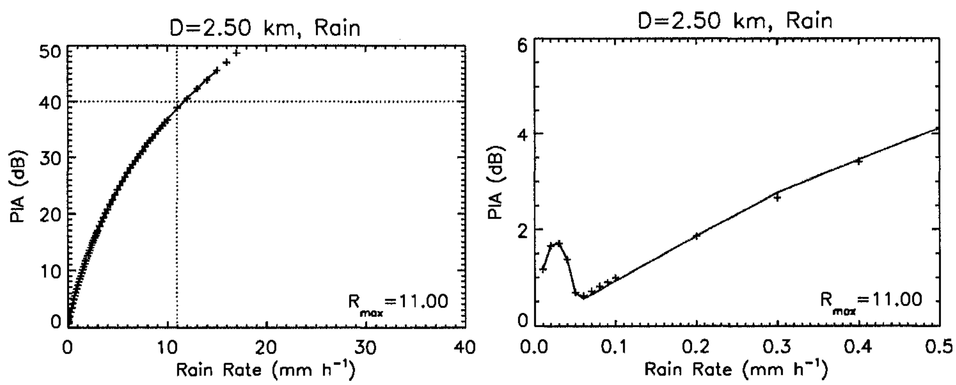

Figure 5.20: The relationship between precipitation rate and apparent PIA for a precipitating layer of depth 2.5 km. The right figure is a blowup of the left for small rain rates. The + symbols are derived from the Monte Carlo output, the solid line is the fitted curve.

$\Gamma = 3$ K km^{-1}. This relationship has already been discussed in a cursory manner for pure rain, but some additional comments are now provided that were omitted from the journal article forming the first section of this chapter. The discussion will also be expanded to include precipitating ice.

First, consider the relationship between rain rate and apparent PIA for pure rain. Figure 5.20 illustrates this relationship for a 2.5 km deep raining layer. Note that in the left panel of this figure it appears that apparent PIA always increases with rain rate. This is, in fact, universally true for any choice of rain layer depth, but only for $R > 0.05$ mm h^{-1}. The right panel provides an expanded view of the small rain rate regime, and clearly demonstrates that a turnover occurs in the R versus PIA relationship for very small values of R. The reason for this turnover is a discontinuity in the assumed cloud to rain water content ratio (CWC/RWC). Recall that this ratio is taken to be the mean derived from the GPROF database for any given value of R. The fit, which is shown graphically in Figure 5.5, takes

Coefficient	Value
a_0	23.376
a_1	−610.80255
a_2	32.48402
a_3	0.52708
a_4	−0.18569
a_5	0.02438

Table 5.3: Values used in the CWC/RWC ratio.

the following form:

$$\mathrm{CWC/RWC} = \begin{cases} a_0 & R < 0.01 \\ a_1 R + a_2 & 0.01 \le R < 0.05 \\ a_3 R^{a_4} \exp(-a_5 R) & R \ge 0.05 \end{cases} \tag{91}$$

with R in mm h^{-1} and coefficient values defined in Table 5.3.

When a multi-valued solution for R is encountered (i.e. the observed PIA matches multiple values of R in the table), two steps are taken. First, the precipitation rate is reported as the mean of the smallest and largest matching values of R. Second, the retrieval is flagged so that users of the product are aware of the enhanced uncertainty. An additional warning of this uncertainty is provided to the user through the reported minimum and maximum precipitation rate, R_{low} and R_{high}, which result from perturbing the measurement uncertainty (i.e. the PIA) by one standard deviation in each direction. For the case of pure rain, this uncertainty is associated only with the lightest detectable rain, and is usually very small.

When precipitating ice is present in the column, the turnover in the PIA versus R relationship can be dramatic. Consider a 4.5 km deep cloud, and let the freezing level vary between three different heights within the cloud: 0.75, 2.5, and 3.75 km (Figure 5.21). For a freezing level of 2.5 km (top right panel), apparent PIA becomes nearly invariant with rain rate between approximately 3 and 10 mm h^{-1}, and turns over at the position of the dashed horizontal line. This turnover is the result of the competing effects of MS and PIA. When the freezing level is high, PIA in the rain dominates, and when the freezing level is low, MS in the ice dominates. Similarly, PIA dominates MS for smaller precipitation rates, but MS becomes large at higher precipitation rates. In the middle ground between these two extremes, the attenuation and MS nearly cancel each other's effects on PIA. This turnover is dealt with in the same manner as that caused by the CWC/RWC ratio at small precipitation rates. It is part of the reason that uncertainties in retrieved precipitation rate are largest for $5 < R < 10$ mm h^{-1}.

5.5 Addendum: Uncertainty analysis

The uncertainty analysis presented in Chapter 5.1.7 summarizes where errors in retrieved precipitation rate are expected to be largest, namely those locations where freezing level heights are low and precipitation rates are light to moderate. It is instructive to break down these uncertainties further, specifically in terms of the individual perturbations and the type of retrieval performed.

Figure 5.22 shows the fractional uncertainty in retrieved precipitation rate as a function of R. Black symbols designate rain-only retrievals, red symbols indicate significant precipitating ice was present, and green symbols indicates rain retrievals without significant precipitating ice (i.e. snow begins falling at the freezing level and immediately begins to melt). Individual perturbations, described originally in 5.1.7, are summarized below.

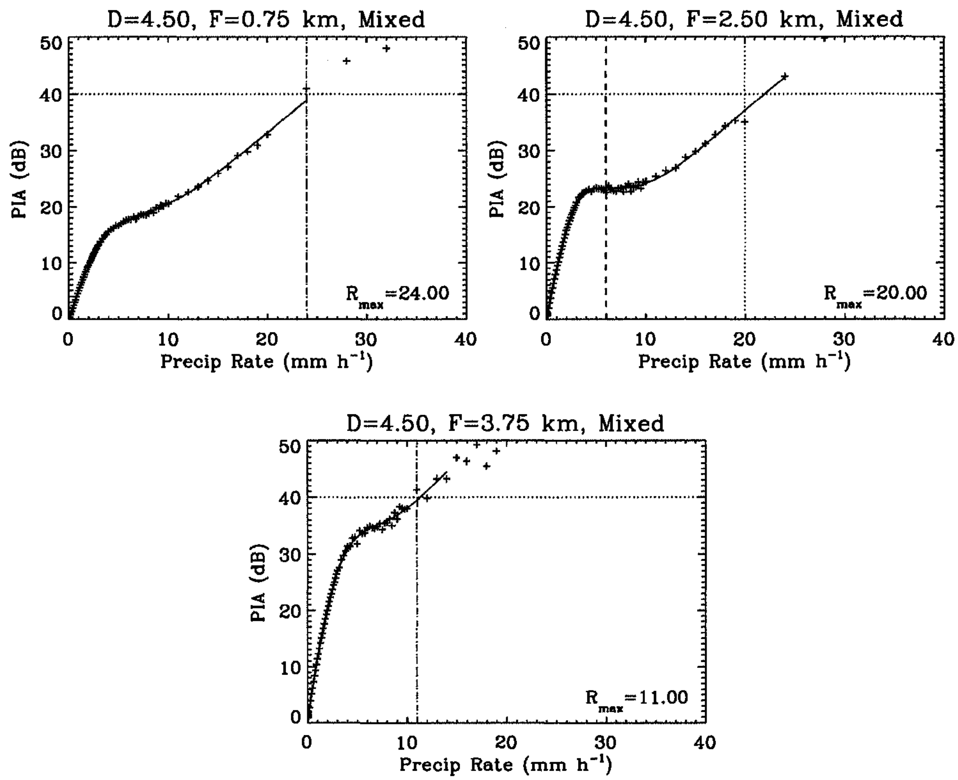

Figure 5.21: The relationship between precipitation rate and apparent PIA for a precipitating layer of depth 4.5 km, with a freezing level height varying from 0.75 to 3.75 km. The + symbols are derived from the Monte Carlo output, the solid line is the fitted curve.

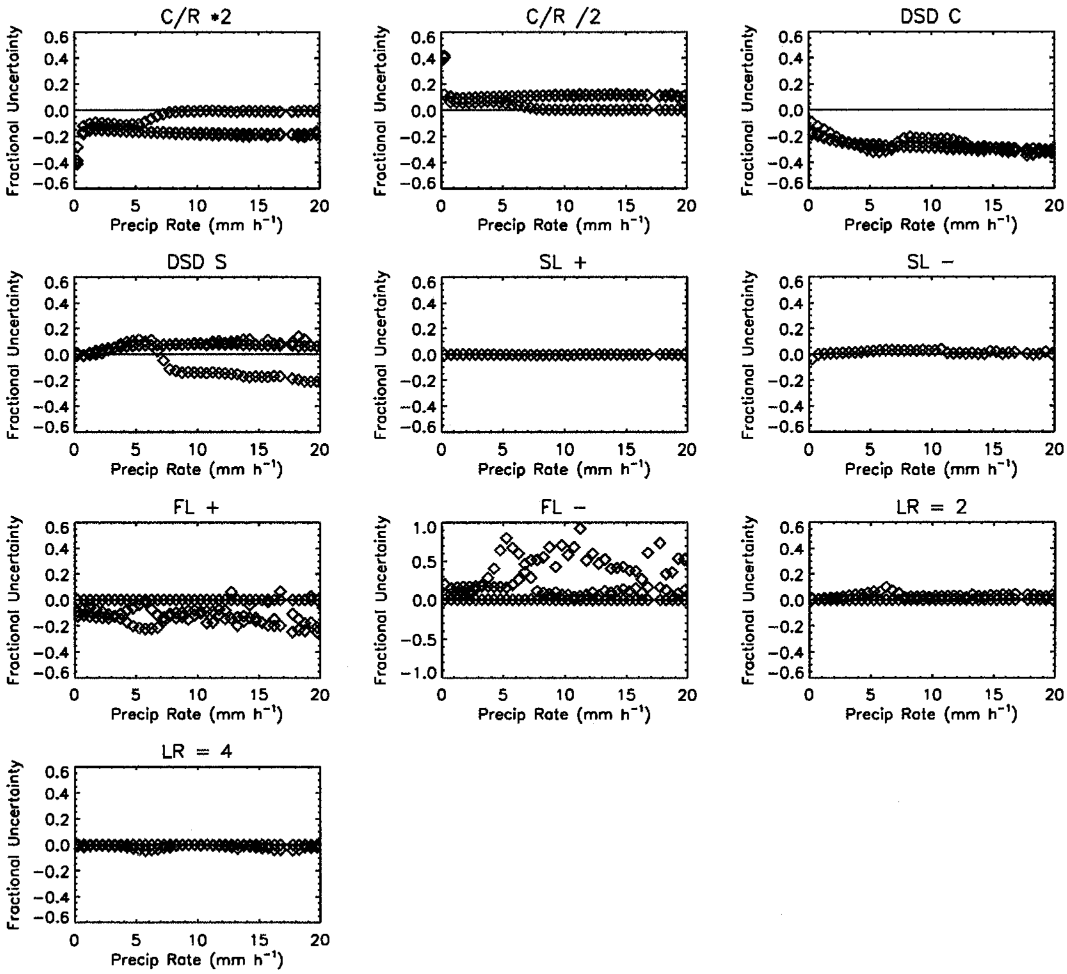

Figure 5.22: Fractional uncertainty in retrieved precipitation rate as a function of R. Black symbols - rain only retrievals, red symbols - retrievals with significant precipitating ice, green symbols - rain with no significant precipitating ice. See text for description of perturbations.

- (C/R *2) and (C/R /2) represent the CWC/RWC multiplied by and divided by two, respectively. Uncertainties are largest for small R for two reasons; first, the fraction of PIA attributed to cloud rather than rain is largest in this regime, and second, due to the turnover in the PIA versus R relationship discussed in the last section. Assuming a larger (smaller) CWC/RWC ratio produces a smaller (larger) R.

- (*DSD C*) and (*DSD S*) represent the TRMM convective and stratiform DSD's, respectively. Uncertainties are largest for the convective DSD, but still in the range of 30 to 40%.

- (*SL* +) and (*SL* −) are the perturbations in the slope of the raining column with height by −0.15 km^{-1} and 0.03 km^{-1}, normalized by the mean rain rate. There is virtually no effect on the mean rain rate that is retrieved. However, the fact that the mean rain rate now differs from the surface rain rate in a way that depends on the height of the raining column *does* produce significant error in the surface rain rate, and this is reflected in Figure 5.12.

- (*FL* +) and (*FL* −) are the perturbations in the freezing level height by plus and minus 250 m, respectively. Overestimation (underestimation) of the freezing level leads to low (high) retrieved precipitation rates. This particularly uncertainty is not symmetric; underestimation of the freezing level produces greater errors than overestimation. This result reflects the fact that a unit change in apparent PIA is associated with a larger change in R when the column is relatively shallow than when it is relatively deep. It is also interesting to note that the largest uncertainties transfer from precipitating ice retrievals to non-precipitating ice retrievals at about 5 mm h^{-1} in the case of the $FL-$ perturbation. This is a associated with the upper end of those precipitation rates that exhibit the "overturning regime" discussed in the last section.

- $(LR = 2)$ and $(LR = 4)$ represent the perturbations in lapse rate by plus and minus 1 K km^{-1}, respectively. These uncertainties are uniformly small, but tend to be largest for lower freezing levels, as shown in Figure 5.12.

These uncertainties may be expressed in terms of latitude to gain a better physical understanding of how they vary zonally. All uncertainties except those due to the freezing level are more-or-less uniform with latitude. Uncertainties associated with the freezing level have the greatest consequence at higher latitudes.

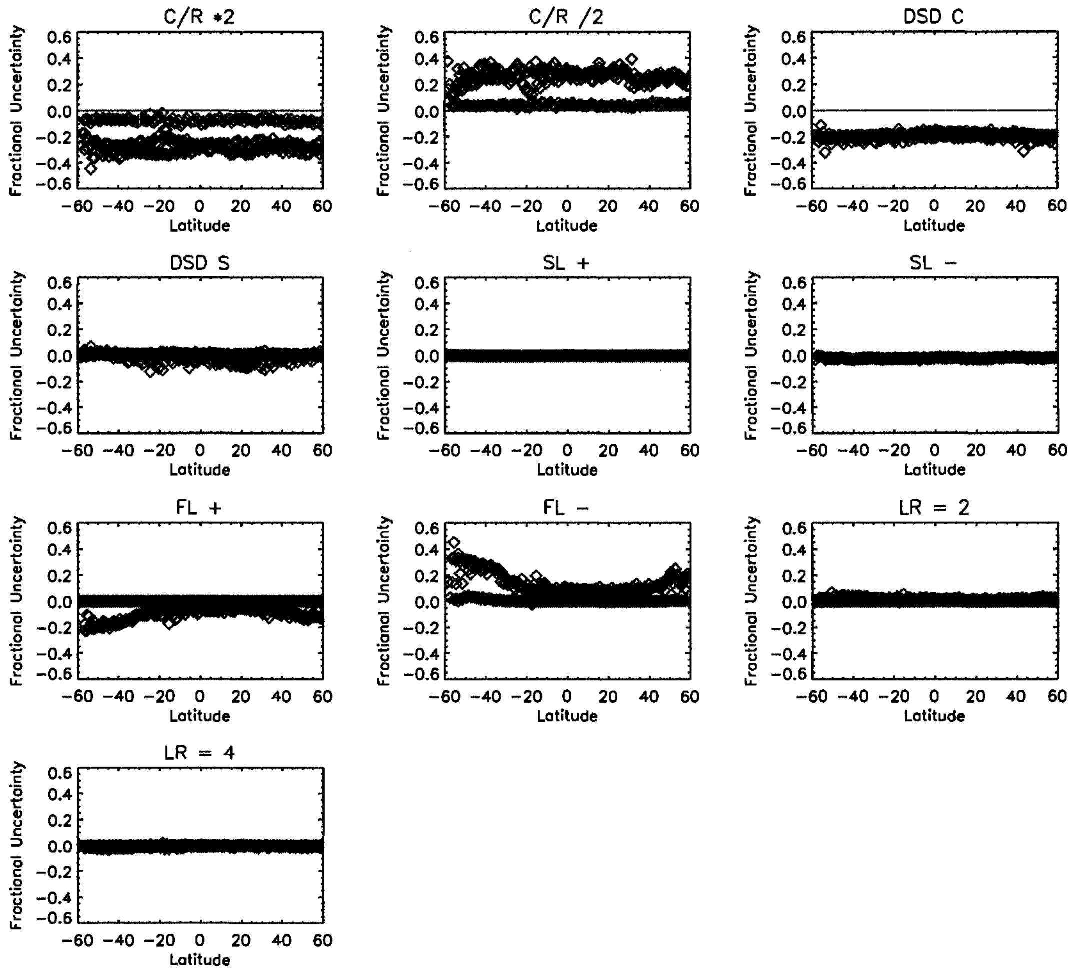

Figure 5.23: As in Figure 5.22, but fractional uncertainties in precipitation rate are expressed as a function of latitude.

6 Near-global precipitation patterns from CloudSat and their associated cloud structures

We will now take an in-depth look at some additional cloud and precipitation occurrence and accumulation statistics derived from the new CloudSat precipitation algorithm. Statistics and comparisons with other precipitation sensors have already been presented in the article that forms the first part of Chapter 5, and will not be repeated here unless additional comment is needed.

6.1 Seasonal precipitation accumulations from the CPR

The total precipitated water mass detected by CloudSat over an area A on the Earth's surface accumulated over a time period Δt is given by

$$P_{tot} = \sum_{i=1}^{n} (R_i) \cdot \frac{\rho_w \, A \, \Delta t}{n} \,, \tag{92}$$

where n instantaneous rain rate observations (including zeros) are taken, and ρ_w is the density of liquid water. The mean rain rate is simply

$$\bar{R} = \sum_{i=1}^{n} \frac{R_i}{n} \,. \tag{93}$$

This formulation requires that n and Δt be large enough to produce a representative sampling of rainfall occurring over the area. In the results presented in this section, gridded maps are shown at 2.5° latitude × 2.5° longitude resolution over a time period of at least three months. Zonal rain accumulations are created over 2.5° latitude bands. Only surface liquid rainfall accumulations are considered (retrievals for which CloudSat are most reliable), so statistics poleward of 60° latitude are excluded from these analyses.

The fraction of accumulated ocean rainfall observed by CloudSat due to each of these intensity regimes (($<$ 1 mm h^{-1}, between 1 and 5 mm h^{-1}, and greater than 5 mm h^{-1})) is shown in Figure 6.1. This figure demonstrates three basic principles. First, there are areas of the planet where light precipitation ($<$ 1 mm h^{-1}) produces significant proportions of the total seasonal rainfall, and these are the generally the stratus-dominated regions. Here, 40 to 60% of the total rainfall observed by the CPR occurs in this light precipitation mode. Second, moderate rainfall (between 1 and 5 mm h^{-1}) is common virtually everywhere, particularly so in the storm tracks of the higher latitudes. The stormy area near 60° south latitude is dominated by this moderate (and frequent, see chapter 4) rainfall during both seasons. Finally, rainfall heavier than 5 mm h^{-1} is most common along the ITCZ, in the Indian and western Pacific basins, and in the storm tracks of the mid-latitudes during the winter season. Regional statistics for a full year are presented in Table 6.1. It is noted that light precipitation, for which CloudSat is particularly well suited to observe, accounts for a sizable fraction of the tropics-wide precipitation observed by the CPR.

The problem of relating CPR-observed rainfall accumulations to those that occur in nature is problematic at best. Although the CPR is more sensitive to

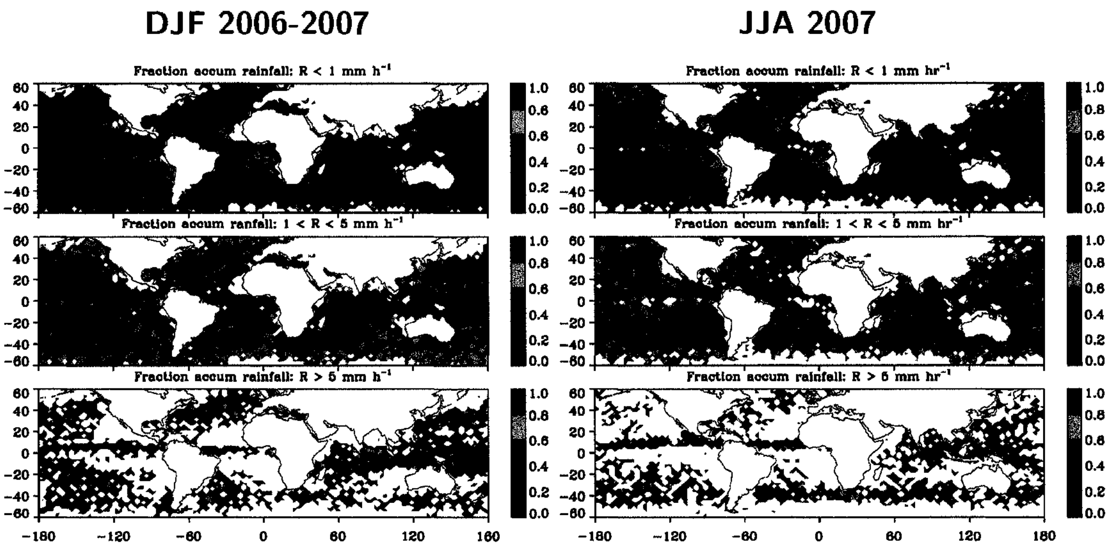

Figure 6.1: The fraction of CPR total precipitation accumulation from precipitation rates less than 1 mm h^{-1} (top panels), between 1 and 5 mm h^{-1} (middle panels), and greater than 5 mm h^{-1} (bottom panels). Left panels, DJF 2006-2007; right panels, JJA 2007. For any given grid box, the sum of the three fractions is unity.

light rain than other spaceborne sensors, it is also unable to quantify rain rates above a known threshold that depends on precipitating layer depth and freezing level height (see Figure 5.11 and the associated discussion). This skews the total accumulated precipitation mass that falls over any given region of the planet in a non-uniform way. Figure 6.2 shows the fraction of total CPR precipitating observations where the maximum precipitation rate (MPR) was encountered (and thus reported). The area weighted mean of this value equatorward of 60° latitude

	Tropics	Indian	WestPac	EastPac	Atlantic
R $<$ 1 mm h^{-1}	0.17	0.14	0.14	0.19	0.17
1 $\leq$ R $<$ 5 mm h^{-1}	0.40	0.35	0.38	0.43	0.38
R $\geq$ 5 mm h^{-1}	0.43	0.50	0.48	0.38	0.45

Table 6.1: Fractional CPR precipitation accumulation for September 2006 through August 2007 in the four geographic regions defined in Figure 4.2.

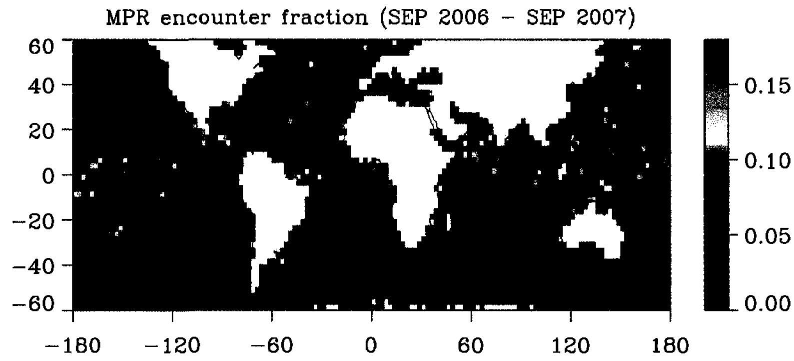

Figure 6.2: The fraction of CPR precipitating observations where the maximum precipitation rate is encountered for September 2006 through August 2007.

is relatively small (0.03), but in certain regions where relatively heavy precipitation cores are common it averages approximately 0.05 to 0.08 (the western Pacific and much of the Indian Ocean basin, for example).

TRMM provides the most authoritative estimate of the total mass of rain water that falls in the tropics. For the September 2006 through August 2007 period, the TRMM PR estimated the mean oceanic rain rate for 20°N to 20°S latitude was 3.12 mm day^{-1}, and the TMI estimate was 3.21 mm day^{-1}. The concurrent CPR estimated precipitation rate was 2.61 mm day^{-1}, or 81 to 84% of the TRMM estimates. With a full year of observations, sampling issues are probably not responsible for this mismatch.

The reasons for the differences between CPR, TRMM, and nature's total rainfall accumulations are thusly convoluted and difficult to separate. First, in those areas where the CPR regularly underestimates the higher precipitation rates, this effect will tend to exaggerate the relative contribution of lighter rain to the seasonal total. This is not expected to be a significant factor in the East Pacific and Atlantic regions, but is of relatively greater importance in the Indian and western Pacific regions. Second, the CPR does not detect rainfall below 1 km. This produces a compensating effect, i.e. it deflates the importance of light rainfall to the seasonal totals. This compensating effect is not, however, expected to be as significant as the former. Third, the TRMM PR and TMI statistics are skewed toward heavier rainfall rates. The PR is unable to detect rain rates less than approximately 0.5 to 0.7 mm h^{-1} because of lack of radar sensitivity to the smallest of precipitation particles, and the TMI may mis-classify low liquid water path events that are seen by the CPR as non-precipitating.

Although the crossover matches described in Chapter 5.1.8 provide some insight into how one may resolve the rain rate dependent precipitation occurrence differences between the CPR and PR, a better solution is to consider each instrument at its native resolution. For this purpose, the TRMM 2A25 data was obtained for the DJF 2006-2007 period and precipitation accumulations and mean rate (using the near surface rain field) were calculated between 20°N to 20°S latitude from equations (92) and (93). Similar analysis was performed for the TRMM TMI (2A12 data) and AMSR-E for reference. The resulting histogram is shown in Figure 6.3, and the mean rain rates are given in Table 6.2. It is noted that the CPR values reported here differ from those in Table 6.1 by a few percent because lidar data availability was not required for this calculation.

For this particular period, both instruments observe similar mean rain rates, but the associated distributions of rain intensity differ greatly. While the CPR derives 16% of the tropical rainfall from rain lighter than 1 mm h^{-1}, the PR derives 6%, such that the CPR accumulates 2.5 times the precipitation mass of the PR in this category. At the heavier end of the spectrum, the PR derives 60% of rainfall from rain more intense than 5 mm h^{-1} while the CPR derives only 45%, such that the CPR accumulates about 72% the precipitation mass of the PR in

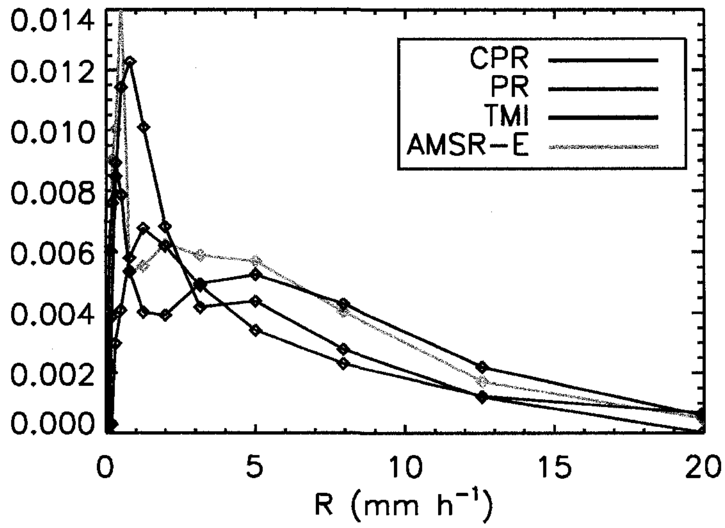

Figure 6.3: Histogram of frequency of occurrence of precipitation normalized by total number of observations for the CPR, TRMM PR and TMI, and AMSR-E at their native resolutions. For observations between 20°N and 20°S latitude, DJF 2006-2007. Bin size increases with R, as shown by the diamond symbols.

Category	R < 1	1 ≤ R < 5	R ≥ 5	Total
TRMM PR	0.188 (0.06)	1.071 (0.34)	1.864 (0.60)	3.128 (1.00)
CPR	0.469 (0.16)	1.204 (0.40)	1.346 (0.45)	3.019 (1.00)
CPR corrected	0.469 (0.14)	1.138 (0.33)	1.864 (0.54)	3.471 (1.00)
CPR/PR	2.49	1.12	0.72	0.97

Table 6.2: Top three rows: Contribution of the given rain categories (mm h^{-1}) to the derived mean rain rate (mm day^{-1}) for DJF 2006-2007, 20° north and 20° south latitude. Numbers in parenthesis are the fractional contribution to the total. The "CPR corrected" category is defined in the text. Bottom row: The ratio of CPR to PR accumulated precipitation.

this category. The precipitation falling from rain with intermediate intensities is similar for both instruments.

Taking the TRMM-observed rainfall accumulated over 5 mm h^{-1} and the CPR-observed rainfall accumulated under 1 mm h^{-1} to be "truth," and using the sensor mean for the intermediate rain category, is is possible to grossly estimate the bias in rainfall accumulation caused by underestimation of heavy rain by CloudSat (the "CPR corrected" category in Table 6.2). This correction leaves the contribution from light rain the same, while decreasing the contribution of moderate rain by about 5% and increasing the contribution of heavy rain by a more substantial 38%. By contrast, the contribution of each rain rate category as a *fraction of the total assumed accumulation* changes by less than 0.1 for each category. This analysis provides a rough estimate of the uncertainty on the fractional accumulations discussed due to attenuation of the CPR in heavy rain.

Finally, it is noteworthy that between 3 and 7 mm h^{-1}, CPR rain rates typically exhibit a local increase in occurrence relative to surrounding values (e.g. the bump visible in Figure 6.3) when accumulated over a long enough period of time. This is associated with activation of the branch of the retrieval that allows precipitating ice to contribute to PIA, which only occurs when significant radar echo is present above the freezing level. As discussed in Chapter 5.4, multiple scattering can lead to a multi-valued solution for precipitation rate in this moderate rain rate regime, and the resulting averaging produces the "bump" effect seen in the figure. The analysis presented in Chapter 5.1.7 describes this effect and quantifies the uncertainties associated with it.

6.2 Precipitation accumulation by cloud height

This section deals further with the question of how precipitating cloud systems are structured in the atmosphere, specifically with regard to how much precipitation falls from clouds with different heights. The location of clouds and intensity of precipitation is directly connected with how much latent heat is released into the atmosphere, and where the heating occurs vertically. This is, in turn, critical to storm dynamics, gravity wave dispersion, and the organization of mesoscale convective systems (e.g. Gill (1980), Johnson and Young (1983), Lin and Johnson (1996) and others). A classical view of the heating from convective and stratiform regions areas is shown in Figure 6.4. While the convective elements of storms are usually taken to contain strong updrafts with the bulk of latent heat released in the middle troposphere, stratiform areas are characterized by more gentle ascent, a higher altitude latent heating peak, and cooling near the surface resulting from evaporation and snow melt (Johnson, 1986). CloudSat, together with CALIPSO, has provided the most complete view of the three-dimensional structure of clouds on Earth to date. When combined with precipitation information, useful new knowledge may be obtained about the structure of those cloud elements that are actually producing precipitation, separate from overlying cloud layers that are

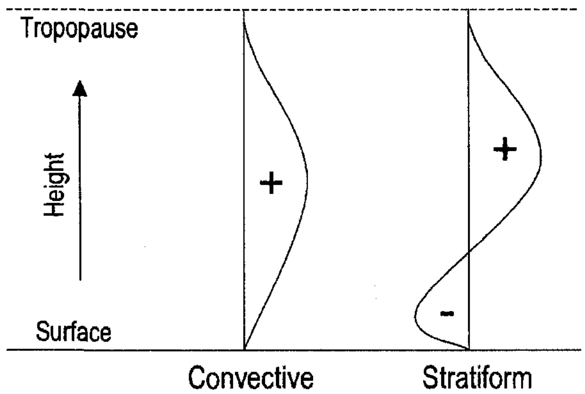

Figure 6.4: Classical view of convective and stratiform heating profiles. "+" indicates heating, "−" indicates cooling.

physically removed from the precipitation process. This is a great strength of active, profiling sensors.

To this end, seasonal CloudSat rain accumulations are subdivided by cloud height regime according to the CTL and CTH. These results are show in Figures 6.5 and 6.6. As expected, the regions favoring precipitation less than 1 mm h^{-1} generally correspond well to regions favoring low CTL's. CTL's between 4.75 and 11 km are favored in the middle latitude storm tracks, but are also common along the ITCZ. Deep convection is marked by regions with the CTL frequently greater than 11 km, and is most common in the Indian Ocean and western Pacific. It is also very common, however, in the southeastern Pacific between 20 and 40° S latitude during the southern hemisphere summer, and in the south Atlantic Ocean basin off the coast of Brazil. The latter feature was also observed from ship observations by Petty (1995), who associated this feature with moist equatorial flow over the relatively cool sea surface. Contrasting this against fractional rain accumulation grouped by CTH hints, again, at the prevalence of multiple layered (ML) systems and their relative importance not only in terms of precipitation incidence,

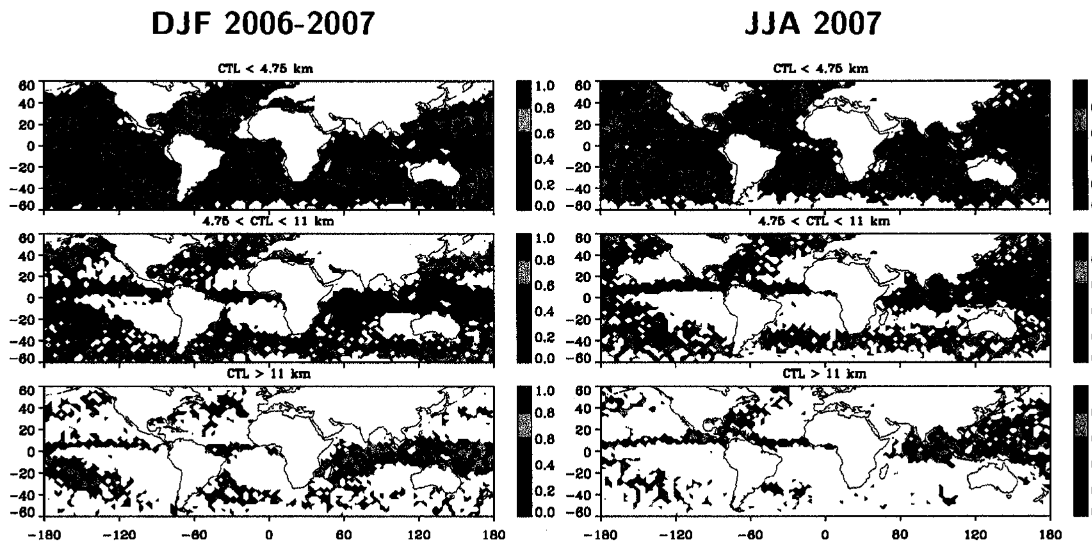

Figure 6.5: The fraction of total CPR precipitation accumulation grouped by the cloud top height of the lowest layer (CTL). Left panels, DJF 2006-2007; right panels, JJA 2007. For any given grid box, the sum of the three fractions is unity.

but total accumulated water as well. For example, nearly all the seasonally accumulated rainfall in the Indian and western Pacific basins occurs with cloud present above 11 km, but the portion of the cloud physically tied with active precipitation microphysics, characterized here by the CTL, is often lower in the atmosphere.

The zonal distribution of CPR precipitated mass as a function of cloud top (Figures 6.7 and 6.8) also demonstrates this phenomenon. The top panels of each figure show precipitation distribution by CTL. The ascending branch of the Hadley cell associated with convection on the ITCZ is apparent, as are the descending regions of subsidence in the subtropics where most precipitation falls from low-topped clouds (the stratus regime), and storm activity in the middle latitude storm tracks.

In the vicinity of the ITCZ there are two distinct cloud structures associated with the bulk of the accumulated precipitation. The first are deep clouds extending

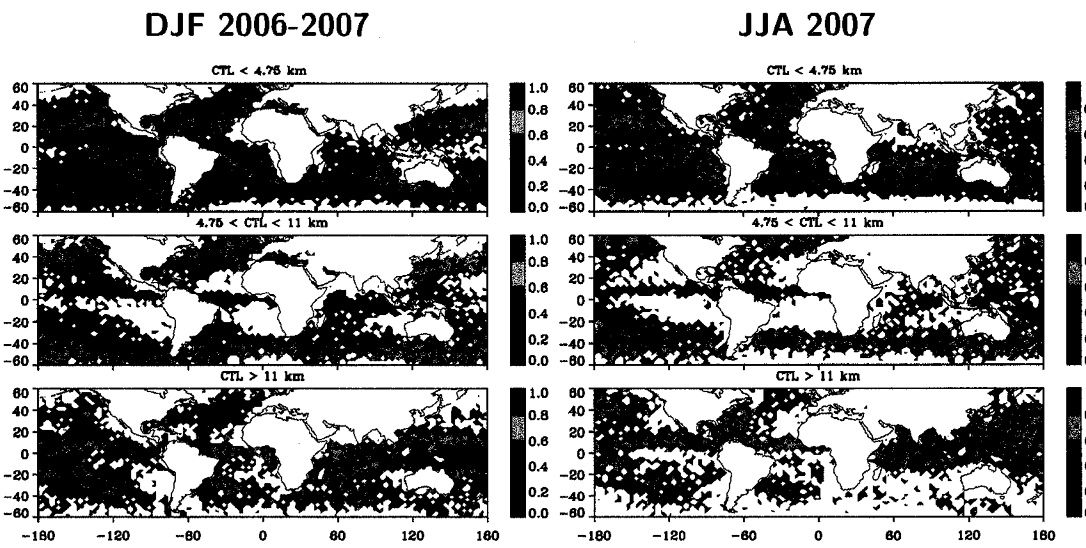

Figure 6.6: As in Figure 6.5 but for cloud top height of the highest layer (CTH).

up to the tropical tropopause near 15 km. The others are low and middle topped clouds extending to anywhere between 3 and 9 km. To the south of the main ITCZ during DJF 2006-2007, the distribution of precipitation-producing clouds is quite different; here the deep mode alone produces the bulk of the surface precipitation. In the middle latitudes, the storm tracks are extremely active, particularly in the winter hemisphere. A bimodal CTL mode is notable between 35 and 50° north during the winter; this is the synthesis of stratus contributions and deeper, heavier precipitating systems in the storm tracks.

The prevalence of ML clouds is again suggested by the differences between CTL and CTH. This is quantified further in Figure 6.9, which reviews the zonal distribution of ML cloud systems and shows the total CPR accumulated precipitation mass due to ML clouds. In the ITCZ, approximately 60% of all precipitation mass retrieved from CloudSat originates from clouds with multiple layers. This percentage is a minimum at 20-40% in the subsidence zones of the subtropics, and about 30-40% in the middle latitudes. Precipitation from ML clouds is further

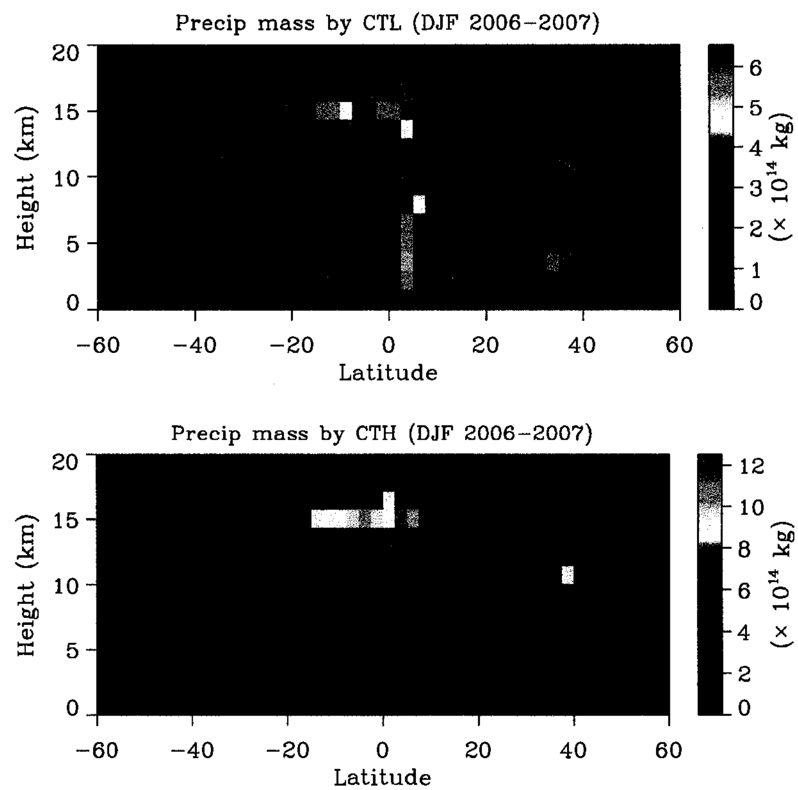

Figure 6.7: Zonal distribution of CPR accumulated precipitation mass as a function of CTL (top panel) and CTH (bottom panel). For DJF 2006-2007.

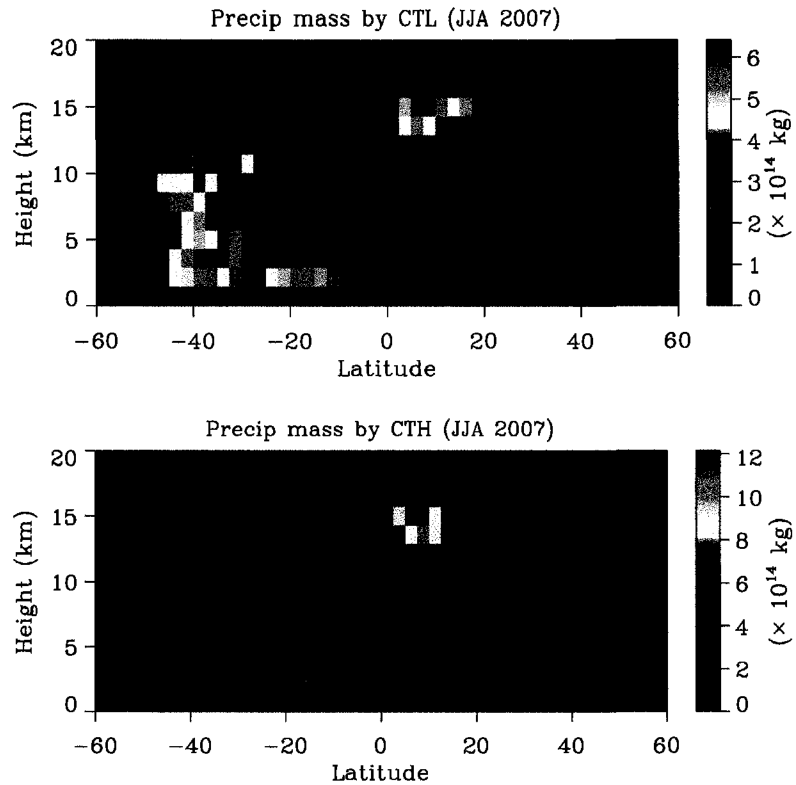

Figure 6.8: As in Figure 6.7, but for JJA 2007.

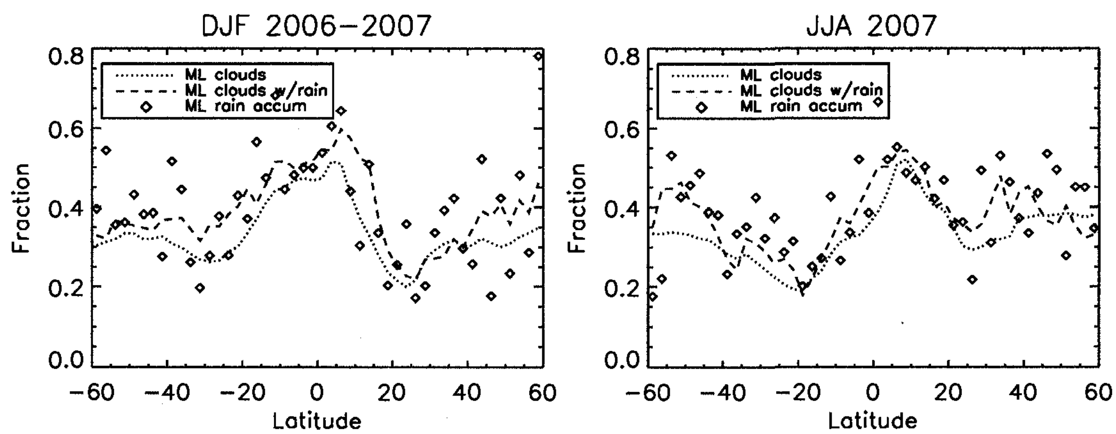

Figure 6.9: Seasonal distribution of the fraction of CPR-observed cloudy columns that have multiple layers (dotted line), fraction of multiple layer cloud systems that produce rain (dashed line), and fractional CPR rainfall accumulation due to multiple layered cloud systems (diamond symbols).

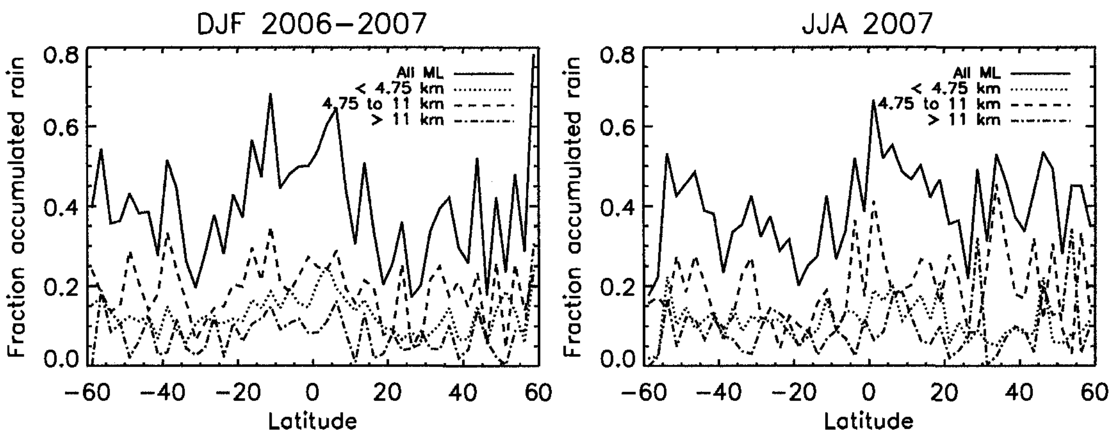

Figure 6.10: Zonal distribution of CPR fractional accumulated rain water due to cloudy scenes with multiple layers and CTL less than 4.75 km (dotted line), between 4.75 and 11 km (dashed line), and greater than 11 km (dash-dot line).

broken down by CTL of the component layers in Figure 6.10, which shows that scenes where the CTL of ML clouds exceeds 11 km are relatively rare (generally less than 20% of all cases); in fact, CTL is almost equally distributed between low, middle, and high topped clouds. Therefore the ML systems shown in Figure 6.10 are *not* simply composed of deep convection with tenuous separated cirrus layers on top.

6.3 Summary

CloudSat rainfall accumulations are not as easy to interpret as are precipitation occurrence statistics. Comparison with TRMM observations over identical areas and time periods suggest that although CloudSat does not capture the heaviest precipitation events, it captures more light rain events. Due to known retrieval biases, the resulting breakdown of total rainfall accumulation into fractional contributions from light, moderate, and heavy precipitation (as defined earlier) must be reduced slightly for light rain and increased for heavy rain. Even with this bias, it is found that a substantial fraction of tropical rainfall falls from cloud layers with CTL's below the freezing level (approximately 4.75 km.)

Cloud systems with multiple layers dominate the CPR-observed precipitation that falls in the tropics. Even given CloudSat rainfall biases discussed in the previous section, it is none-the-less certain that ML cloud systems have a significant contribution to rainfall over the global oceans. It is cautioned that passive spaceborne sensors may, at times, be unable to resolve the vertical structure of such systems, and attribute the observed rainfall to a continuous, deep structure. The extent to which the "deep model" of tropical precipitation, demonstrated by the latent heating profiles shown in Figure 6.4, is represented by these new observations is beyond the scope of this study. It appears, however, that a lower mode of latent heat release may be much more common in the tropical atmosphere than previously quantified.

Example CloudSat cross sections demonstrating precipitating falling from both the deep mode (Figure 6.11) and multi-layer mode (Figure 6.12) are provided. In both cases, a bright band is present marking the freezing level near 5 km. In the deep mode example, tropopause penetrating convection with overlying cirrus is present. In the left third of the figure, most precipitation is falling from this deep mode. In the middle third of the figure, convection penetrates through the melting level but does not reach the tropopause; overlying cirrus associated with the deep convective element qualifies this area as multi-layer. On the far right of the figure, congestus is seen in the incipient stages of precipitation formation. In the second example, precipitation falls dominantly from low cloud with overlying cirrus of various thickness in the first and last thirds of the figure.

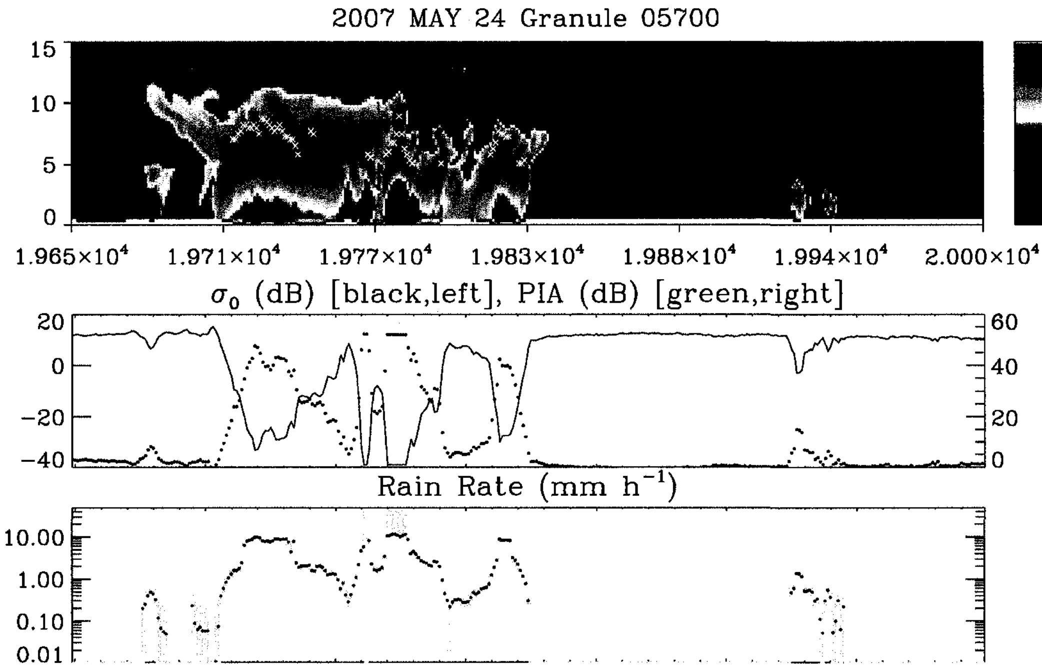

Figure 6.11: Example retrieval showing deep convection as the dominant precipitation mode. Top panel - CPR reflectivity between 0 and 15 km, yellow X's indicate assumed frozen precipitation height. Middle panel - σ_0 and PIA. Bottom panel - Retrieved rain rate, bars indicate uncertainty due to measurements, green dots indicate the "rain certain" category, blue and red dots indicate rain is less likely.

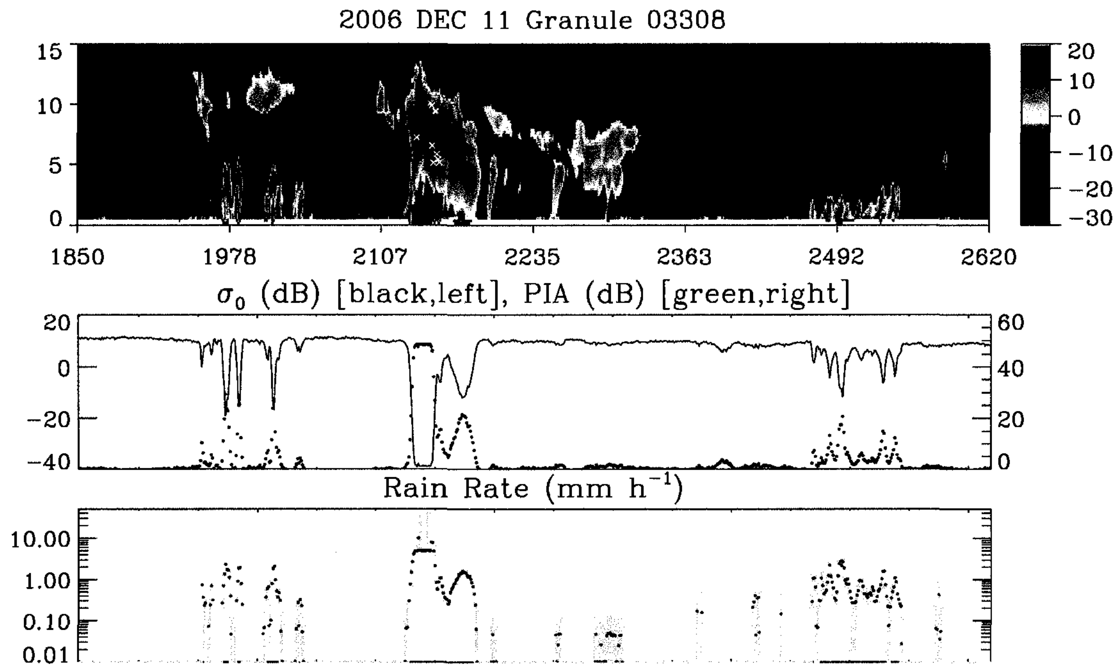

Figure 6.12: As in Figure 6.11. An example retrieval with precipitation falling from multi-layer cloud systems.

7 Conclusions

This dissertation has introduced a new path integrated attenuation (PIA) based precipitation retrieval algorithm applicable to spaceborne millimeter wavelength cloud radars. The algorithm was then applied to near-global observations from CloudSat's Cloud Profiling Radar.

Algorithm

The precipitation retrieval algorithm is based on the principle that measurements of the attenuated backscatter from the ocean surface, combined with knowledge of the ocean surface wind speed, sea surface temperature, and temperature and moisture in the atmospheric column, may be used to derive the PIA in a precipitating column. Assuming an exponential drop size distribution, the relationship between PIA and rain rate is easily derived from Mie theory for homogeneous columns of warm rain.

To account for the fact that rain drops often form from snow falling through the freezing level, a model of the melting layer is implemented to predict melted fraction of hydrometeors as a function of depth below the freezing level. The discrete dipole approximation is used to model dry snowflakes. When applied to the melting layer model, a peak in attenuation is produced several hundred meters below the freezing level as large melting particles become covered with liquid water. Failure to account for this extra attenuation results in a positive bias in precipitation rate.

Multiple scattering can be significant for the CPR for precipitation rates exceeding approximately 3-5 mm h^{-1}. Monte Carlo modeling of the radiative transfer equation shows that several orders of scatter (10 or more) may be required to adequately model the reflectivity in a heavily raining column. To accommodate multiple scattering, a lookup table approach is used whereby the observed PIA is matched to apparent PIA modeled through Monte Carlo methods, as a function of precipitating layer depth and freezing level height. Precipitating ice is shown to exhibit significant multiple scattering at liquid equivalent precipitation rates of greater than about 3 mm h^{-1}. Multiple scattering from ice tends to oppose the effects of attenuation, sometimes even producing regimes where PIA is practically invariant with precipitation rate.

The sensitivity of the radar and limits on the applicability of the surface reference technique in the presence of multiple scattering lead to an upper limit on precipitation rates that can be retrieved from CloudSat. For warm rain, the maximum retrievable rain rate varies between over 25 mm h^{-1} for a raining column up to 2 km thick to about 5 mm h^{-1} for a 5 km deep column. Addition of ice increases the range of retrievable precipitation rates because of multiple scattering effects. Uncertainties in retrieved precipitation rate are generally largest for very small values ($<$ 0.1 mm h^{-1}) and moderate values (between 5 and 10 mm h^{-1}) when the freezing level is lower than 2.5 km.

The algorithm is incorporated into the experimental CloudSat 2C-PRECIP-COLUMN product detailed in Appendix B. The flexible forward model for radar reflectivity, QuickBeam, is publicly available.

Precipitation incidence

The CloudSat CPR is an excellent detector of precipitation because of the high sensitivity of the radar (approximately −30 dBZ). Precipitation is detected using near-surface reflectivity thresholds corrected for PIA. The combination of cloud height information from the CPR with precipitation detection is particularly powerful. Some key results from application of the precipitation detection algorithm follow.

- The oceans between 60° north and south latitude are cloudy approximately 72% of the time, exceeding 80% poleward of 40° latitude. Cloudiness of the global tropical oceans predominantly favors clouds with tops in layers centered at 2 and 15 km. Precipitating clouds also prefer these modes.

- A middle level mode of cloudiness and precipitation, including the congestus mode, is present through most of the tropics. It is especially pronounced in the western Pacific and Indian Ocean basins, but is also found in the Atlantic basin. The cloud top height characterizing this mode is near the tropical freezing level.

- Applying the combined CloudSat/CALIPSO cloud mask allows derivation of a crude precipitation index defined as the ratio of cloud occurrence to precipitation occurrence. This index varies regionally in the tropics, averaging about 0.1; the largest values in the tropical region are in the western Pacific (~0.12), while smaller values (~0.07) occur in the eastern Atlantic stratus regions.

- There are vast regions of the globe where nearly all precipitation falls from clouds with cloud top heights of the lowest layer (CTL) less than the 4.75 km.

These include the stratus regions on the west sides of the continents. Over the tropical oceans as a whole, precipitation falls approximately twice as often from clouds with CTL less than 4.75 km than any other cloud type.

- Multiple layered cloud systems are ubiquitous globally. Over half of observed cloudy scenes in the tropics, for example, contain more than one cloud layer. Similarly, over half the time rain is occurring, multiple layers are present. It is a misconception that most tropical rain falls in a deep mode where convection extends from near the surface to the tropical tropopause.

Accumulated precipitation and comparisons with other sensors

Precipitation accumulations form CloudSat are subject to greater uncertainties than detection. However a number of points can be made here.

- Tropical precipitation incidence of precipitation is very similar for CloudSat and AMSR-E. Both instruments observe rain in the light (<1 mm h^{-1}), moderate (1 to 5 mm h^{-1}), and heavy (> 5 mm h^{-1} precipitation categories with a similar frequency in the tropics.

- In the middle latitudes, CloudSat observations suggest precipitation occurs nearly twice as frequently as AMSR-E. This is especially true in the winter hemisphere where the storm tracks are most active. The CloudSat observations are more in line with surface shipping observations than the passive microwave.

- Total accumulated precipitation estimates from CloudSat, when averaged seasonally, compare fairly well with other sensors, especially in the tropics, though CloudSat has a negative precipitation accumulation bias in areas where full attenuation occurs frequently. In the middle latitudes, CloudSat precipitation accumulations are generally higher than other sensors. Since passive microwave precipitation estimates are less reliable at higher latitudes and virtually no in-situ ocean rainfall observations exist, there is little point for comparison.

- There are large areas on the planet, including the stratus regions, where rain less than 1 mm h^{-1} dominates precipitation accumulation viewed by CloudSat.

- About 16% of the tropical rain observed by CloudSat during DJF 2006-2007 was light, less than 1 mm h^{-1}. For the TRMM PR, this number is found to be 6%. The true value probably lies between these two estimates and somewhat closer to the CloudSat estimate.

- The CTL of cloud structures responsible for tropical rainfall accumulation exhibits a bimodal structure, with precipitating clouds showing similar structures. Middle latitude CTL's also suggest bimodality during DJF 2006-2007.

- Multiple layered cloud systems produce more than half of the CPR-observed precipitation in the tropics. Of precipitation falling from multiple layer cloud systems, the CTL is nearly equally distributed among low, middle, and high clouds. The classic model of deep convection as the dominant mode of tropical rainfall is again brought into question.

Appendices

A PIA / Precipitation Rate Tables

This appendix contains graphical representations of the lookup tables that are the output of the algorithm described in chapter 5. Each plot shows apparent path integrated attenuation that is calculated from the Monte Carlo model versus a discrete array of precipitation rates. In the titles above each figure, "D=" refers to the depth of the raining column and "F=" refers to the depth of the freezing level, where applicable, in km above the surface. The first figure, Fig. A.1, shows calculations for pure rain, while the following figures show results for a mixture of snow and rain.

Solid crosses represent raw Monte Carlo output, while the red lines are curves fit to the output. For $R \geq 0.05$, log-polynomial curves are used:

$$PIA_{fit} = \sum_{j=0}^{n} a_j \, [\ln(R)]^j \, , \qquad (94)$$

with n being the order of the polynomial (varying from 5 to 8 depending on R) and a being the fit coefficients. For $R < 0.05$, a third order polynomial is used to fit the "hump" due to rapid growth of the prescribed cloud water to rain water ratio at low rain rates.

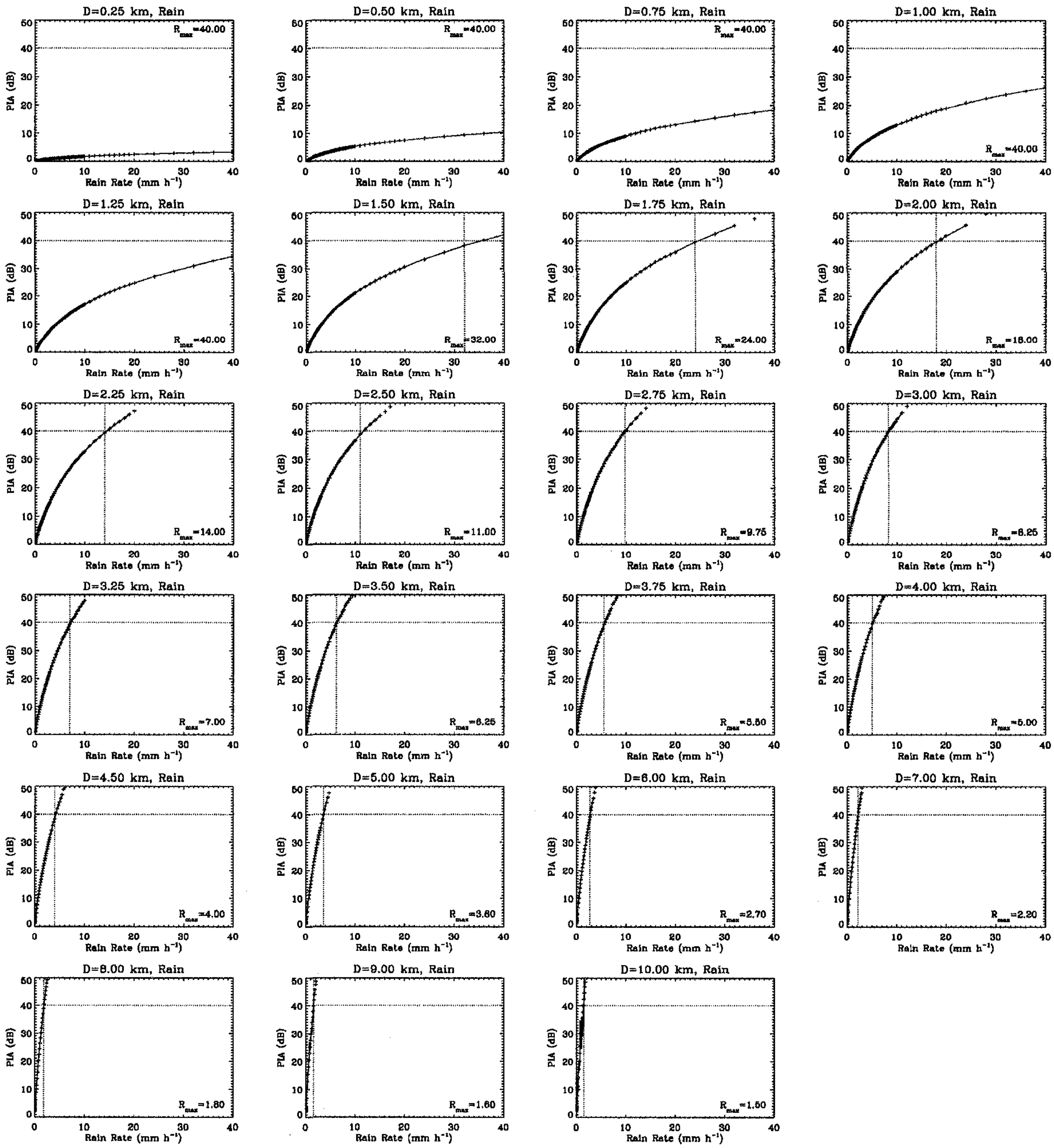

Figure A.1: PIA lookup tables, pure rain of various depths

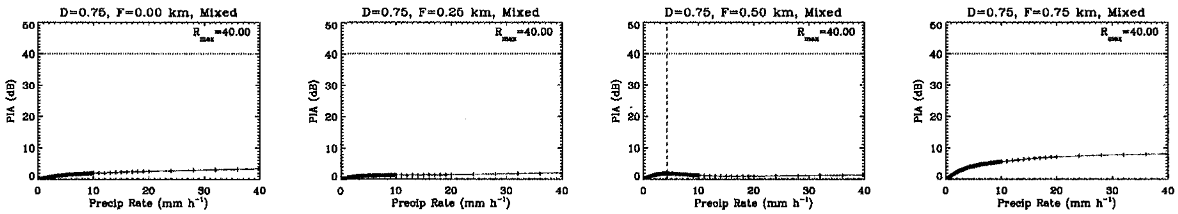

Figure A.2: PIA lookup tables, mixed phase, D = 0.75 km

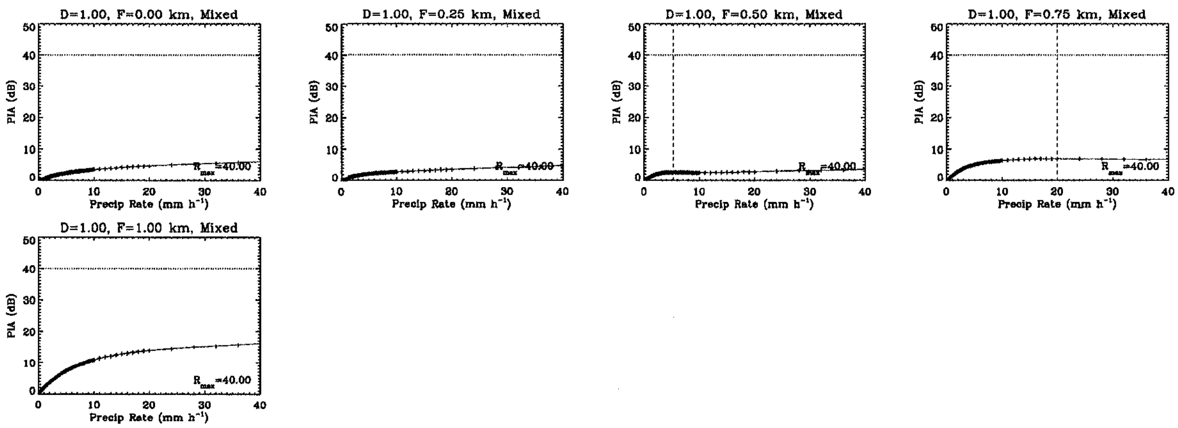

Figure A.3: PIA lookup tables, mixed phase, D = 1.00 km

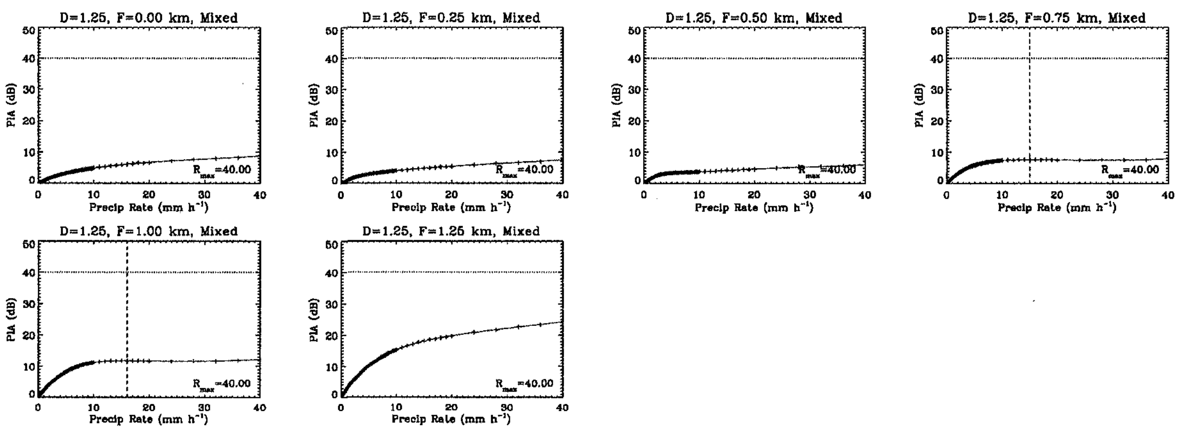

Figure A.4: PIA lookup tables, mixed phase, D = 1.25 km

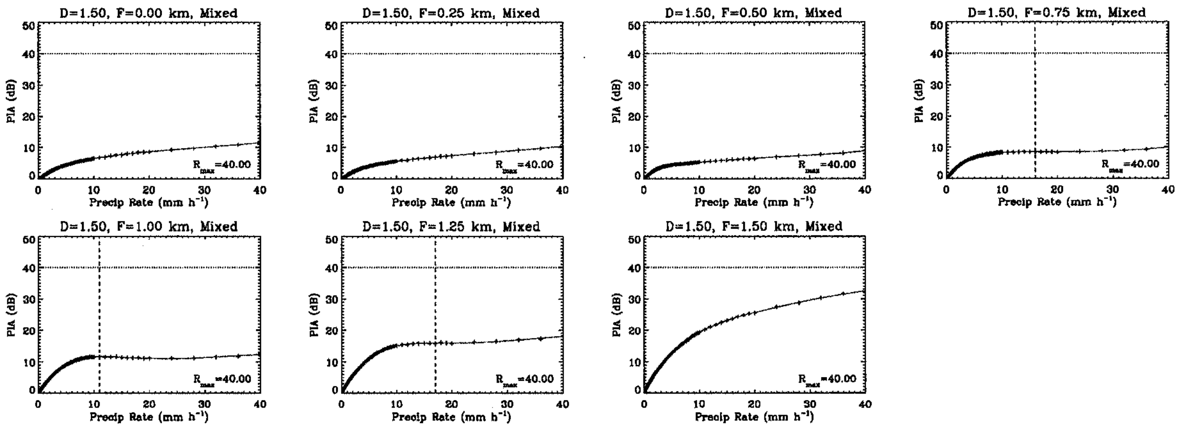

Figure A.5: PIA lookup tables, mixed phase, D = 1.50 km

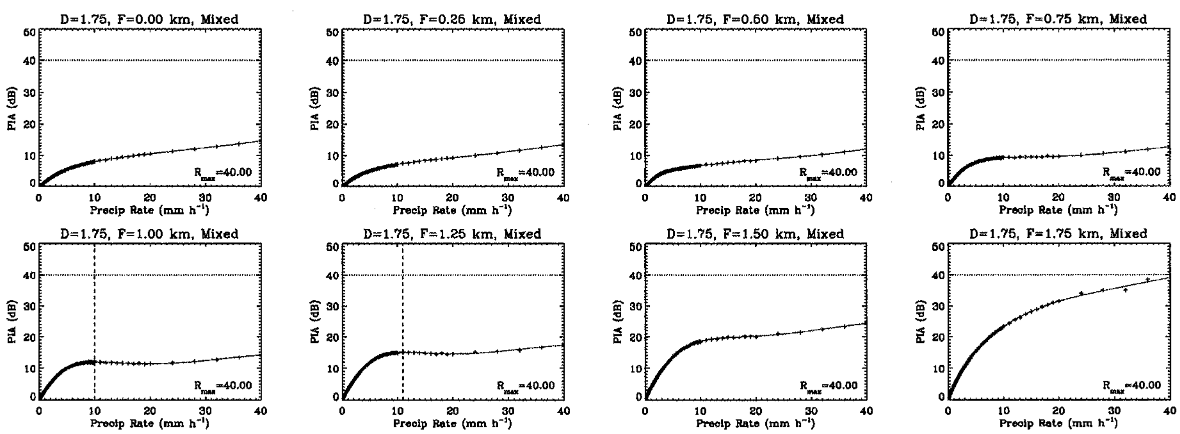

Figure A.6: PIA lookup tables, mixed phase, D = 1.75 km

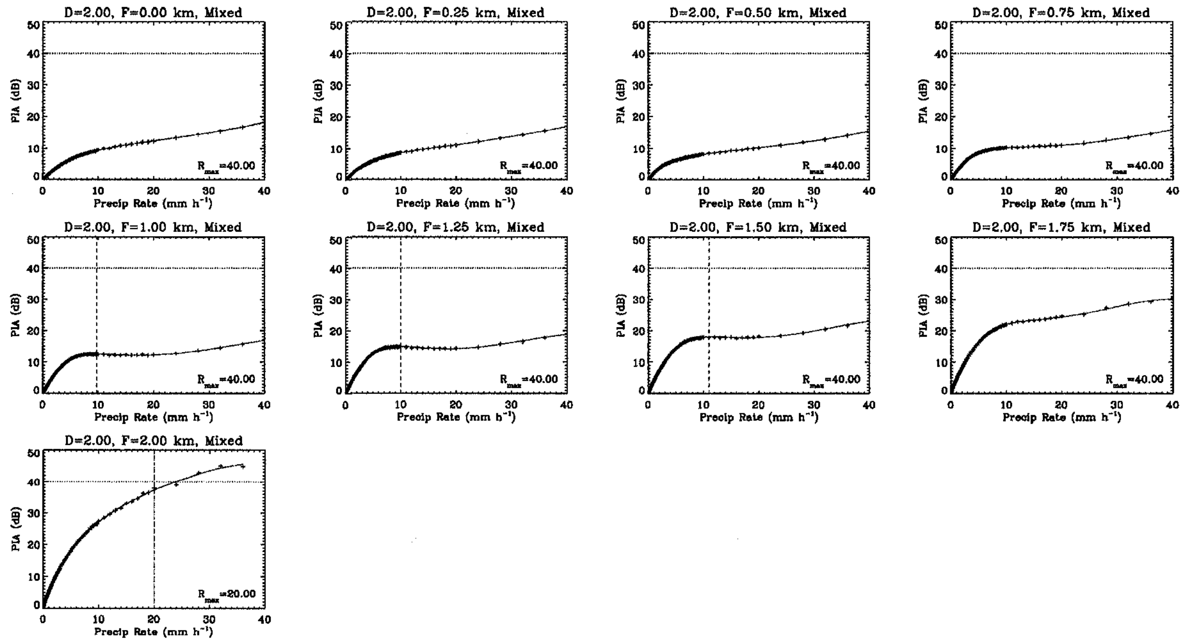

Figure A.7: PIA lookup tables, mixed phase, D = 2.00 km

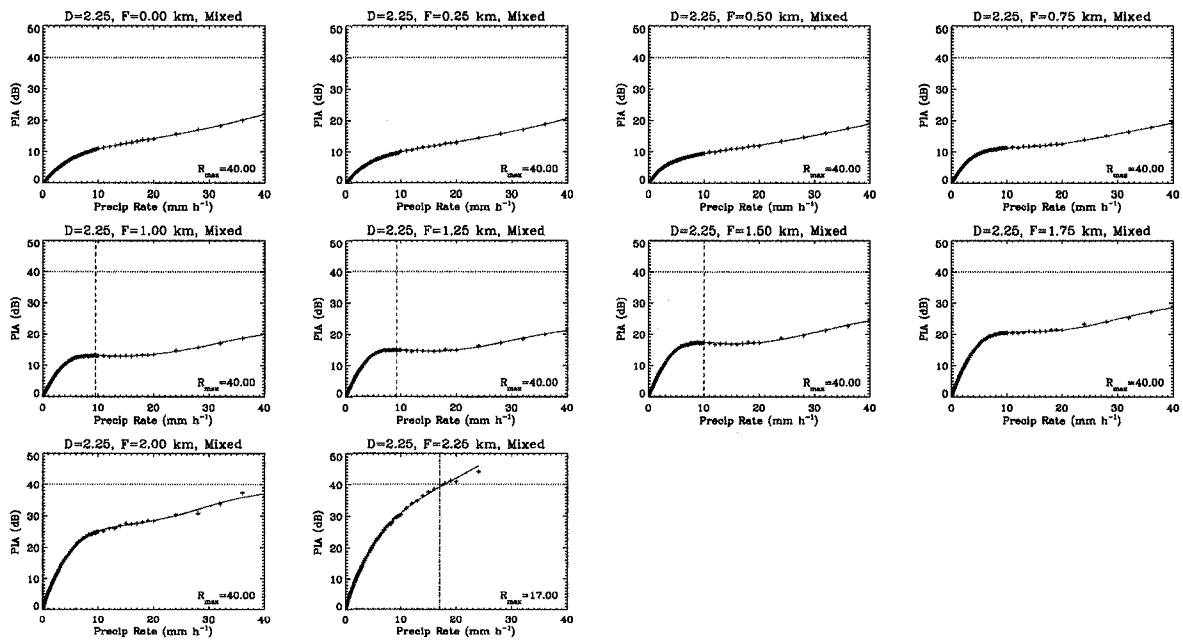

Figure A.8: PIA lookup tables, mixed phase, D = 2.25 km

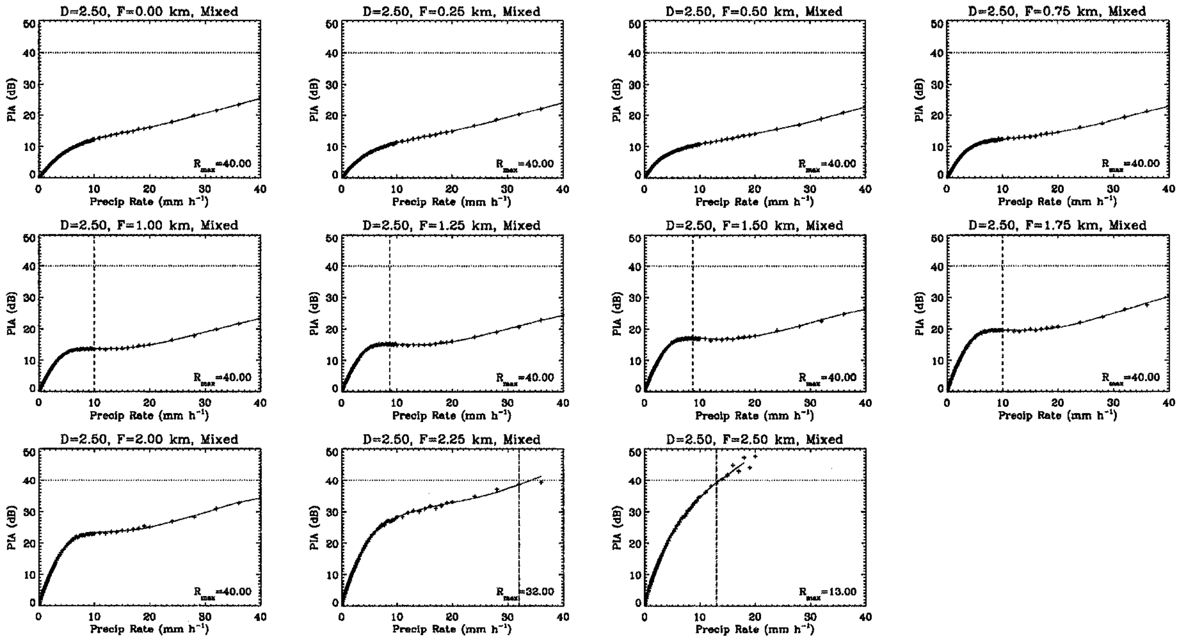

Figure A.9: PIA lookup tables, mixed phase, D = 2.50 km

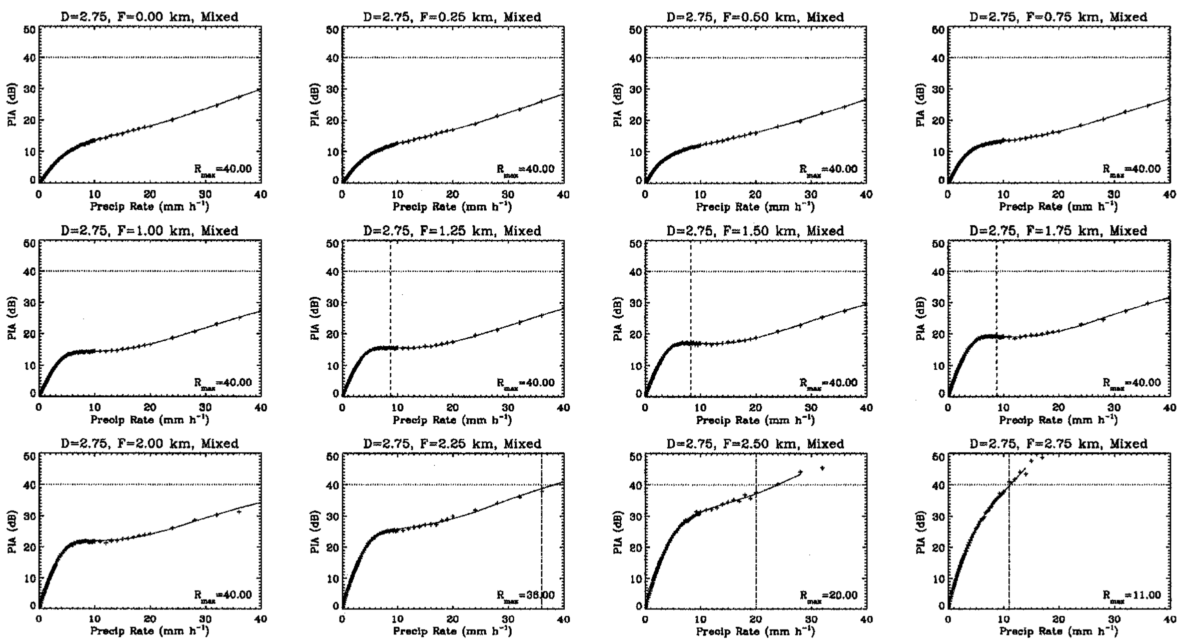

Figure A.10: PIA lookup tables, mixed phase, D = 2.75 km

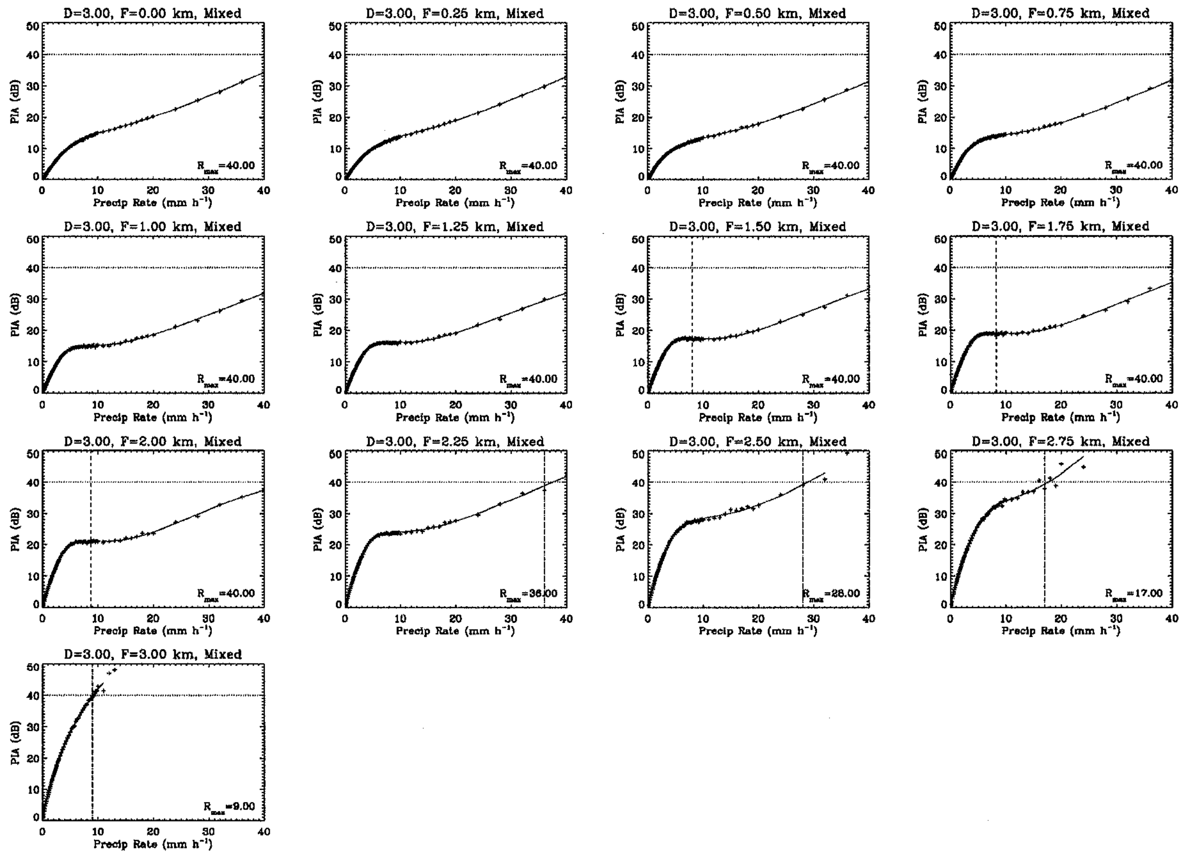

Figure A.11: PIA lookup tables, mixed phase, D = 3.00 km

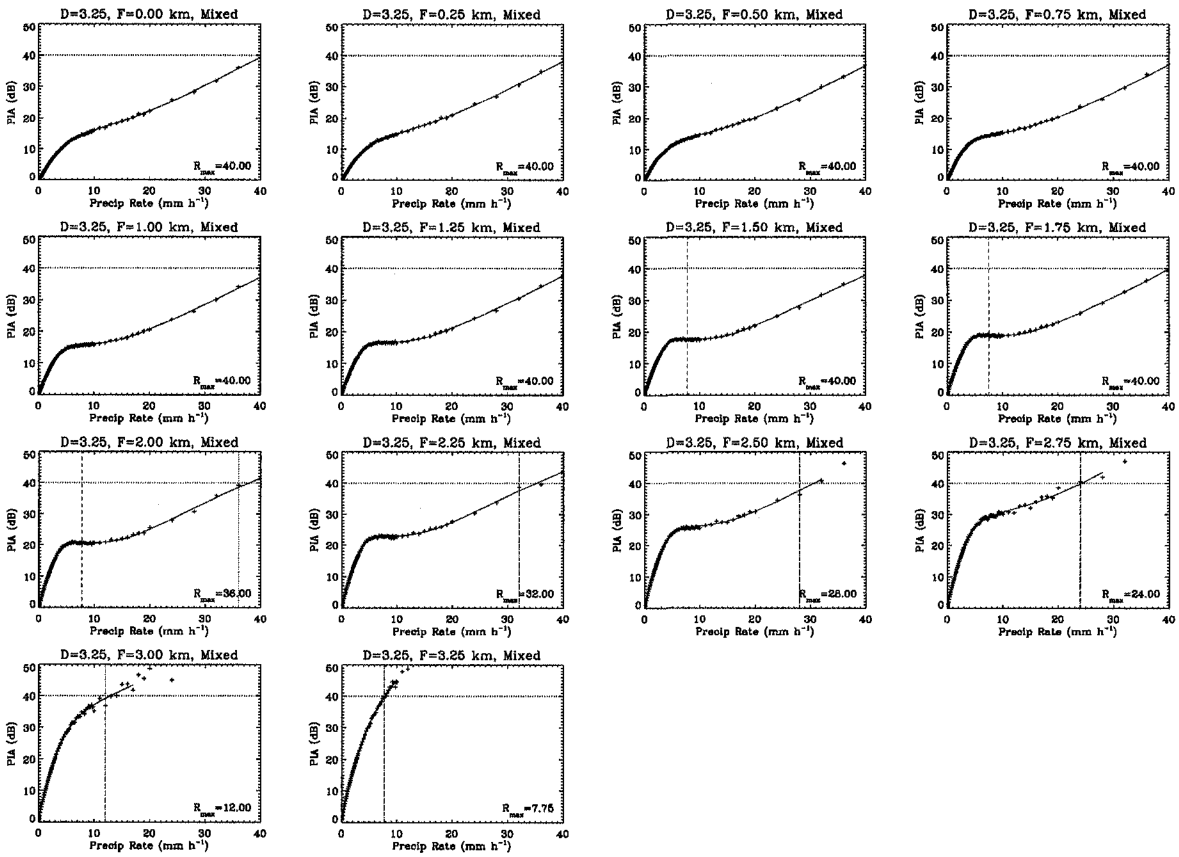

Figure A.12: PIA lookup tables, mixed phase, D = 3.25 km

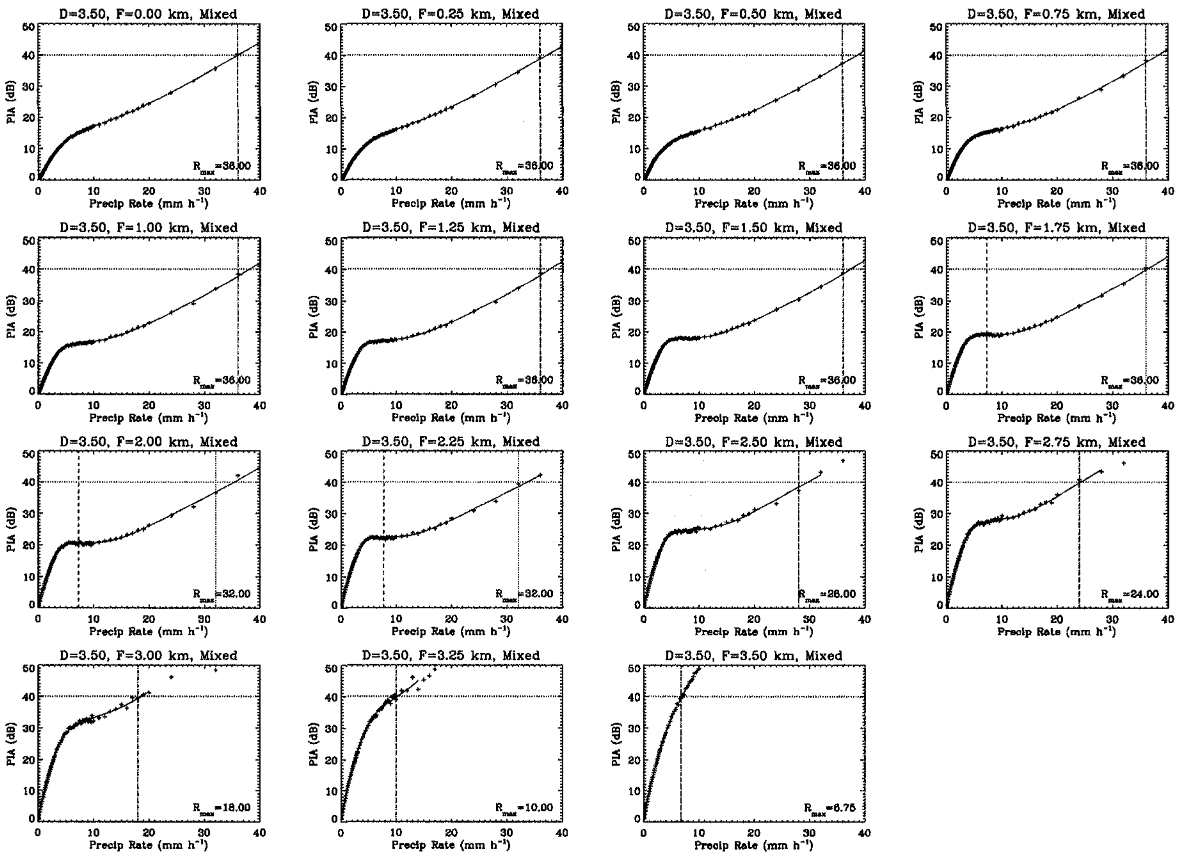

Figure A.13: PIA lookup tables, mixed phase, D = 3.50 km

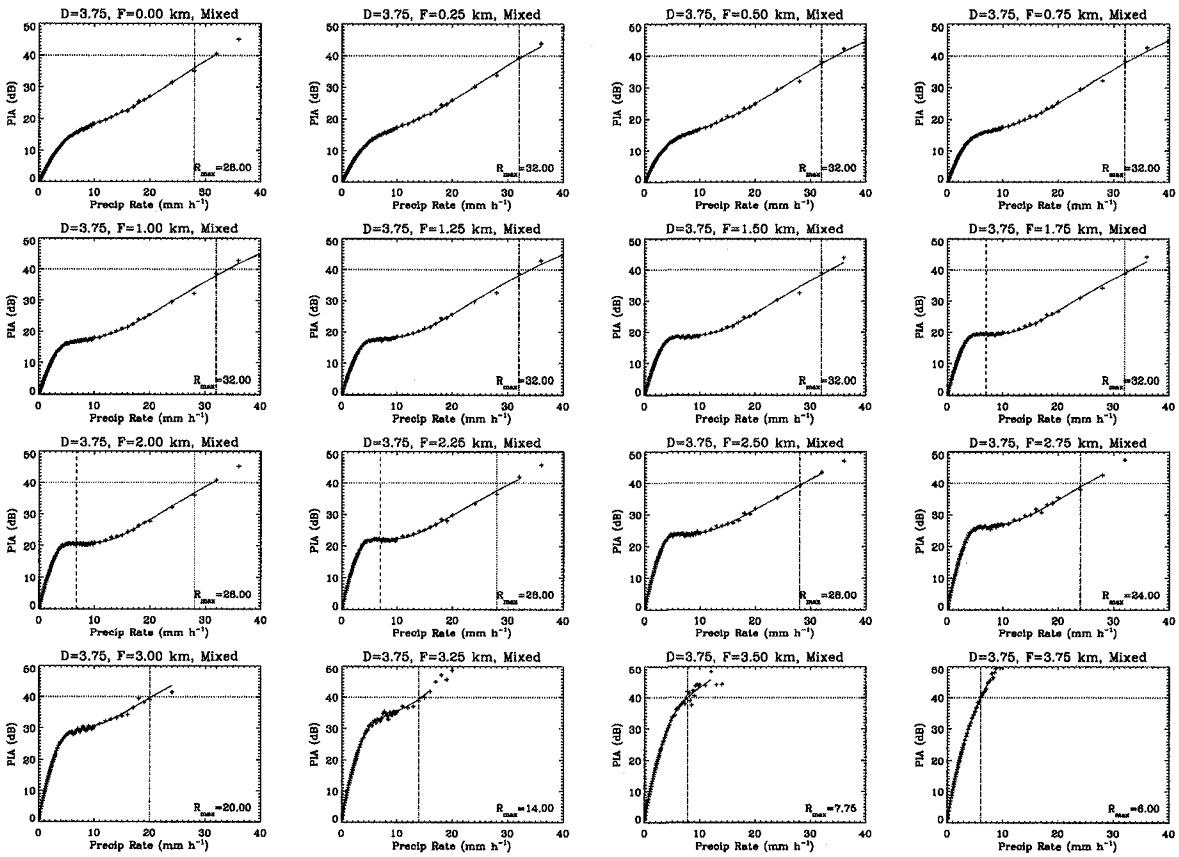

Figure A.14: PIA lookup tables, mixed phase, D = 3.75 km

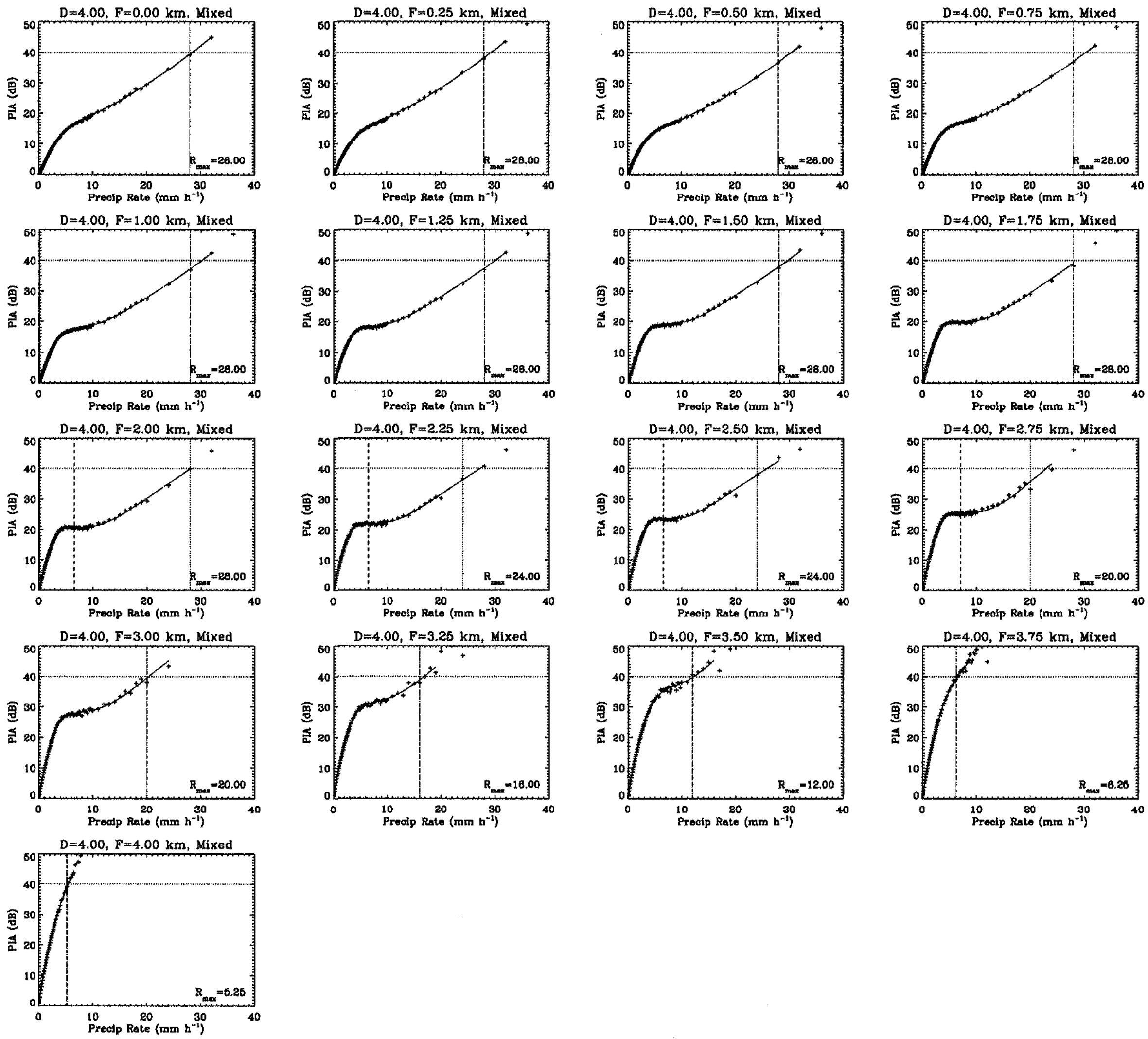

Figure A.15: PIA lookup tables, mixed phase, D = 4.00 km

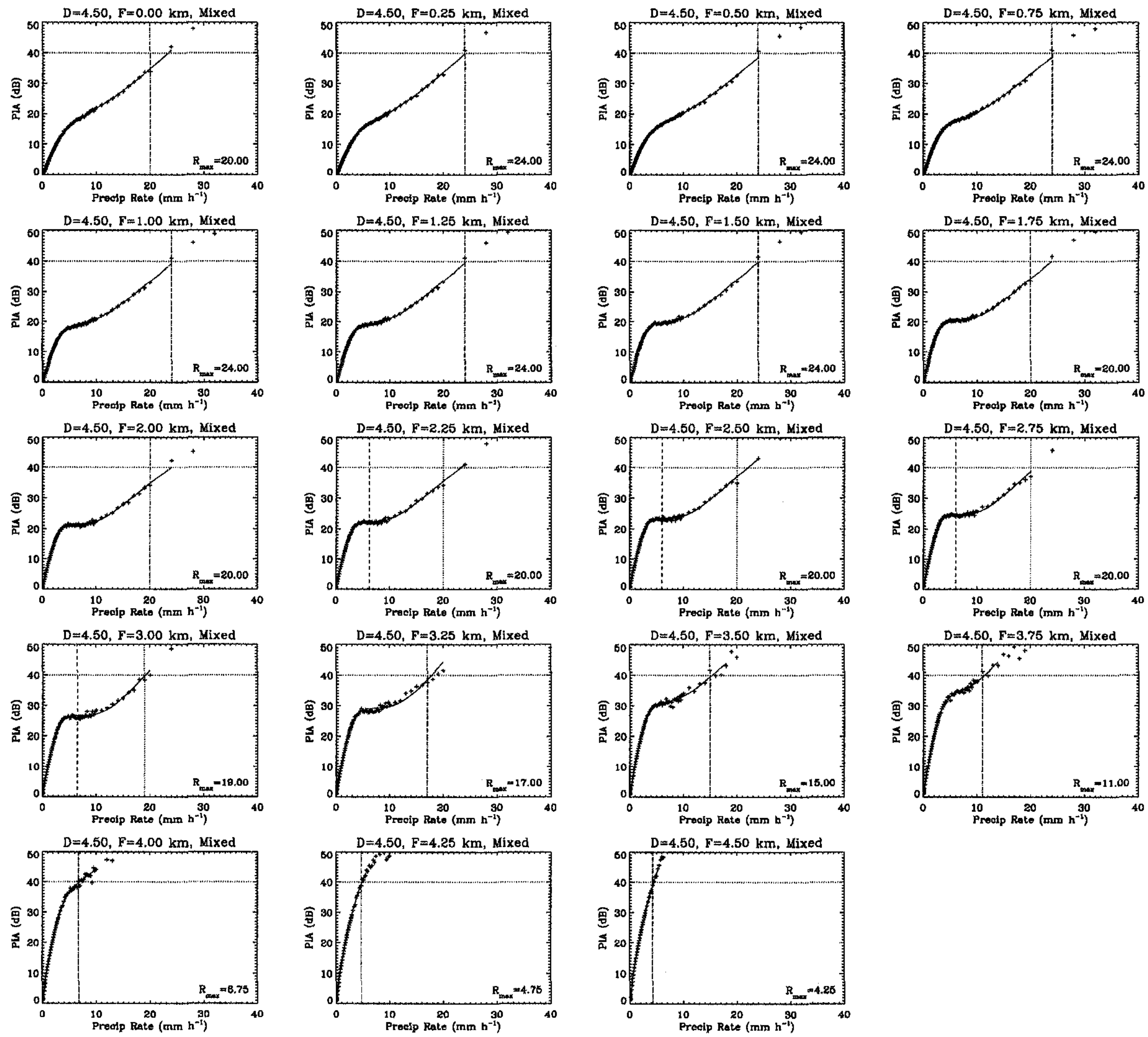

Figure A.16: PIA lookup tables, mixed phase, D = 4.50 km

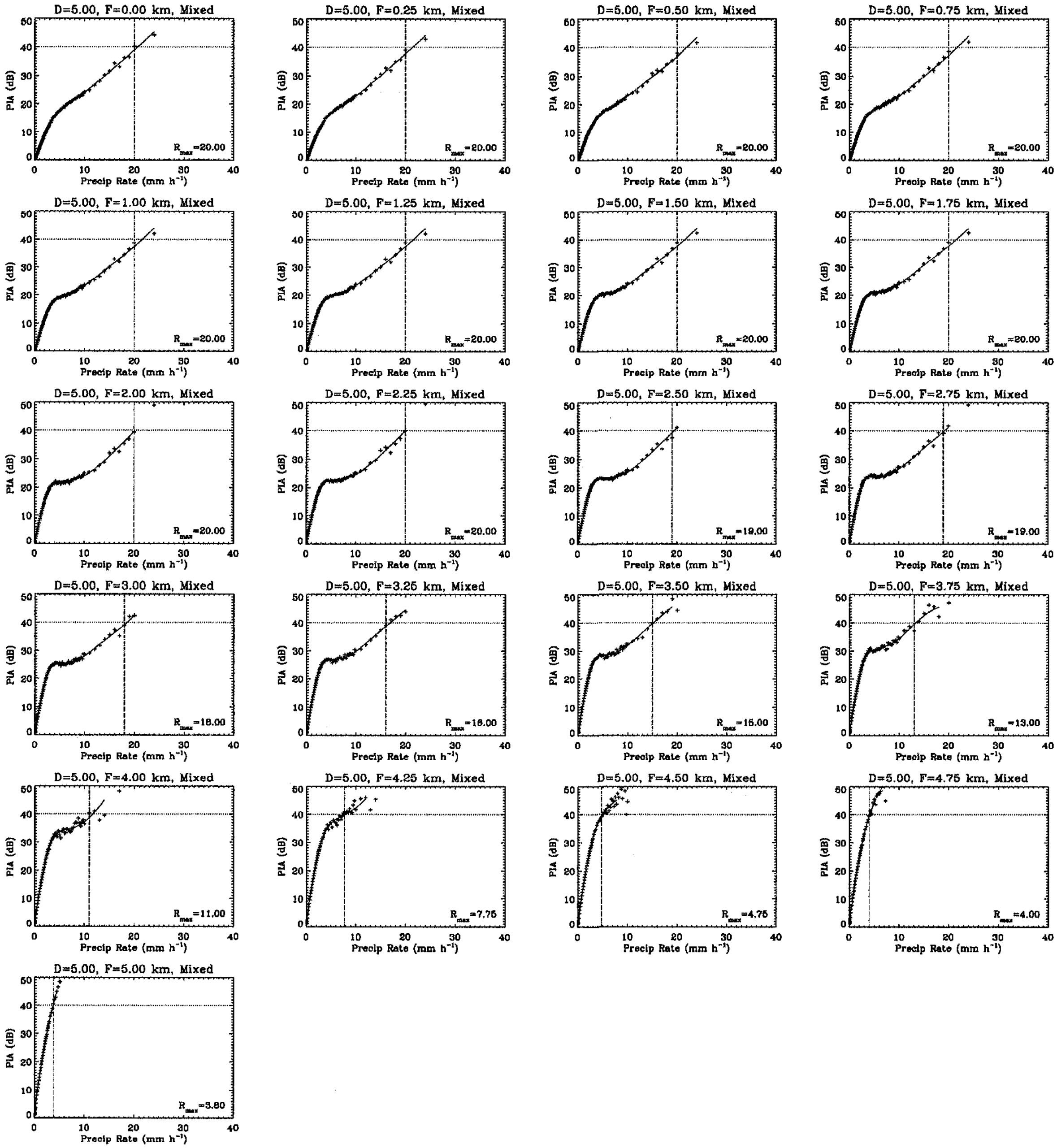

Figure A.17: PIA lookup tables, mixed phase, D = 5.00 km

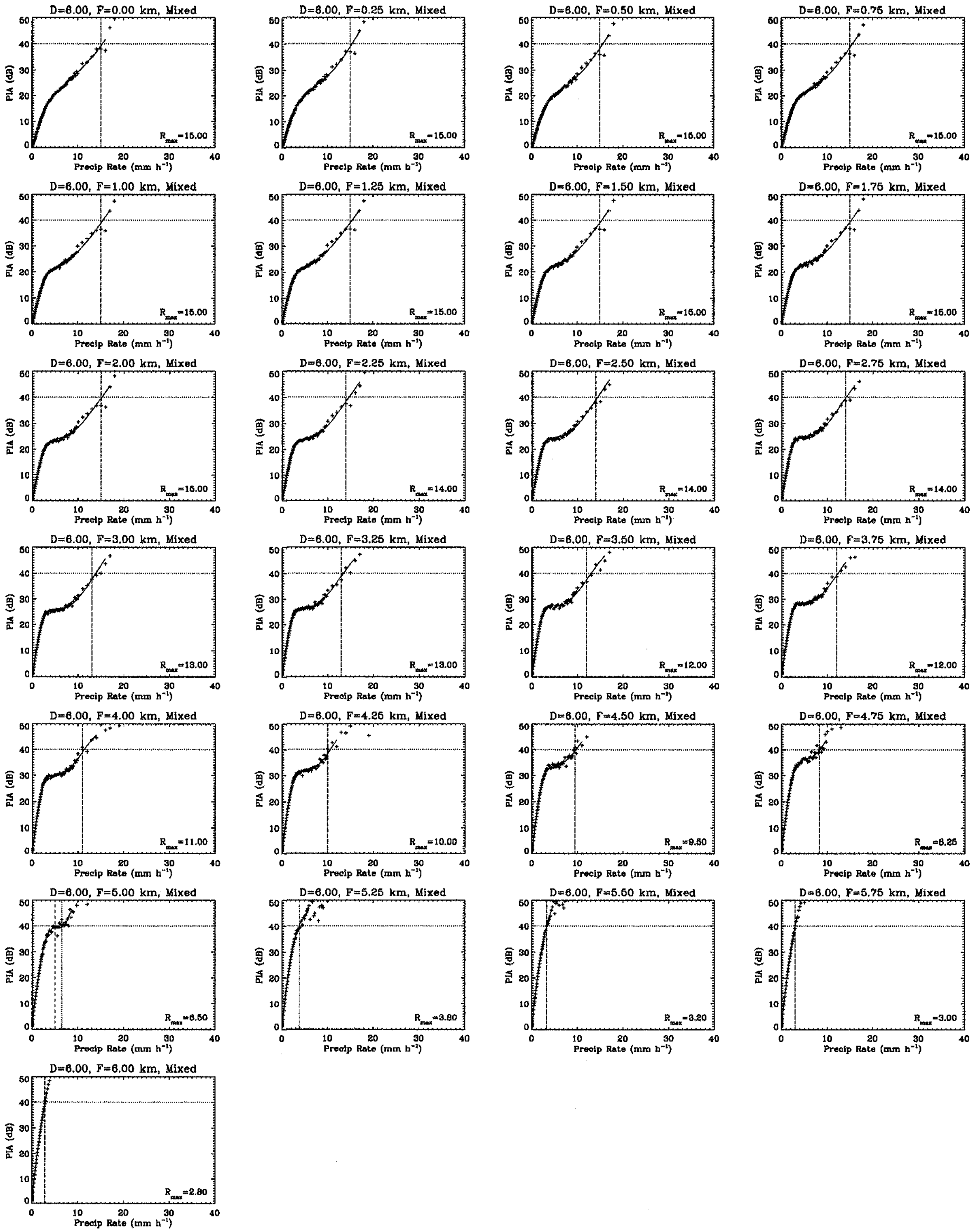

Figure A.18: PIA lookup tables, mixed phase, D = 6.00 km

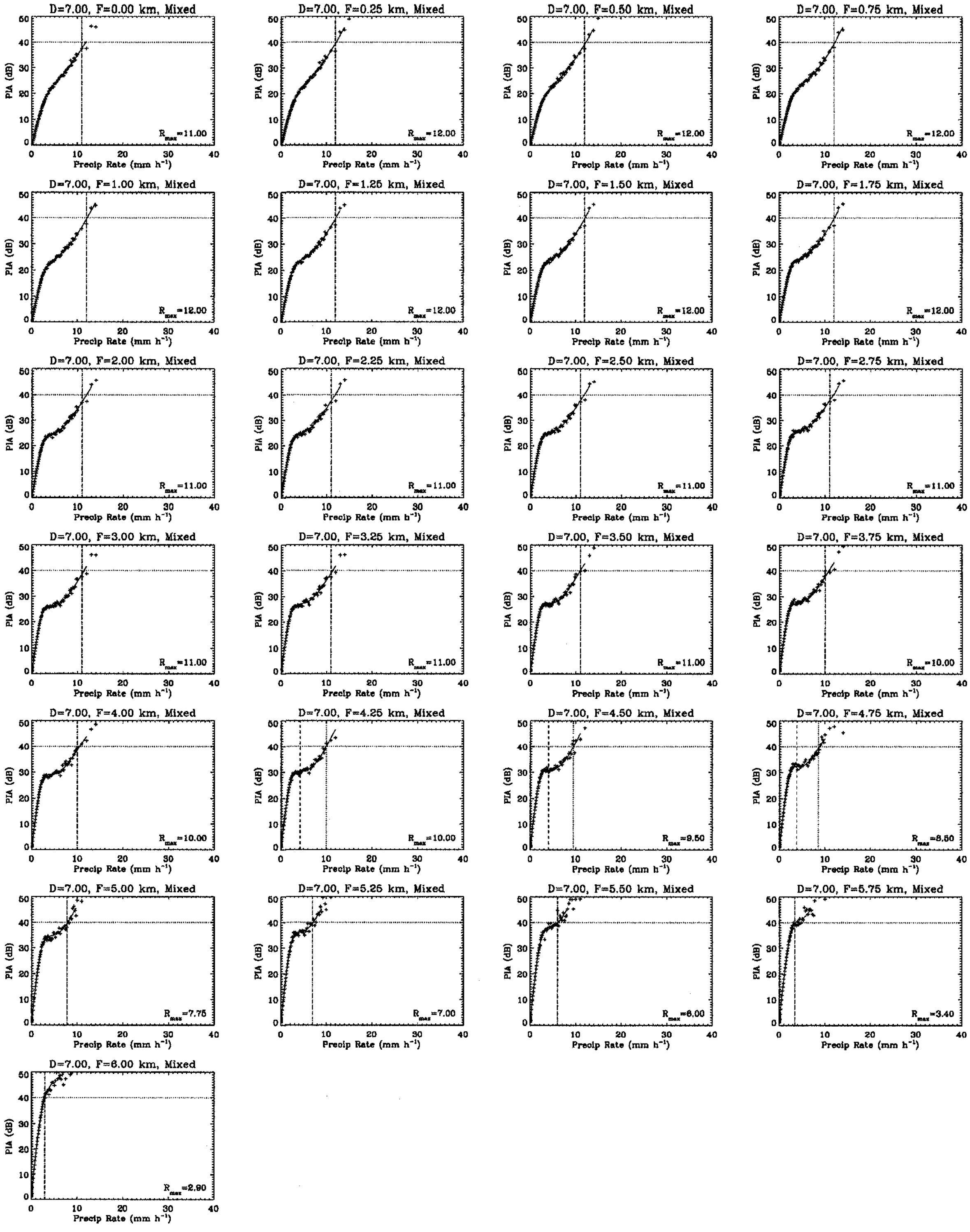

Figure A.19: PIA lookup tables, mixed phase, D = 7.00 km

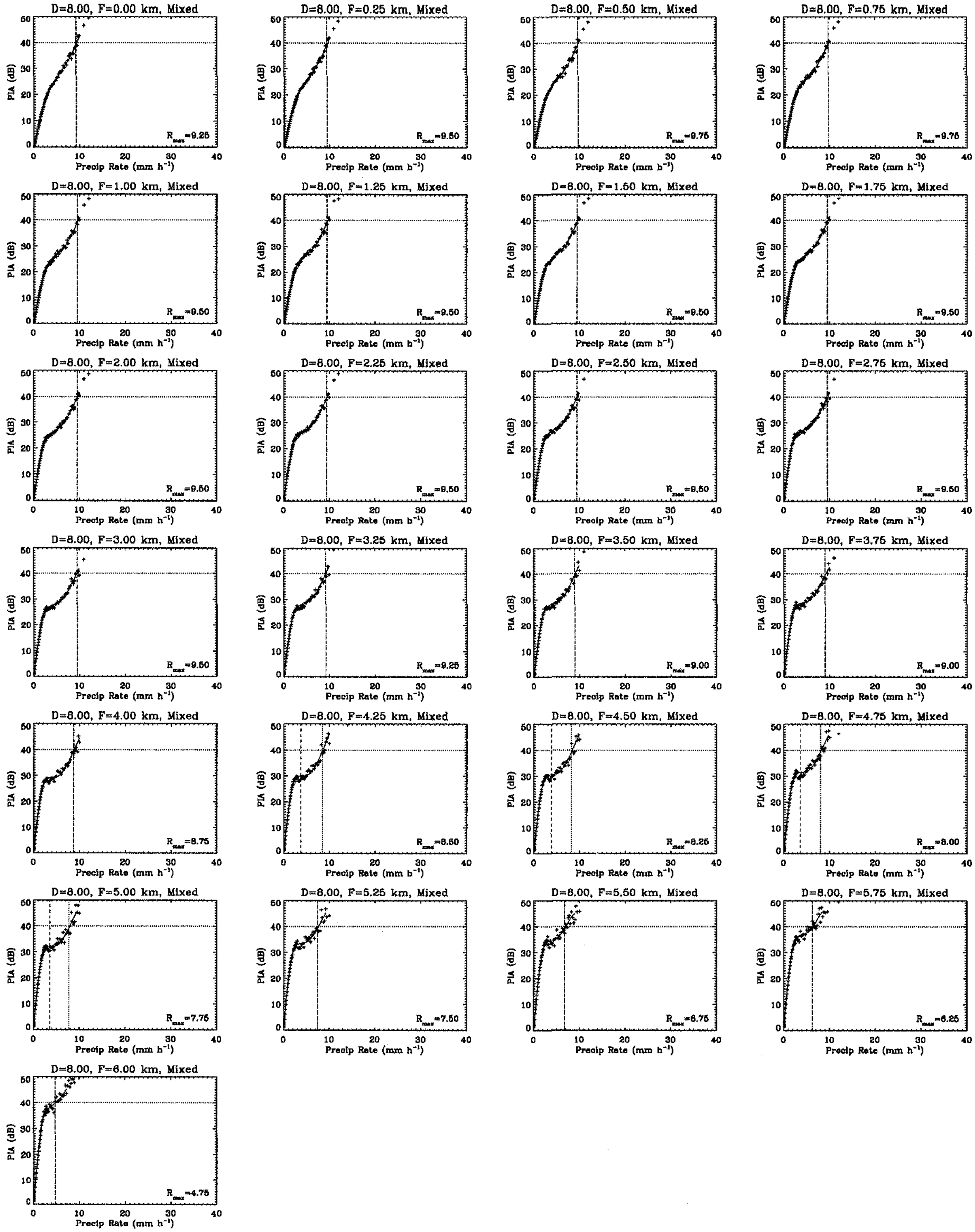

Figure A.20: PIA lookup tables, mixed phase, D = 8.00 km

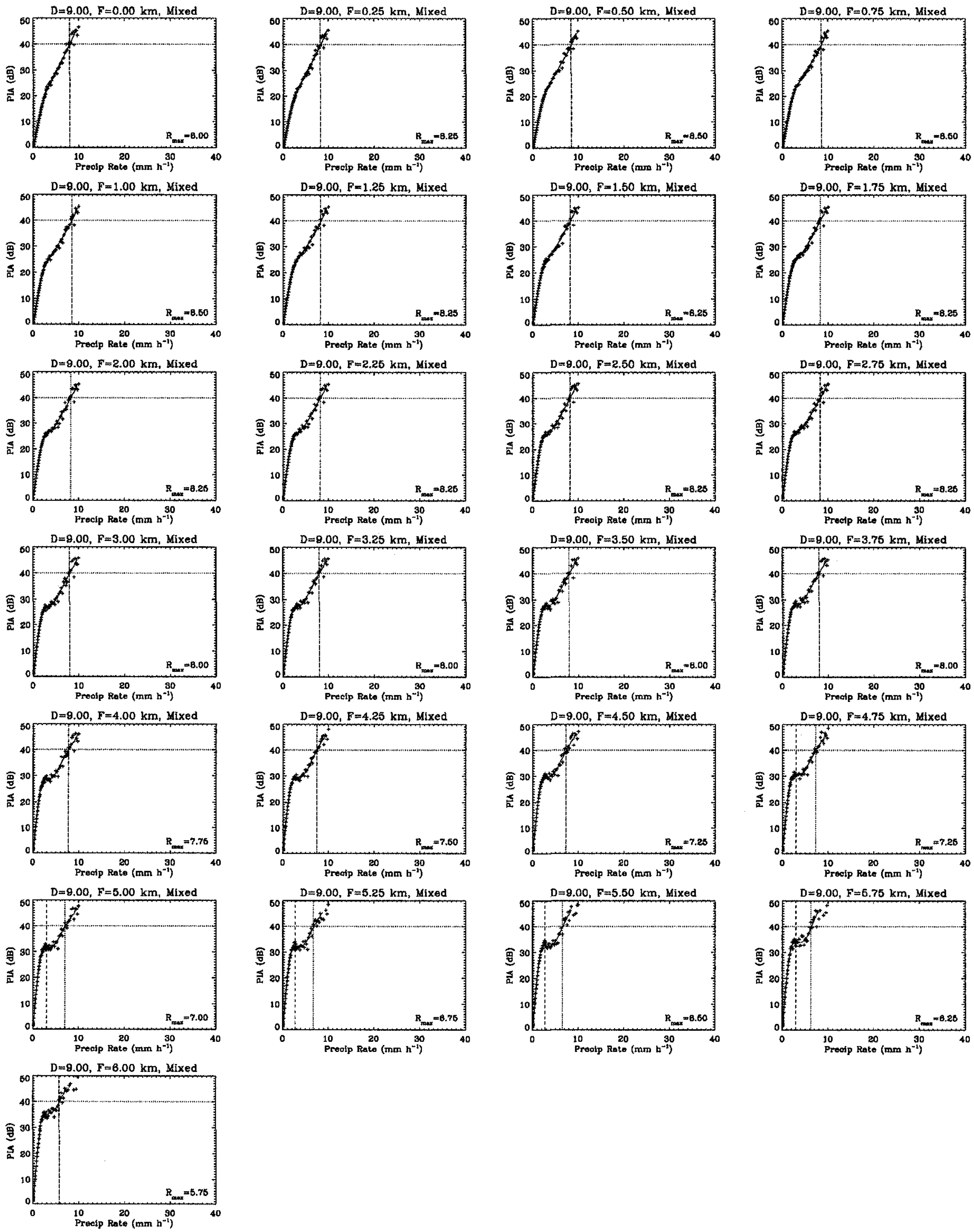

Figure A.21: PIA lookup tables, mixed phase, D = 9.00 km

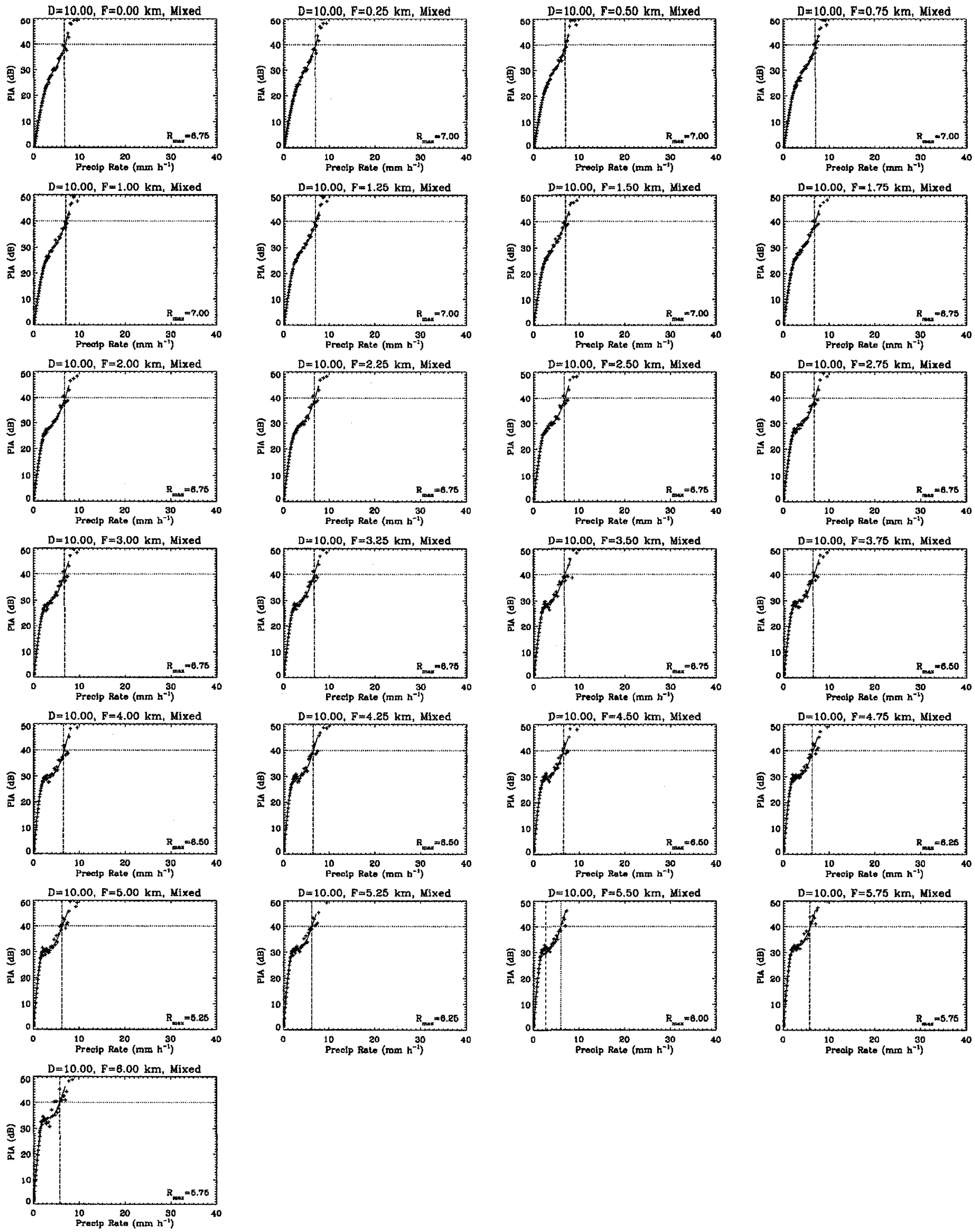

Figure A.22: PIA lookup tables, mixed phase, D = 10.00 km

B CloudSat Precipitation: 2C-PRECIP-COLUMN Product

This appendix contains information on the 2C-PRECIP-COLUMN product created by the author. This product is an experimental CloudSat product, intended to be run and hosted by the Cooperative Institute for Research in the Atmosphere (CIRA) on their CloudSat data product page. The product is archived in HDF format, consistent with other CloudSat products, with each granule (file) representing one CloudSat orbit. There are approximately 15 orbits per day, and each orbit requires approximate 3 megabytes storage space. The variable list for the product is listed below.

```
2C-PRECIP-COLUMN Precipitation Product
Variable List - Version 1.02
Data contact: John Haynes (haynes@atmos.colostate.edu)

-------------------------------------------------------------------
> Precip_rate
-------------------------------------------------------------------
Precipitation rate (mm/hr).

-------------------------------------------------------------------
> Precip_rate_min
-------------------------------------------------------------------
Lower bound on precipitation rate given instrument uncertainty
(mm/hr).

-------------------------------------------------------------------
> Precip_rate_max
-------------------------------------------------------------------
Upper bound on precipitation rate given instrument uncertainty
(mm/hr).
```

```
-------------------------------------------------------------------
> Precip_rate_no_ms
-------------------------------------------------------------------
Precipitation rate that would be retrieved without considering
multiple scattering effects; provided for information only, do not
use as a physical precipitation rate (mm/hr).

-------------------------------------------------------------------
> PIA_hydrometeor
-------------------------------------------------------------------
Path integrated attenuation due to hydrometeors (dB).

-------------------------------------------------------------------
> Sigma_zero
-------------------------------------------------------------------
Surface attenuated backscatter cross section (dB).

-------------------------------------------------------------------
> Near_surface_reflectivity
-------------------------------------------------------------------
Reflectivity in the fourth bin (~750 m) above surface (dBZ).

-------------------------------------------------------------------
> Cloud_top_lowest_layer
-------------------------------------------------------------------
The cloud top height of the lowest cloud layer (km).

-------------------------------------------------------------------
> Frozen_precip_height
-------------------------------------------------------------------
The maximum height reached by frozen precipitation (km).

-------------------------------------------------------------------
> Melted_fraction
-------------------------------------------------------------------
The total mass fraction of liquid water contained in precipitation.

-------------------------------------------------------------------
> Status_flag
-------------------------------------------------------------------
0 - both the quantitative precip rate and occurrence retrievals
    were successful
1 - only the precip occurrence retrieval was successful; no precip
    rate was retrieved (see Retrieval_info_flag)
```

```
8 - no retrieval attempted (land or sea ice)

Values of 10 or greater indicate an error condition occurred.

-------------------------------------------------------------------
> Precip_flag
-------------------------------------------------------------------
0 - no precip detected
1 - rain possible
2 - rain probable
3 - rain certain
4 - snow possible
5 - snow certain
8 - no retrieval attempted (land or sea ice)
9 - uncertain, see Status_flag

-------------------------------------------------------------------
> Retrieval_info_flag
-------------------------------------------------------------------
0 - no additional information to report
8 - no retrieval attempted (land or sea ice)
9 - uncertain, see Status_flag

Reason no quantitative precip rate retrieval was performed:
1 - melted fraction too small
2 - only snow was present
3 - PIA not significantly larger than noise
4 - retrieved rain rate less than minimum allowable

Additional information:
50 - precipitation rate ceiling was encountered
51 - multiple solutions were found

-------------------------------------------------------------------
> Phase_flag
-------------------------------------------------------------------
Describes the phase(s) of precipitation that are present in the
observed radar profile:
0 - no precip
1 - rain only
2 - snow only
3 - rain and significant precipitating ice
4 - rain and ice are present; however precipitating ice content is
    small and neglected in the retrieval process
```

```
8 - no retrieval attempted (land or sea ice)
9 - uncertain, see Status_flag

-------------------------------------------------------------------
> Cloud_flag
-------------------------------------------------------------------
0 - no cloud or cloud unlikely
    (GEOPROF cloud mask is less than 30)
1 - cloud present with high certainty
    (GEOPROF cloud mask is 30 or 40)
9 - cloud presence unknown

-------------------------------------------------------------------
> Freezing_level
-------------------------------------------------------------------
The height of the freezing level; from ECMWF (km).

-------------------------------------------------------------------
> SST
-------------------------------------------------------------------
The sea surface temperature; from ECMWF (deg C).

-------------------------------------------------------------------
> Surface_wind
-------------------------------------------------------------------
The surface wind speed; from ECMWF (m/s).

-------------------------------------------------------------------
> Aux_CWV_AMSR
-------------------------------------------------------------------
Column water vapor; derived from microwave, from AMSR-E (mm).

-------------------------------------------------------------------
> Aux_LWP_AMSR
-------------------------------------------------------------------
Column liquid water path; derived form microwave, from AMSR-E (mm).

-------------------------------------------------------------------
> Aux_SST_AMSR
-------------------------------------------------------------------
Sea surface temperature; Wentz ocean products, from AMSR-E (deg C).
```

```
-------------------------------------------------------------------
> Aux_precip_AMSR
-------------------------------------------------------------------
Rain rate; derived from microwave, from AMSR-E (mm/hr).

-------------------------------------------------------------------
> Aux_dist_AMSR
-------------------------------------------------------------------
Distance to center of AMSR-E pixel (km).
```

References

Adler, R. F., G. J. Huffman, A. Chang, R. Ferraro, P. Xie, J. Janowiak, B. Rudolf, U. Schneider, S. Curtis, D. Bolvin, A. Gruber, J. Susskind, P. Arkin, and E. Nelkin, 2003: The version-2 global precipitation climatology project (gpcp) monthly precipitation analysis (1979-present). *J. Hydrometeorol.*, **4**, 1147–1167.

Amayenc, P., J. P. Diguet, M. Marzoug, and T. Tani, 1996: A class of single- and dual-frequency algorithms for rain-rate profiling from a spaceborne radar. part ii: Tests from airborne radar measurements. *J. Atmos. Oceanic Technol.*, **13**, 142–164.

Arnell, N. W., 1999: Climate change and global water resources. *Global Environmental Change-Human And Policy Dimensions*, **9**, S31–S49.

Austin, R. T. and G. L. Stephens, 2001: Retrieval of stratus cloud microphysical parameters using millimeter-wave radar and visible optical depth in preparation of cloudsat: 1. algorithm formulation. *J. Geophys. Res.*, **106**, 28233–28242.

Battaglia, A., M. O. Ajewole, and C. Simmer, 2007: Evaluation of radar multiple scattering effects in cloudsat configuration. *Atmos. Chem. Phys.*, **7**, 1719–1730.

Battaglia, A., J. M. Haynes, T. S. LEcuyer, and C. Simmer, 2008: Identifying multiple scattering in cloudsat observations over the oceans. *Submitted to J. Geophys. Res.*.

Battaglia, A., C. Kummerow, D. Shin, and C. Williams, 2003: Constraining microwave brightness temperatures by radar brightband observations. *J. Atmos. Oceanic Technol.*, **20**, 856–871.

Bissonnette, L. R., 1988: Multiple scattering of narrow light beams in aerosols. *Applied Optics*, **27**, 2478–2484.

Bodas-Salcedo, A., J. M. Haynes, et al., 2008: Evaluation of cloud systems in the met office global forecast model using cloudsat data. *In prep.*

Bohren, C. F. and L. J. Battan, 1982: Radar backscattering of microwaves by spongy ice spheres. *J. Atmos. Sci*, **39**, 2623–2629.

Bohren, C. F. and D. R. Huffman, 1983: *Absorption and scattering of light by small particles*. John Wiley and Sons, Inc., New York.

Brown, P. R. A. and P. N. Francis, 1995: Improved measurements of the ice water content in cirrus using a total-water probe. *J. Atmos. Oceanic Technol.*, **12**, 410–414.

Bruggeman, D. A. G., 1935: Berechnung verschiedener physikalischer konstanten von heterogenen substanzen. *Ann. Phys.*, **24**, 636679.

Chen, M., R. E. Dickinson, X. Zeng, and A. N. Hahmann, 1996: Comparison of precipitation observed over the continental united states to that simulated by a climate model. *Climate Dynamics*, **9**, 2223–2249.

Dai, A., 2001: Global precipitation and thunderstorm drequencies. part i: seasonal and interannual variations. *Climate Dynamics*, **14**, 1593–1616.

Dai, A., F. Giorgi, and K. E. Trenberth, 1999: Observed and model simulated precipitation diurnal cycles over the contiguous united states. *J. Geophys. Res.*, **104**, 6377–6402.

Eyre, J. R., G. A. Kelly, A. P. McNally, E. Andersson, and A. Persson, 1993: Assimilation of tovs radiances information through one-dimensional variational analysis. *Quart. J. Roy. Meteorol. Soc.*, **119**, 1427–1463.

Fabry, F. and I. Zawadzki, 1995: Long-term radar observations of the melting layer of precipitation and their interpretation. *J. Atmos. Sci*, **52**, 838–851.

Freilich, M. H. and B. A. Vanhoff, 2003: The relationship between winds, surface roughness, and radar backscatter at low incidence angles from trmm precipitation radar measurements. *J. Atmos. Oceanic Technol.*, **20**, 549–562.

Fu, Y. and G. Liu, 2001: The variability of tropical precipitation profiles and its impact on microwave brightness temperatures as inferred from trmm data. *J. Appl. Meteor.*, **40**, 2130–2143.

Gill, A. E., 1980: Some simple solutions for heat induced tropical circulations. *Quart. J. Roy. Meteorol. Soc.*, **106**, 447–462.

Halton, J. H. and G. B. Smith, 1964: Algorithm 247: radical-inverse quasi-random point sequence. *Commun. ACM*, **7**, 701–702.

Hardaker, P. ., A. R. Holt, and C. G. Collier, 1995: A melting-layer model and its use in correcting for the bright-band in single-polarization radar echoes. *Quart. J. Roy. Meteorol. Soc.*, **121**, 495–525.

Haynes, J. M., T. S. L'Ecuyer, G. L. Stephens, S. D. Miller, C. M. Mitrescu, N. B. Wood, and S. Tanelli, 2008: Rainfall retrieval over the ocean using spaceborn w-band radar. *Submitted to J. Geophys. Res.*

Haynes, J. M., R. T. Marchand, Z. Luo, A. Bodas-Salcedo, and G. L. Stephens, 2007: A multi-purpose radar simulation package: Quickbeam. *Bull. Amer. Meteor. Soc.*, **88**, 1723–1727.

Haynes, J. M. and G. L. Stephens, 2007: Tropical oceanic cloudiness and the incidence of precipitation: Early results from cloudsat. *Geophys. Res. Letters*, **34**, L09811, doi:10.1029/2007GL029335.

Heymsfield, A. J. and L. M. Miloshevich, 2003: Parameterizations for the cross-sectional area and extinction of cirrus and stratiform ice particles. *J. Atmos. Sci*, **60**, 936–956.

Heysmfield, A. J., C. G. Schmitt, A. Bansemer, D. B. amd E. M. Weinstock, J. T. Smith, and D. Sayres, 2004: Effective ice particle densities for cold anvil cirrus. *Geophys. Res. Letters*, **31**, L02101, doi:10.1029/2003GL018311.

Hitschfeld, W. and J. Bordan, 1954: Errors inherent in the radar measurement of rainfall at attenuating wavelengths. *J. Meteor.*, **11**, 58–67.

Iguchi, R. and R. Meneghini, 1994: Intercomparison of single-frequency methods for retrieving a vertain rain profile from airborne or spaceborne radar data. *J. Atmos. Oceanic Technol.*, **11**, 1507–1516.

Iguchi, T., T. Kozu, R. Meneghini, J. Awaka, and K. Okamoto, 2000: Rain-profiling algorithm for the trmm precipitation radar. *J. Appl. Meteor.*, **39**, 2053–2070.

Im, E., S. L. Durden, and C. Wu, 2005: Cloud profiling radar for the cloudsat mission. *IEEE Aerosp. Electron. Syst. Mag.*, **20**, 15–18.

Jensen, E. J., O. B. Toon, L. Pfister, and H. Selkirk, 1996: Dehydration of the upper troposphere by subvisual cirrus near the tropical tropopause. *Geophys. Res. Letters*, **23**, 825–828.

Johnson, B. and G. W. Petty, 2008: Methods and uncertainties in nodeling of microwave scattering and extinction properties of frozen and mixed phase precipitation: 1. theory. *to be submitted.*

Johnson, R. H., 1986: Implications of lower-tropospheric warming and drying in tropical mesoscale convective systems for the problem of cumulus parameterization. *J. Meteor. Soc. Japan*, **64**, 721–726.

Johnson, R. H., T. M. Rickenbach, S. A. Rutledge, P. E. Ciesielski, and W. H. Schubert, 1999: Trimodal characteristics of tropical convection. *J. Climate*, **12**, 2397–2418.

Johnson, R. H. and G. S. Young, 1983: Heat and moisture budgets of tropical mesoscale anvil clouds. *J. Atmos. Sci*, **40**, 2138–2147.

Joyce, R. and P. A. Arkin, 1997: Improved esimates of tropical and subtropical precipitation using the goes precipitation index. *J. Atmos. Oceanic Technol.*, **14**, 997–1011.

Khairoutdinov, M., D. A. Randall, and C. DeMott, 2005: Simulations of the atmospheric general circulation using a cloud-resolving model as a superparameterization of physical processes. *J. Atmos. Sci*, **62**, 2136–2154.

Kiehl, J. T. and K. E. Trenberth, 1997: Earth's annual global mean energy budget. *Bull. Amer. Meteor. Soc.*, **78**, 197–208.

Klassen, W., 1988: Radar observations and similation of the melting layer of precipitation. *J. Atmos. Sci*, **45**, 3741–3753.

Klein, S. A. and C. Jakob, 1999: Validation and sensitivities of frontal clouds simulated by the ecmwf model. *Monthly Weather Review*, **127**, 2514–2531.

Kozu, T., T. Kawanishi, H. Kuroiwa, M. Kojima, K. Oikawa, H. Kumagai, K. Okamoto, M. Okumura, H. Nakatsuka, and K. Nishikawa, 2001: Development of precipitation radar onboard the tropical rainfall measuring mission (trmm) satellite. *IEEE Trans. Geosci. Remote Sens.*, **39**, 102–116.

Kummerow, C., W. Barnes, T. Kozu, J. Shiue, and J. Simpson, 1998: The tropical rainfall measurement mission (trmm) sensor package. *J. Atmos. Oceanic Technol.*, **15**, 809–817.

Kummerow, C., Y. Hong, W. S. Olson, S. Yang, R. F. Adler, J. McCollum, R. Ferraro, G. Petty, D. B. Shin, and T. T. Wilheit, 2001: The evolution of the goddard profiling algorithm (gprof) for rainfall estimation from passive microwave sensors. *J. Appl. Meteor.*, **40**, 1801–1820.

Kummerow, C., W. S. Olson, and L. Giglio, 1996: A simplified scheme for obtaining precipitation and vertical hydrometeor profiles from passive microwave sensors. *IEEE Trans. Geosci. Remote Sens.*, **34**, 1213–1232.

Lau, K. M. and L. Peng, 1987: Origin of low frequency (intraseasonal) oscillations in the tropical atmosphere. part i basic theory. *J. Atmos. Sci*, **44**, 950–972.

L'Ecuyer, T. S. and G. L. Stephens, 2002: An estimation-based precipitation retieval algorithm for attenuating radars. *J. Appl. Meteor.*, **41**, 272–285.

Legates, D. R., 1995: Global and terrestrial precipitation: A comparative assessment of existing climatologies. *Int. J. Climatol.*, **10**, 111–127.

Li, L., G. M. Heymsfield, L. Tian, and P. E. Racette, 2005: Measurements of ocean surface backscattering using an airborne 94-ghz cloud radar-implication for calibration of airborne and spaceborne w-band radars. *J. Atmos. Oceanic Technol.*, **22**, 1033–1045.

Liebe, H. J., 1985: An updated model for millimeter wave propagation in moist air. *Radio Science*, **20**, 1069.

Lin, X. and R. H. Johnson, 1996: Kimematic and thermodynamic characteristics of the flow over the western pacific warm pool during toga coare. *J. Atmos. Sci*, **53**, 695–715.

Lindzen, R., 2001: Does the earth have an adaptive iris? *Bull. Amer. Meteor. Soc.*, **82**, 417–432.

Liu, G., 2004: Approximation of single scattering properties of ice and snow particles for high microwave frequencies. *J. Atmos. Sci*, **61**, 2441–2456.

— 2007: A database of microwave scattering properties for non-spherical ice particles. *http://cirrus.met.fsu.edu/research/scatdb.html*.

Locatelli, J. D. and P. V. Hobbs, 1974: Fallspeeds and masses of solid precipitation particles. *J. Geophys. Res.*, **79**, 2185–2197.

Lui, C., E. J. Zipser, and S. W. Nesbitt, 2007: Global distrbition of tropical deep convection: different prospectives from trmm infrared and radar data. *Climate Dynamics*, **20**, 489–503.

Mace, G. G., R. Marchand, Q. Zhang, and G. Stephens, 2007: Global hydrometeor occurrence as observed by cloudsat: Initial observations from summer 2006. *Geophys. Res. Letters*, **34**, L09808, doi:10.1029/2006GL029017.

Marchand, R. ., J. M. Haynes, G. Mace, T. Ackerman, and G. L. Stephens, 2008: A comparison of cloudsat cloud radar observations with simulated cloud radar output from the multiscale modeling framework global climate model. *In prep.*

Marshall, J. S. and W. M. Palmer, 1948: The distribution of raindrops with size. *J. Meteor.*, **5**, 165–166.

Marzoug, M. and P. Amayenc, 1994: A class of single-frequency and dual-frequency algorithms for rain-rate profiling from a spaceborne radar. part i: Principle and tests from numerical simulations. *J. Atmos. Oceanic Technol.*, **11**, 1480–1506.

Matrosov, S. Y., 2007: Potential for attenuation-based estimations of rainfall rate from cloudsat. *Geophys. Res. Letters*, **34**, L05817, doi:10.1029/2006GL029161.

Meneghini, R. and L. Liao, 2000: Effective dielectric constants of mixed-phase hydrometeors. *J. Atmos. Oceanic Technol.*, **17**, 628–640.

Menzel, W. P., D. P. Wylie, and K. I. Strabala, 1992: Seasonal and diurnal changes in cirrus clouds as seen in four years of observations with the VAS. *J. Geophys. Res.*, **31**, 370–385.

O'Brien, D. M., 1992: Accelerated quasi monte carlo integration of the radiative transfer equation. *J. Quant. Spectrosc. Radiat. Transfer*, **48**, 41–59.

— 1998: Monte carlo integration of the radiative transfer equation in a scattering medium with stochastic reflecting boundary. *J. Quant. Spectrosc. Radiat. Transfer*, **60**, 573–583.

Oguchi, T., 1983: Electromagnetic wave propagation and scattering in rain and other hydrometeors. *Proc. IEEE*, **71**, 1029–1078.

Ohmura, A. and H. Gilgen, 1993: Re-evaluation of the global energy balance. *Interactions between the global climate subsystems: The legacy of Hann, Geophys. Monogr., No. 75 Int Union Geodesy and Geophys.*, 93–110.

Ohtake, T., 1969: Observations of the size distribution of hydromeors through the melting layer. *J. Atmos. Sci*, **26**, 545–557.

Petty, G. W., 1995: Frequencies and characteristics of global oceanic precipitation from shipboard present-weather reports. *Bull. Amer. Meteor. Soc.*, **76**, 1593–1616.

— 1997: An intercomparison of oceanic precipitation frequencies from 10 special sensor microwave/imager rain rate algorithms and shipboard present weather reports. *J. Geophys. Res.*, **102**, 1757–1777.

— 2004: *A first course in atmospheric radiation*. Sundog Publishing, Madison, WI.

Ramanathan, V. and W. D. Collins, 1991: Thermodynamic regulation of the ocean warming by cirrus clouds deduced from observations of the 1987 el nino. *Nature*, **351**, 27–32.

Randall, D., M. Khairoutdinov, A. Arakawa, and W. Grabowski, 2003: Breaking the cloud parameterizations deadlock. *Bull. Amer. Meteor. Soc.*, **84**, 1547–1564.

Ray, P. S., 1972: Broadband complex refractive indices of ice and water. *Applied Optics*, **11**, 1836–1844.

Rosengrant, M. W. and S. A. Cline, 2003: Global food security: challenges and policies. *Science*, **302**, 1917–1919.

Rossow, W. B. and Y. C. Zhang, 1995: Calculation of surface and top of atmosphere radiative fluxes from physical quantities based on isccp data sets 2. validation and first results. *J. Geophys. Res.*, **100**, 1167–1197.

Ryan, B. F., 2000: A bulk parameterization of the ice particle size distribution and the optical properties of ice clouds. *J. Atmos. Sci*, **57**, 1436–1451.

Sassen, K. and V. I. Khvorostyanov, 2007: Microphysical and radiative properties of mixed phase altocumulus: A model evaluation of glaciation effects. *Atm. Res.*, **84**, 390–398.

Sassen, K., S. Matrosov, and J. Campbell, 2007: Cloudsat spaceborne 94 ghz radar bright bands in the melting layer: An attenuation-driven upside-down lidar analog. *Geophys. Res. Letters*, **34**, L16818, doi:10.1029/2007GL030291.

Shneider, T. L. and G. L. Stephens, 1995: Theoretical aspects of modeling backscattering by cirrus ice particles at millimeter wavelength. *J. Atmos. Sci*, **52**, 4367–4385.

Smith, E. A., J. E. Lamm, R. Adler, J. Alishouse, K. Aonashi, E. Barrett, P. Bauer, W. Berg, A. Chang, R. Ferraro, J. Ferriday, S. Goodman, N. Grody, C. Kidd, D. Kniveton, C. Kummerow, G. Liu, F. Marzano, A. Mugnai, W. Olson, G. Petty, A. Shibata, R. Spencer, F. Wentz, T. Wilheit, and E. Zipser, 1998: Results of the wetnet pip-2 project. *J. Atmos. Sci*, **55**, 1483–1536.

Staudenmaier, M., 1997: The navy operational global atmospheric prediction system (nogaps), western region technical attachment no. 97-09.

Stephens, G. L., 2005: Cloud feedback in the climate system: A critical review. *J. Climate*, **18**, 237–273.

Stephens, G. L. and C. D. Kummerow, 2007: The remote sensing of clouds and precipitation from space: a review. *J. Atmos. Sci*, **64**, 3742–3765.

Stephens, G. L., D. G. Vane, R. J. Boain, G. C. Mace, K. Sassen, Z. E. Wang, A. J. Illingworth, E. J. O'Connor, W. B. Rossow, S. L. Durden, S. D. Miller, R. T. Austin, A. Benedetti, and C. Mitrescu, 2002: The cloudsat mission and the a-train - a new dimension of space-based observations of clouds and precipitation. *Bull. Amer. Meteor. Soc.*, **83**, 1771–1790.

Stephens, G. L., D. G. Vane, S. Tanelli, E. Im, S. Durden, M. Rokey, D. Reinke, P. Partain, G. G. Mace, R. Austin, T. LEcuyer, J. M. Haynes, M. Lebsock, K. Suzuki, D. Waliser, D. Wu, J. Kay, A. Gettleman, and Z. Wang, 2008: The cloudsat mission: performance and early science after the first year of operation. *Submitted to J. Geophys. Res.*.

Stephens, G. L. and N. Wood, 2007: Properties of tropical convection observed by millimeter-radar systems. *Monthly Weather Review*, **135**, 821–842.

Sun, Y., S. Soloman, A. Dai, and R. W. Portmann, 2006: How often does it rain? *Climate Dynamics*, **19**, 916–934.

Szyrmer, W. and I. Zawadzki, 1999: Modeling of the meling later. part i: Dynamics and microphysics. *J. Atmos. Sci*, **56**, 3573–3592.

Tanelli, S., S. L. Durden, E. Im, K. Pak, D. Reinke, P. Partain, J. M. Haynes, and R. Marchand, 2008: Cloudsats cloud profiling radar after 1 year in orbit: performance, calibration, and processing. *Submitted to IEEE TGRS*.

Toit, P. S. D., 1967: Doppler radar observations of drop size in continuous rain. *J. Appl. Meteor.*, **6**, 1082–1087.

Warren, S. G., 1984: Optical constants of ice from the ultraviolet to the microwave. *Applied Optics*, **23**, 1206–1225.

Webb, M., C. Senior, S. Bony, and J. J. Marcrette, 2001: Combining erbe and isccp data to assess clouds in the hadley centre, ecmwf and lmd atmospheric climate models. *Climate Dynamics*, **17**, 905–922.

Wentz, F. J. and T. Meissner, 2007: Amsr-e ocean algorithms supplement 1. *Algorithm Theoretical Basis Document: AMSR-E Ocean Algorithms Supplement 1*.

Winker, D. M., W. H. Hunt, and C. Hostetler, 2004: Status and performance of the caliop lidar. *Laser Radar Techniques for Atmospheric Sensing. Edited by Singh, Upendra N. Proceedings of the SPIE*, **5575**, 8–15.

Winker, D. M., W. H. Hunt, and M. J. McGill, 2007: Initial performance assessment of caliop. *Geophys. Res. Letters*, **34**, L19803, doi:10.1029/2007GL030135.

Woodruff, S. D., R. J. Slutz, R. L. Jenne, and P. M. Steuer, 1987: A comprehensive ocean-atmosphere data set. *Bull. Amer. Meteor. Soc.*, **68**, 1239–1250.

Worley, S. J., S. D. Woodruff, R. W. Reynolds, S. J. Lubker, and N. Lott, 2005: Icoads release 2.1 data and products. *Int. J. Climatol.*, **25**, 823–842.

Zhang, C., 2005: Madden-julian oscillation. *Rev. Geophys.*, **43**, RG2003.